



**HAL**  
open science

# Assimilation of satellite earth observation-derived flood maps for a better parameterization of large scale hydraulic models.

Vita Ayoub

► **To cite this version:**

Vita Ayoub. Assimilation of satellite earth observation-derived flood maps for a better parameterization of large scale hydraulic models.. Earth Sciences. Université de Montpellier, 2022. English. NNT: 2022UMONG094 . tel-04131237

**HAL Id: tel-04131237**

**<https://theses.hal.science/tel-04131237>**

Submitted on 16 Jun 2023

**HAL** is a multi-disciplinary open access archive for the deposit and dissemination of scientific research documents, whether they are published or not. The documents may come from teaching and research institutions in France or abroad, or from public or private research centers.

L'archive ouverte pluridisciplinaire **HAL**, est destinée au dépôt et à la diffusion de documents scientifiques de niveau recherche, publiés ou non, émanant des établissements d'enseignement et de recherche français ou étrangers, des laboratoires publics ou privés.

# THÈSE POUR OBTENIR LE GRADE DE DOCTEUR DE L'UNIVERSITÉ DE MONTPELLIER

En Sciences de la Terre et de l'Eau

École doctorale GAIA

Unité de recherche HydroSciences Montpellier

## ASSIMILATION OF SATELLITE EARTH OBSERVATION-DERIVED FLOOD MAPS FOR A BETTER PARAMETERIZATION OF LARGE SCALE HYDRAULIC MODELS.

Présentée par Vita AYOUB  
le 02 Décembre 2022

Directrice de thèse: Dr. Carole DELENNE  
Co-encadrant: Dr. Renaud HOSTACHE

Devant le jury composé de

Pr. Robert MOSÉ, Professeur, Univ. de Strasbourg, IUT Robert Schumann  
Pr. Hélène ROUX, Professeure, INPToulouse, IMFT  
Dr. Sylvain BIANCAMARIA, Chargé de Recherche, CNRS, UMR LEGOS  
Dr. Laurent PFISTER, Directeur d'Unité, LIST, ENVISION  
Dr. Gilles BELAUD, Professeur, SupAgro, UMR G-EAU  
Dr. Renaud HOSTACHE, Directeur de Recherche, IRD, UMR Espace-Dev  
Dr. Carole DELENNE, HDR, Maitre de Conférence, Univ. de Montpellier, UMR HydroSciences

Rapporteur  
Rapporteuse  
Examineur  
Examineur  
Examineur  
Co-encadrant  
Directrice de thèse



UNIVERSITÉ  
DE MONTPELLIER



# Contents

<b>Acronyms</b>	<b>iii</b>
<b>List of Figures</b>	<b>v</b>
<b>List of Tables</b>	<b>vi</b>
<b>Acknowledgments</b>	<b>vii</b>
<b>Abstract</b>	<b>viii</b>
<b>Résumé</b>	<b>ix</b>
<b>Résumé français étendu</b>	<b>1</b>
Introduction . . . . .	1
Contexte de la thèse . . . . .	1
Problématique de recherche . . . . .	2
Contributions . . . . .	3
Développement d'une chaîne de modélisation hydrodynamique à large échelle . .	3
Amélioration des algorithmes d'estimation automatique de surfaces inondées et niveaux d'eau à partir de des données satellitaires et topographiques. . .	5
Assimilation de cartes d'inondation satellitaires probabilistes dans un modèle hydraulique à partir d'un filtre à particules à tempéragé . . . . .	8
<b>General introduction</b>	<b>12</b>
<b>1 A porosity-based flood inundation modelling approach for enabling faster large scale simulations</b>	<b>15</b>
1.1. Introduction . . . . .	15
1.2. Methodology and experimental setup . . . . .	18
1.2..1 Modelling framework . . . . .	18
1.2..2 Experimental design . . . . .	21
1.3. Study area, experimental data and model setup . . . . .	23
1.3..1 Model setup . . . . .	25
1.4. Results . . . . .	27
1.4..1 Evaluation of simulated flood extent maps . . . . .	27
1.4..2 Evaluation of simulated water level maps . . . . .	29
1.4..3 Evaluation of simulated water levels time series . . . . .	31
1.5. Discussion . . . . .	32
1.6. Conclusion . . . . .	35

<b>2</b>	<b>Estimating flood depth from space: an automatic method based on satellite imagery and topography data</b>	<b>37</b>
2.1.	Introduction . . . . .	37
2.2.	Materials and methods . . . . .	40
2.2.1	Flood extent mapping from SAR imagery . . . . .	40
2.2.2	Pre-processing of topographic data . . . . .	41
2.2.3	WaSER: Water Surface Elevation Retrieval algorithm . . . . .	42
2.2.4	Post-processing . . . . .	44
2.2.5	Evaluation approach . . . . .	45
2.3.	Study site and available data . . . . .	46
2.4.	Results and discussions . . . . .	47
2.4.1	Evaluation of SAR-derived flood extent maps . . . . .	47
2.4.2	Evaluation of the WaSER flood extent maps . . . . .	49
2.4.3	Evaluation of the WaSER water surface elevation maps . . . . .	53
2.4.4	Window size sensitivity analysis . . . . .	56
2.5.	Conclusion . . . . .	57
<b>3</b>	<b>Assimilation of probabilistic flood maps into large scale hydraulic models using a tempered particle filter</b>	<b>60</b>
3.1.	Introduction . . . . .	60
3.2.	Method . . . . .	62
3.2.1	Probabilistic flood mapping . . . . .	62
3.2.2	The shallow water modelling framework . . . . .	63
3.2.3	The data assimilation framework . . . . .	64
3.3.	Study site, available data and experimental design . . . . .	66
3.3.1	Study site and available data . . . . .	66
3.3.2	Experimental design . . . . .	67
3.4.	Results . . . . .	70
3.5.	Discussion and conclusion . . . . .	74
	<b>General Conclusions and Perspectives</b>	<b>80</b>
	<b>Author Publications</b>	<b>83</b>
	<b>Bibliography</b>	<b>97</b>

# Acronyms

CPU	process time
CSI	critical success index
DA	data assimilation
DEM	digital elevation model
DIP	dual integral porosity
EO	earth observation
FE	flood extent
FN	false negatives
FP	false positives
IP	integral porosity
IQR	interquartile range
LiDAR	light detection and ranging
OA	overall accuracy
PF	particle filter
PFM	probabilistic flood maps
RMSD	root square mean error
SAR	synthetic aperture radar
SW2D	shallow water two-dimensionnal
SW2D-DDP	shallow water 2-dimensionnal depth-dependant porosity
SWE	shallow water equations
TN	true negatives
TP	true positives
TPF	tempered particle filter
WaSER	water surface elevation retrieval
WSE	water surface elevation

# List of Figures

1	Zone d'étude . . . . .	4
1.1	Porosity laws: a) law type 0; b) law type 3; c) bathymetry representation using law type 3. $z$ : elevation, $\phi$ : porosity, $s$ : abscissa along the river cross-section. . .	20
1.2	0.25 km <sup>2</sup> subset of: a) the standard model mesh, b) the porosity model mesh. .	20
1.3	Study site: model boundaries and location of the gauging stations and the river camera. The background colours illustrate the classification of ground elevation.	24
1.4	Model boundary conditions for the 2007 (a) and the 2012 (b) flood events: Upstream streamflow (Saxons Lode and Bredon) and downstream water level (Deerhurst) time series. . . . .	26
1.5	CSI and OA scores time series showing agreement between simulated (porosity) and "reference" (standard) flood extent maps, CSI: Critical Success Index & OA: Overall Accuracy. . . . .	27
1.6	Contingency maps between porosity and fine models for simulation days 3, 7 and 16 of the 2007 flood event . . . . .	28
1.7	Contingency maps between porosity and fine models for simulation days 1, 7 and 15 of the 2012 flood event . . . . .	28
1.8	Contingency maps computed from the satellite and each of the standard (a) and porosity (b) model flood maps, on December 04, 2012. . . . .	30
1.9	Root mean square deviations (RMSD) in meters, between SW2D-DDP and SW2D simulated water level maps (resampled at DTM resolution): a) 2007 and b) 2012 flood events. . . . .	30
1.10	Boxplots drawn from the simulated water level deviations using as a reference the standard model - orange line: median; triangle: mean; box: interquartile range; whisker ends: the lower and upper bounds: (a) 2007 and (b) 2012 flood events. . . . .	31
1.11	Water level time series evaluation using data at Mythe Bridge for the 2007 event (a), 2012 event (b) and at Tewkesbury for the 2012 event (c). . . . .	33
1.12	Drains representation by computational cells in the SW2D (orange) and SW2D-DDP (blue) models. . . . .	35
2.1	Computing HAND values using a DEM . . . . .	41
2.2	WaSER HAND G. and HAND L. (a), DEM L. (b) algorithm variant flowcharts.	42
2.3	Study area showing the area of interest (AOI), Rivers Severn and Avon, and the urban area of Tewkesbury. 1) CopDEM topographic data (DEM), 2) HAND map derived from CopDEM, 3) Extent indicator. . . . .	47
2.4	Contingency maps between the SAR and the aerial photography-derived flood maps: left: TerraSAR-X; right: Envisat. . . . .	48
2.5	Contingency maps between the WaSER and the aerial photography-derived flood maps: (a,d) HAND G., (b,e) HAND L. and (c,f) DEM L. variants, 1st row: SRTM/Envisat; 2nd row: SRTM/TerraSAR-X. . . . .	50

2.6	Contingency maps between the WaSER and the aerial photography-derived flood maps: (a,d) HAND G., (b,e) HAND L. and (c,f) DEM L. variants, 1st row: CopDEM/Envisat; 2nd row: CopDEM/TerraSAR-X. . . . .	51
2.7	Contingency maps between the WaSER and the aerial photography-derived flood maps: (a) HAND G., (b) HAND L. and (c) DEM L. variants, 1st row: LiDAR/Envisat; 2nd row: LiDAR/TerraSAR-X. . . . .	52
2.8	Boxplots of WSE deviations of the WaSER with respect to the hydraulic model outputs (a-f). White horizontal segments and red diamonds represent the median and mean, respectively. . . . .	55
2.9	boxplot of the SRTM/CopDEM deviations with respect to the LiDAR (g). White horizontal segments and red diamonds represent the median and mean, respectively.	56
2.10	WSE deviation maps between the WaSER (after post-processing) and the hydraulic model WSE maps. From left to right, 1st row: Srtm/Envisat HAND G., HAND L., DEM L., 2nd row: LiDAR/TerraSAR-X HAND G., HAND L., DEM L.	57
2.11	CSI, OA and RMSD scores using the DEM L. variant with LiDAR/TSX. . . . .	58
3.1	Riverbed porosity law: Left: Law type 3 attributed to riverbed cells in the mesh; Right: bathymetry representation; $z$ : elevation, $\phi$ : porosity, $d$ : river depth, $s$ : abscissa along the river cross-section. $L1$ : Bottom width; $L2$ : River width, $L3$ : Riverbed cell width. . . . .	64
3.2	Study site showing the three river reaches and the available gauging stations and river camera. . . . .	67
3.3	CosmoSky-Med probabilistic flood maps for the 2012 event. . . . .	68
3.4	Cross sections at Saxons Lode, Bredon and Deerhurst. . . . .	69
3.5	Test 1param daily time series of the water surface elevations, for a) the OL and b) the last iteration. Black lines correspond to the particle ensemble and the red line to the observation, at Mythe Bridge. . . . .	71
3.6	Test 1param + ExLay daily time series of the water surface elevations, for a) the OL and b) the last iteration. Black lines correspond to the particle ensemble and the red line to the observation, at Mythe Bridge and Tewkesbury. . . . .	73
3.7	Test 2param daily time series of the water surface elevations, for a) the OL and b) the last iteration. Black lines correspond to the particle ensemble and the red line to the observation, at Mythe Bridge and Tewkesbury. . . . .	74
3.8	Test 2param + ExLay daily time series of the water surface elevations, for a) the OL and b) the last iteration. Black lines correspond to the particle ensemble and the red line to the observation, at Mythe Bridge and Tewkesbury. . . . .	75
3.9	Test 3param daily time series of the water surface elevations, for a) the OL and b) the last iteration. Black lines correspond to the particle ensemble and the red line to the observation, at Mythe Bridge and Tewkesbury. . . . .	76
3.10	Test 3param + ExLay daily time series of the water surface elevations, for a) the OL and b) the last iteration. Black lines correspond to the particle ensemble and the red line to the observation, at Mythe Bridge and Tewkesbury. . . . .	77
3.11	Test 4param daily time series of the water surface elevations, for a) the OL and b) the last iteration. Black lines correspond to the particle ensemble and the red line to the observation, at Mythe Bridge and Tewkesbury. . . . .	78
3.12	Test 4param + ExLay daily time series of the water surface elevations, for a) the OL and b) the last iteration. Black lines correspond to the particle ensemble and the red line to the observation, at Mythe Bridge and Tewkesbury. . . . .	79

# List of Tables

1.1	Performance of the flood inundation extents simulated by the porosity (SW2D-DDP) and standard (SW2D) models computed using as a reference the satellite flood extent maps available for the 2007 and 2012 events. CSI: Critical Success Index; OA: Overall Accuracy. . . . .	29
1.2	RMSDs computed between the water level time series simulated by the porosity (SW2D-DDP) and standard (SW2D) models and Mythe Bridge gauge data for both flood events and Tewkesbury camera data of the 2012 flood event; RMSD: root mean square deviation. . . . .	32
1.3	Simulation run time for the porosity (SW2D-DDP) and standard (SW2D) models, with the run time reduction factor . . . . .	35
2.1	Goodness of fit metrics between the $FE_{SAR}$ map (TerraSAR-X (TSX.) and Envisat (Env.)) and i) the aerial photograph (P.), ii) the model simulations (M.)-derived flood maps. OA: Overall Accuracy, CSI: Critical Success Index. . . . .	48
2.2	Performance metrics evaluating the $FE_{WaSER}$ and $WSE_{WaSER}$ maps using as a reference: i) the aerial photograph (P.), ii) the model results (M.). OA: Overall Accuracy, CSI: Critical Success Index, RMSD: Root Mean Square Deviations, Sm.: Smoothing, No sm.: No smoothing, TSX: TerraSAR-X, Env.: Envisat. Values in pink and orange correspond to the best results in terms of OA(P.) and RMSD, respectively. . . . .	49
3.1	RMSE performances ( $\pm$ standard deviation) for the OL and the posterior derived WSEs, for the different scenario tests. Performances obtained with the ADWR control simulation: $RMSE(Mythe\ Bridge)=0.24$ ; $RMSE(Tewkesbury)=0.43$ . . . .	72
3.2	$z_1$ Parameter means and standard deviations obtained for the OL and the posterior, for the different scenarios. Observed river bottom values on observed cross sections: Saxons Lode: $z_1=4.39\pm 0.9$ ; Bredon: $z_1=6.43\pm 0.44$ ; Deerhurst: $z_1=3.8\pm 0.17$ . . . . .	72

# Acknowledgements

This PhD thesis would not have been successful without the support of people who helped me reach this point.

First of all, I would like to thank all members of the jury for accepting to review and discuss this work. I would also like to thank all members that participated in my annual steering committees; our exchanges have been a great opportunity to criticise and broaden thoughts on my thesis.

I would like to express my immense gratitude to my supervisors Carole and Renaud, who hosted me and offered me this opportunity. I would like to thank them for their patience, guidance and continuous support that were decisive in the accomplishment of this work. Beyond the professional experience, your mentoring allowed me to challenge and improve myself.

My sincere gratitude to the people I have worked with in LIST, HydroSciences and Lemon teams, for the warm working environment and the insightful scientific discussions. A special thank you for my colleagues with whom I shared offices (yes in those four years, I have had a few!), and those in the CAT group for the good times we shared!

My words will not be strong enough to express how grateful for my friends and those who are dear to my heart. Thank you for the good times and also for always showing up and listening when I need it the most.

I would like to thank my parents and my sisters, for their unconditional love and encouragement.

For my biggest support system and cheerleader, a big thank you for believing I can achieve anything I put my mind into!

# Abstract

With the objective of assessing flood hazard at a large scale, there is currently a growing interest for regional to global scale flood models. However, predicting flood hazard at high resolution and over large areas remains challenging due to (i) the recurrent lack of in situ hydrological data, (ii) the high computing demand of accurate hydrodynamic models when applied over large areas and (iii) the rather large model uncertainty due to physical simplifications, numerical approximations and uncertainty in input and geometrical data. In this context, the PhD focuses on one main research question: *How to optimally integrate large collections of satellite derived flood information for parameterizing and controlling large scale hydraulic models over data scarce areas?* The PhD leverages recent developments in hydrodynamic modelling and proposes an innovative hydraulic modelling framework based on the two-dimensional shallow water model with depth dependant porosity (SW2D-DDP). This model uses an unstructured mesh and incorporates porosity concepts in combination with the traditional 2D shallow water equations. In this model, the definition of porosity as a function of water depth allows for a more detailed representation of the floodplain and riverbed geometry, even when adopting comparatively large cell sizes. Thus, one of the main objectives of the thesis is the evaluation of the developed modelling approach for large-scale applications. Moreover, the lack of input data often required for hydraulic models, motivates the exploitation of satellite and topographic data, which are becoming increasingly globally available. Recent studies have enabled the automatic extraction of flooded areas via robust and effective algorithms. Nevertheless, automatic and efficient algorithms for estimating spatially distributed water levels are still lacking. Thus, a second objective is to develop an automatic water level estimation algorithm using satellite and topographic data only. In addition, the efficient integration of this remote sensing flood information into hydraulic models remains a crucial problem. As a matter of fact, a data assimilation algorithm (of inundation extent maps) based on a tempered particle filter is exploited to optimally combine observation and model data in order to: i) reduce the uncertainties related to these two sources of information and ii) optimally represent the bathymetry in this hydraulic model.

**Keywords:** Flood inundation, hydraulic modelling, satellite imagery, data assimilation, water levels, topography, bathymetry, fast simulation, large scale.

# Résumé

Dans le but d'évaluer les risques d'inondation à grande échelle, il existe actuellement un intérêt croissant pour les modèles d'inondation à l'échelle régionale et mondiale. Cependant, la cartographie des risques d'inondation à haute résolution et sur de grandes zones reste un défi en raison : i) du manque récurrent de données hydrologiques in situ ; ii) des temps calcul souvent élevés des modèles hydrodynamiques précis lorsqu'ils sont appliqués sur de grandes zones ; et iii) de l'incertitude souvent importante des modèles en raison des simplifications physiques, des approximations numériques et de l'incertitude des données d'entrée et géométriques. Dans ce contexte, la thèse se concentre sur une question de recherche principale : Comment intégrer de manière optimale de grandes collections d'informations satellitaires sur les inondations pour paramétrer et contrôler des modèles hydrauliques à grande échelle dans des zones peu instrumentées ? Les travaux de thèse s'appuient d'une part, sur un cadre de modélisation hydraulique innovant qui utilise une version de SW2D basée sur une porosité variable en fonction de la profondeur, appelée SW2D-DDP (Shallow Water with Depth-Dependant Porosity). Ce modèle utilise un maillage non structuré et intègre les concepts de porosité en combinaison avec les équations traditionnelles de Barré de Saint-Venant 2D. Dans ce modèle, la définition de la porosité variable en fonction de la profondeur de l'eau permet de représenter une géométrie plus détaillée de la plaine d'inondation et du lit de la rivière, même en adoptant des tailles de cellules comparativement grandes. Ainsi, l'un des objectifs principaux de la thèse est l'évaluation de l'approche de modélisation développée pour une application à large échelle. D'autre part, le manque de méthodes efficaces en temps de calcul pour l'estimation des niveaux d'eau dans des zones inondées, motive l'exploitation de données satellitaires et topographiques, de plus en plus disponibles globalement. Les études récentes ont permis l'automatisation d'algorithmes robustes d'extraction d'étendues inondées. Néanmoins, les algorithmes d'estimation de niveaux d'eau spatialement distribués, restent limités. Ainsi, un deuxième objectif est de développer un algorithme automatique d'estimation de niveaux d'eau à partir de données satellitaires et topographiques uniquement. En outre, l'intégration efficace de ces informations de télédétection sur les inondations dans les modèles hydrauliques reste un problème crucial. Ainsi, un algorithme d'assimilation de données (de cartes d'étendues inondées) basée sur un filtre à particules à tempéragé est exploité pour combiner de manière optimale les données observées et simulées par le modèle dans le but : i) de réduire les incertitudes liées à ces deux sources d'information et ii) de réestimer la bathymétrie dans ce modèle hydraulique lorsque cette donnée n'est pas disponible.

**Mots clés :** Inondations, modélisation hydraulique, imagerie satellitaire, assimilation de données, niveaux d'eau, topographie, bathymétrie, simulation rapide, large échelle.

# Résumé français étendu

*Conformément au Code de l'Éducation (Article L121-3), nous proposons un résumé étendu en français.*

---

Introduction . . . . .	1
Contexte de la thèse . . . . .	1
Problématique de recherche . . . . .	2
Contributions . . . . .	3
Développement d'une chaîne de modélisation hydrodynamique à large échelle . .	3
Amélioration des algorithmes d'estimation automatique de surfaces inondées et niveaux d'eau à partir de des données satellitaires et topographiques. . .	5
Assimilation de cartes d'inondation satellitaires probabilistes dans un modèle hydraulique à partir d'un filtre à particules à tempéragé . . . . .	8

---

## Introduction

### Contexte de la thèse

Cette thèse s'est déroulée du 15 Novembre 2018 jusqu'au 14 Novembre 2022, au Luxembourg pour deux tiers du temps, et en France pour le reste, dans le cadre du projet CASCADE<sup>1</sup> (Combining earth observation with a large scale model cascade for assessing flood hazard at high spatial resolution), financé par le Fonds National de la Recherche (FNR). La collaboration est menée entre le Luxembourg Institute of Science and Technology (LIST), unité de recherche Environmental Sensing and Modelling, au sein du groupe Remote Sensing and Natural Resources Modelling (REMOTE), et l'Université de Montpellier (UM), unité de recherche HydroSciences (HSM), au sein de l'équipe Hydrologie, Ecohydrologie, Climat (HEC).

---

<sup>1</sup><https://www.list.lu/en/environment/project/cascade/>

Le département Environmental Research and Innovation (ERIN) au LIST compte 200 scientifiques et ingénieurs spécialisés dans les domaines de l'Environnement, les Sciences de la Vie et l'Informatique. Divisé en trois unités de recherche, ses principaux objectifs sont d'offrir des solutions aux défis environnementaux auxquels notre société est confrontée aujourd'hui, notamment l'atténuation du changement climatique, les systèmes énergétiques durables, la sécurité maritime et la gestion efficace des ressources renouvelables. Dans le groupe Remote Sensing and Natural Resources Modelling, plus particulièrement dans la thématique des risques naturels, les projets fournissent une aide à la décision fondée sur des preuves en temps quasi réel, à travers la télédétection et la modélisation hydrologique et hydraulique. De même, l'équipe HEC à HSM s'implique sur des problématiques inhérentes aux grands enjeux environnementaux et sociétaux, dont le changement climatique, l'évolution des ressources hydrologiques et végétales, et l'aménagement du territoire sous pression démographique. Ses principaux objectifs sont de mieux caractériser les interactions entre les processus hydrologiques, écohydrologiques et atmosphériques, et ensuite d'améliorer les modèles de type statistiques, conceptuels et/ou à base physique, à échelles spatiales et temporelles variées.

## Problématique de recherche

Les inondations comptent parmi les risques naturels les plus dévastateurs au monde. Avec le changement climatique et l'urbanisation croissante, les inondations devraient devenir plus fréquentes et plus graves à l'avenir. Afin de lutter contre ce risque, la communauté scientifique s'intéresse de près à la cartographie d'inondation. Les études d'impact des inondations sont très souvent menées dans les études d'aménagement des territoires et la conception d'ouvrages hydrauliques afin de réduire les dégâts potentiels qui y sont associés. Le principal objectif de cette thèse est de développer et d'automatiser des méthodes dans le domaine de la cartographie des risques d'inondation à travers la télédétection et la modélisation hydraulique. Même si la littérature et les applications développées dans ce domaine de recherche sont vastes, les enjeux de modélisation hydraulique à large échelle ainsi que la disponibilité accrue des données satellitaires et topographiques engendrent de nouveaux axes de recherche. Ainsi, cette thèse vise à proposer des solutions aux problématiques suivantes :

- **La modélisation à large échelle et à haute résolution.** La modélisation des inondations à large échelle et à haute résolution est confrontée à plusieurs défis, dont en particulier : i) le temps de calcul qui augmente avec l'augmentation du nombre de mailles discrétisant une surface d'intérêt assez large, et ii) le manque de données nécessaires à la mise en place des modèles hydrauliques (ex : géométrie de la rivière).
- **Le manque de méthodes efficaces et automatiques pour l'estimation des niveaux d'eau dans les zones inondées.** Surfaces inondées et niveaux d'eau sont deux variables particulièrement intéressantes dans la cartographie des risques d'inondation. Alors qu'il existe plusieurs méthodes pour extraire automatiquement les étendues inondées à partir des données satellitaires et données topographiques, il reste peu d'approches

---

qui ont abordé le calcul automatique des niveaux d'eau distribués spatialement pour une zone donnée.

- **Le manque général de données relatives à la bathymétrie, paramètre primordial dans la modélisation hydraulique.** L'information de la topographie en zones émergées est souvent disponible grâce aux modèles numériques de terrain mais la géométrie du fond des rivières (bathymétrie) est une donnée rarement disponible car pour l'instant impossible à collecter à partir d'observations satellitaires, nécessitant ainsi de lourdes campagnes de mesures in situ.

## Contributions

Afin de répondre aux problématiques de recherche mentionnées précédemment, plusieurs méthodologies s'appuyant sur des outils de traitement d'image, de chaînes de modélisation hydrodynamique et d'assimilation de données, sont proposées dans cette thèse. La contribution du travail mené pendant la durée de cette thèse se divise en trois parties principales :

1. Mise en place d'une chaîne de modélisation hydrodynamique à large échelle, permettant de préserver l'information topographique à haute résolution, tout en réduisant le temps de calcul.
2. Amélioration des algorithmes d'extraction automatique de surfaces inondées et niveaux d'eau à partir de la fusion d'images satellitaires et de données topographiques.
3. Assimilation d'images satellitaires dans le modèle hydraulique proposé dans une perspective d'estimation de paramètres inconnus, tels que la bathymétrie.

**Zone d'étude** Le site d'étude situé à la confluence des rivières Severn et Avon autour de la zone urbaine de Tewkesbury, est d'environ 150 km<sup>2</sup> (voir Figure 1). Cette zone d'étude a été choisie pour son historique assez fréquent en termes d'épisodes d'inondation, et parce que l'on possède un ensemble d'informations permettant l'évaluation des méthodes proposées.

## Développement d'une chaîne de modélisation hydrodynamique à large échelle

L'objectif principal de cette partie (présentée au chapitre 1 du document de thèse) est de relever les défis de la modélisation hydrodynamique à grande échelle. L'inconvénient de la discrétisation d'une zone à l'aide d'un maillage fin, outre l'étape de conception du maillage, est le coût de calcul élevé des simulations. Cependant, augmenter la taille des mailles entraîne une baisse de la précision, parce qu'on obtient des résultats moyennés par unité de maille. Au cours des dernières années, le développement de modèles sous-maille a suscité un intérêt croissant car ils permettent des simulations plus rapides en utilisant des cellules plus grossières. Dans ce chapitre, nous proposons et évaluons un cadre de modélisation basé sur un modèle Shallow

Water 2D à porosité [50], qui résout les équations de Saint-Venant sur de grandes mailles, tout en gardant une représentation sous-maille de la topographie de la plaine d'inondation et du lit de la rivière à travers des fonctions de porosité. Lorsque la bathymétrie de la rivière n'est pas disponible, elle peut devenir un paramètre de calage de la loi de porosité.

Afin de permettre une évaluation spatiale du modèle, nous mettons en place un modèle standard 2D à haute résolution et l'utilisons comme référence. Nous exploitons également des données de terrain et des cartes d'inondations dérivées de la télédétection pour évaluer le cadre de modélisation proposé. Nous utilisons comme cas test les inondations de 2007 et 2012 du bassin de la Severn, avec des durées d'évènement de 17 et de 12 jours, respectivement. Les données topographiques sont dérivées d'un MNT LiDAR à 2 m, et les données bathymétriques sont re-construites à partir de trois profils en travers bathymétriques de la rivière, disponibles aux limites amont et aval du modèle. L'hypothèse de forme trapézoïdale simplifiée est choisie pour représenter le lit de la rivière dans les deux modèles. Le MNT est modifié en conséquence pour inclure l'altitude du fond de la rivière. Les lois de porosité sont alors automatiquement déduites à partir des seules informations du tracé de la rivière et du MNT. La construction des maillages formera ainsi : 29,772 mailles pour le modèle standard, et 1,042 mailles pour le modèle à porosité. Le paramétrage est le même pour les deux modèles : i) des débits imposés en amont à Saxons Lode et à Bredon (voir emplacement sur la Figure 1), et des niveaux d'eau en aval à Deerhurst, comme conditions aux limites ; ii) un niveau d'eau uniforme égal à la condition aval à  $t = 0$ , comme condition initiale ; iii) un coefficient Strickler uniforme  $K_s = 50 \text{ m}^{1/3} \text{ s}^{-1}$ .

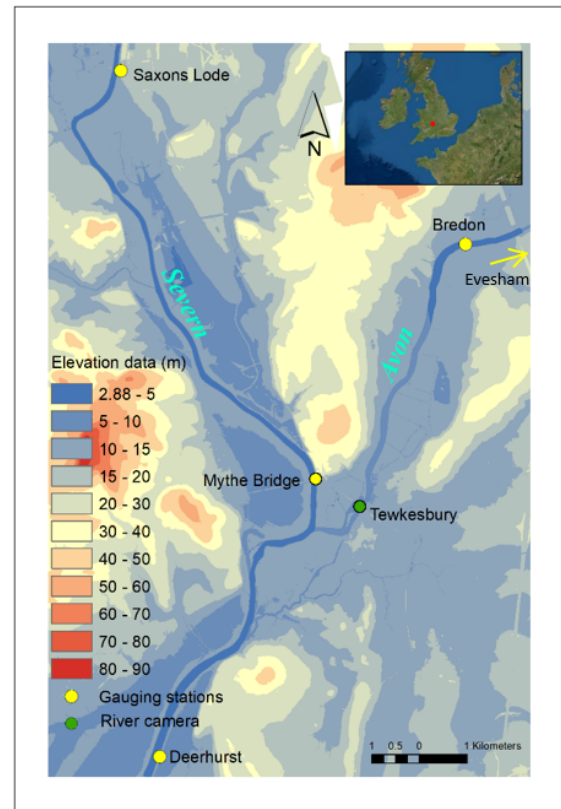


**Figure 1** : Zone d'étude

Les résultats du modèle à porosité et du modèle de référence sont comparés en termes d'étendues inondées et de niveaux d'eau. Pour cela, les résultats obtenus par maille, sont tout d'abord convertis en images. Les indices de performance CSI (Critical Success Index) et OA (Overall Accuracy) – calculés via une comparaison « pixel à pixel » dans les deux images – montrent un très bon accord entre les deux modèles (OA=95%), au pic de crue. En outre, la concordance des modèles s'affaiblit légèrement lors de la montée de la crue, lorsque le modèle à

---

porosité inonde localement des zones plus grandes que le modèle standard, notamment en amont de la rivière et dans la zone urbaine au niveau de la confluence. Cette concordance est plus fortement affaiblie lors de la décrue, lorsque inversement, le modèle standard inonde des zones plus larges, notamment dans la plaine d'inondation Est de la Severn et la zone urbaine. Ceci indique, dans un premier temps, une dynamique de drainage différente pour les deux modèles. La comparaison des niveaux d'eau simulés par les deux modèles est évaluée via des données de station de mesure disponibles à l'intérieur du domaine du modèle, à Mythe Bridge et à Tewkesbury (voir emplacement sur la Figure 1). D'abord, les RMSEs (racine carrée de l'erreur quadratique moyenne) sont calculées au niveau du pixel, entre les niveaux d'eau simulés par les deux modèles. Ces RMSEs, égales à 12.32 cm et 6.3 cm pour les évènements 2007 et 2012, sont acceptables étant donnée la précision verticale (environ 10 à 15 cm) du MNT LiDAR utilisé. Un très bon accord des deux modèles est alors visible lors du pic de crue, alors que les écarts les plus élevés sont observés lors de la montée de crue et de la décrue. Par ailleurs, une sur-estimation des niveaux par le modèle à porosité lors de la montée de crue indique que ce modèle induit un débordement plus rapide que le modèle standard. D'autre part, la sous-estimation des niveaux d'eau calculés par le modèle à porosité lors de la décrue, implique qu'il draine l'eau présente dans le modèle plus rapidement que le modèle standard. Nous avons ensuite utilisé les séries temporelles de mesures *in situ* à Mythe Bridge et Tewkesbury pour évaluer les niveaux d'eau simulés par les deux modèles. L'inter-comparaison des deux modèles montre un très bon accord général. Les plus grands écarts aux mesures sont observés juste avant le pic de crue de 2007, et lors du premier jour de l'évènement de 2012. Par ailleurs, l'évaluation montre des écarts réduits, notamment lors de la décrue de 2012, où le modèle à porosité présente une erreur de moins de 5 cm environ. Ainsi, les écarts importants observés en montée de crue sont probablement liés à la condition initiale fixée comme uniforme et correspondant au niveau aval de Deerhurst. D'autre part, les écarts semblent être un peu diminués pour les résultats du modèle à porosité par rapport aux résultats du modèle standard.

En conclusion, le modèle standard et le modèle à porosité atteignent une précision du même ordre de grandeur, avec un temps de calcul beaucoup plus réduit pour le modèle à porosité, environ 350 fois plus vite que le modèle standard.

## **Amélioration des algorithmes d'estimation automatique de surfaces inondées et niveaux d'eau à partir de données satellitaires et topographiques.**

L'objectif principal de cette partie (présentée au chapitre 2 du document de thèse) est de développer une méthode automatique d'extraction de cartes d'inondation (flood extent : FE) et de niveaux d'eau (Water Surface Elevation : WSE) spatialement distribués, à partir de données satellitaires et topographiques. La majorité des algorithmes d'estimation développés au cours des dernières décennies, sont conçus pour délimiter les étendues inondées sans information sur la profondeur de l'eau. Dans ce contexte, nous présentons une méthode – automatisée et non su-

pervisée d'estimation de la profondeur des eaux de crue, basée sur la fusion de données d'observation satellitaires et topographiques – nommée WaSER (WATER Surface Elevation Retrieval). Dans notre étude, les observations satellitaires sont des images radars à synthèse d'ouverture (SAR en anglais), et la topographie est présentée sous deux formes : i) le modèle numérique de terrain (Digital elevation Model : DEM) et ii) la hauteur au-dessus du point de drainage le plus proche (Height Above Nearest Drainage : HAND), qui en est dérivée. Ainsi, trois variantes de WaSER sont proposées et nommées : HAND global, HAND local et DEM local. Elles reposent toutes sur les étapes génériques suivantes : i) le seuillage de données topographiques (HAND ou DEM) global ou local pour produire des cartes d'inondation synthétiques, ii) l'optimisation du seuil en sélectionnant la carte synthétique qui présente le meilleur accord avec la carte d'inondation satellitaire obtenue par la méthode proposée par [19], et iii) la génération de cartes de hauteur d'eau (Water Depth ou WD) et de niveau d'eau. Ensuite, un lissage spatial au sein d'une fenêtre mobile est effectué sur les cartes de niveaux d'eau, afin de réduire le bruit qui a été produit lors de l'utilisation des variantes locales. Cette étude comporte ainsi une analyse comparative de ces trois variantes afin d'évaluer leurs avantages et leurs limites. Nous utilisons l'inondation de 2007 de la rivière Severn au Royaume-Uni comme cas test car le jeu de données d'évaluation est conséquent. Ainsi, nous évaluons un total de 18 cartes d'inondation, issues de la fusion entre une carte d'inondation satellitaire (Envisat ou Terrasar-X) et des données de topographie (SRTM, CopDEM ou LiDAR), en utilisant chacune des trois variantes WaSER proposées. De plus, nous évaluons l'effet de post-traitement (lissage) des cartes de niveaux d'eau, d'où un total de 36 cartes.

Nous avons évalué la performance de chacune des variantes de WaSER en comparant les cartes obtenues à celle des cartes d'inondation issues des images SAR uniquement. Les résultats ont montré que globalement, les deux cartes d'inondation satellitaire, dérivées de TerraSAR-X et Envisat, présentent un bon accord avec les cartes d'évaluation, malgré quelques sous-détections principalement visibles aux extrémités des zones inondées et dans la partie nord de la zone urbaine de Tewkesbury. L'utilisation de la variante HAND G présente l'avantage de réduire les sous-estimations, en comblant les « trous » produits par la carte d'inondation satellitaire. Ceci est accompagné par un risque de sur-estimation, dans d'autres zones de la carte. Ce mélange de sous-estimation et de sur-estimation est lié à l'utilisation d'un seul seuil sur l'ensemble du domaine, résultant en un meilleur compromis « global ». En effet, l'optimisation d'un seuil HAND unique global sur une image entière, entraîne des sous-estimations locales, lorsque des pixels contigus, inondés dans la carte d'inondation satellitaire, ont des valeurs HAND très différentes. Ceci rend difficile pour WaSER d'optimiser une valeur de seuil unique produisant une carte d'inondation optimisée à 100% similaire à la carte d'étendues satellitaire. Ainsi, nous constatons que dans la majorité des cas la carte d'inondation optimisée est plus performante que la carte d'inondation satellitaire seule, lorsque nous utilisons les variantes locales HAND L. et DEM L. Le seuil calibré est ainsi mieux adapté localement et reflète une meilleure classification de l'eau, conformément à la carte d'inondation satellitaire. La variante DEM L. est la plus performante de toutes les variantes en terme de carte d'inondation, notamment lors de l'utilisation

---

de topographie à plus haute précision (CopDEM et LiDAR). La sous-estimation des étendues inondées constatée dans certaines régions est très probablement due à une sous-détection de l'eau initialement dans la carte d'inondation satellitaire, entraînant ainsi une sous-estimation du seuil optimisé. Dans l'ensemble, l'algorithme WaSER dans ses trois variantes fournit de meilleures détections dans les zones rurales que dans les zones urbaines.

En terme de niveaux d'eau, la variante HAND G. présente les meilleurs résultats des racines carrées de la déviation quadratique moyenne (RMSD) lors de la fusion des données à moyenne résolution : SRTM et Envisat. Ceci est visible dans les cartes de différence entre les niveaux d'eau estimés par WaSER et par le modèle hydraulique, où la distribution générale des déviations est globalement homogène. Ceci est aussi observable dans la distribution des déviations entre estimation et référence qui varie entre -1 et 1 m. Cette distribution devient asymétrique lorsqu'on utilise des approches locales (HAND L. et DEM L.), reflétant ainsi une sur-estimation des niveaux d'eau par rapport aux sorties du modèle. Cependant, les médianes sont principalement situées entre 0 et 1 m, ce qui reflète un bon accord entre les résultats donnés par notre méthode et ceux fournies par le modèle d'évaluation. Nous observons des différences assez importantes surtout au début et à la fin d'évènement de crue (outliers virés pour une meilleure visualisation des valeurs autour de 0). Ceci signifie que cette sur-estimation est due à des niveaux d'eau estimés par WaSER particulièrement élevés localement. Par ailleurs, nous observons un mélange de sous-estimation et de sur-estimation des niveaux d'eau, généré par la variante HAND G. en utilisant les données LiDAR/TerraSAR-X et CopDEM/TerraSAR-X. Ceci est cohérent avec ce qui a été observé pour les cartes d'étendues inondées. Il est cependant important de noter que la sur-estimation reste prépondérante par rapport à la sous-estimation, notamment lors de l'utilisation du HAND L. Cela révèle clairement que l'approche basée sur HAND souffre des discontinuités dues à de fortes variabilités locales des valeurs de HAND, lorsqu'on utilise des données topographiques à haute résolution. La variante DEM L. offre les meilleurs résultats dans l'ensemble, et des écarts plus petits en utilisant l'image à plus haute résolution (TerraSAR-X). En outre, l'analyse de l'effet du post-traitement des WSE a montré également que les déviations minimales et maximales sont réduites après le lissage, en particulier lors de l'utilisation des variantes locales. La taille de la fenêtre déterminée a priori dans cette étude est égale à 2010 mètres, représentant donc 201 pixels avec une taille de pixel de 10 m. Ce choix a été fait en se basant sur la largeur de la plaine inondable de la Severn en aval et a été contraint à respecter deux conditions : i) la taille de la fenêtre doit être suffisamment petite pour garantir l'hypothèse d'un niveau d'eau plutôt constant sur toute la fenêtre, et ii) la taille de la fenêtre doit être suffisamment grande pour inclure les pixels inondés et non inondés. L'analyse de sensibilité menée pour évaluer la précision en termes d'estimation carte de FE et de WSE en utilisant la variante DEM L. montre un optimum de taille de fenêtre à  $locws=250$  pixels. Au fur et à mesure que la taille de la fenêtre augmente, les scores se stabilisent. Nous pensons néanmoins, que des recherches supplémentaires devraient être menées pour mieux investiguer l'effet de la taille de la fenêtre, en effectuant des tests sur différents sites d'études. En conclusion, la méthode d'estimation de niveaux d'eau développée permet de cartographier

des étendues inondées et des niveaux d'eau, en quelques minutes et sans faire de calcul hydraulique, en utilisant des données topographiques et satellitaires. L'influence du paramètre du seuil local dans les variantes locales mérite d'être examiné.

## **Assimilation de cartes d'inondation satellitaires probabilistes dans un modèle hydraulique à partir d'un filtre à particules à tempérag**

L'objectif de cette partie (présentée au chapitre 3 du document de thèse) est d'intégrer des données satellitaires dans le modèle hydraulique SW2D-DDP proposé afin de le calibrer et d'améliorer ses prédictions dans un premier temps, et dans un deuxième temps, dans le but d'estimer un paramètre hydraulique souvent inconnu et nécessaire en entrée des modèles hydrauliques : la bathymétrie. Il existe d'autres paramètres hydrauliques importants tels que le coefficient de frottement qui peuvent être calibrés avec la bathymétrie. Basé sur une étude de sensibilité menée par Antoine Pfefer (stagiaire à l'INRIA en 2021) en parallèle, nous avons remarqué que la sensibilité du modèle au coefficient de frottement est beaucoup plus faible que la sensibilité à l'altitude de fond de rivière. Permettant de aussi réduire le risque d'équifinalité, nous choisissons donc d'effectuer la calibration de modèle à porosité via le paramètre qui semble être le plus influant : la bathymétrie.

Dans cette étude, nous assimilons les cartes d'étendues en eau probabilistes des inondations, en provenance des images du radar à synthèse d'ouverture (RSO), dans le modèle SW2D-DDP, via un filtre à particules tempéré (Tempered Particle Filter : TPF). Pour réduire la dégénérescence et l'appauvrissement de l'échantillon, les TPF utilisent une approche itérative qui factorise la vraisemblance en utilisant des coefficients de tempérag. Cela augmente la variance de la vraisemblance et permet une transition lisse entre la probabilité *a priori* et la probabilité *a posteriori*. Un ré-échantillonnage (Sequential Importance Resampling : SIR) et des mutations sont effectuées pour regagner en diversité à travers les particules. L'algorithme d'assimilation de données est appliqué en utilisant le cas test de 2012 à la confluence des rivières Severn et Avon, où des données *in situ* à l'intérieur du domaine hydraulique – à Mythe Bridge et à Tewkesbury (voir emplacement sur Figure 1.3) – sont disponibles pour évaluation.

La calibration de toutes les mailles du lit de la rivière (au nombre de 93) peut résulter en des paramètres qui sont contrastés tout au long de la rivière. Nous proposons ainsi de réduire notre calibration à trois paramètres, situés aux trois limites du modèle hydrauliques (deux en amont et une en aval), et en déduire une bathymétrie interpolée linéairement avec deux pentes fixes correspondant à la Severn, entre Saxons Lode et Deerurst, et l'Avon, entre Bredon et la confluence (voir emplacement sur Figure 1.3). Nous proposons de faire un autre test avec une calibration encore plus simplifiée, où on calibre uniquement le paramètre en aval, et on en déduit les paramètres en amont en rajoutant un delta d'élévation estimé à partir des données topographiques. Le modèle SW2D-DDP (à calibrer) a été mis en place avec les paramètres suivant : une hauteur d'eau constante dans le lit de la rivière comme condition initiale, et en conditions aux limites : des hydrogrammes de débit en amont à Saxons Lode et Bredon, et une relation hauteur débit en aval à Deerhurst (estimation du nombre de Froude à partir d'une

---

simulation de contrôle effectuée dans l'étude du chapitre 1). Nous proposons d'établir un test supplémentaire qui consiste en une calibration du ou des paramètre(s) de bathymétrie avec une valeur de Froude fixe, et une valeur de Froude qui est calibrée. Par ailleurs, nous testons l'utilisation d'une couche d'exclusion pour tenir en compte des erreurs possibles des données issues des cartes RSO.

En termes de niveaux d'eau, pour la majorité des tests, les prédictions du modèle atteignent des RMSE inférieures à 0,5 m après assimilation. Les résultats montrent que la meilleure variante est celle qui repose sur la calibration des 3 paramètres distribués aux limites du modèle hydraulique. La calibration ou non du Froude n'affecte pas les résultats de l'assimilation. L'influence de la couche d'exclusion est limitée dans les tests effectués. D'autre part, en terme de bathymétrie calibrée, les paramètres après assimilation sont relativement éloignés des valeurs données par les mesures disponibles de sections en travers aux 3 stations.

## Conclusions et perspectives

Dans la première partie, nous avons proposé une chaîne de modélisation nouvelle, permettant de simuler rapidement les inondations à large échelle. En effet, le modèle à porosité SW2D-DDP [50] permet pour la première fois, une représentation précise de la bathymétrie et la topographie au sein de grandes mailles, en utilisant la porosité dépendante de la profondeur, ainsi permettant une réduction significative du nombre de mailles par rapport au modèle standard SW2D. La simulation de deux cas test réels de 2007 et 2012, sur une zone de 1500 km<sup>2</sup> autour de la confluence des rivières Severn et Avon, a montré les résultats suivants :

- l'approche de modélisation proposée permet de simuler des cartes d'inondation similaires à celles produites par le modèle standard SW2D, avec une précision allant jusqu'à 90 %.
- le modèle de porosité est capable de prendre en compte les petits drains dans des mailles comparativement très grandes. En revanche, leur représentation dans un modèle standard nécessiterait de très petites mailles, ce qui entraînerait un nombre de mailles beaucoup plus élevé et une demande de calcul d'autant plus importante.
- l'expérience montre que les simulations du modèle à porosité sont environ 350 fois plus rapides que celles du modèle standard, ce qui réduit considérablement les coûts de calcul pour des résultats comparables.

L'approche de modélisation proposée dans cette partie facilite l'estimation d'une bathymétrie effective, car celle-ci est représentée par les paramètres de porosité. Ceci ouvre de nouvelles perspectives à grande échelle, notamment dans des zones où les données bathymétriques ne sont pas disponibles.

Dans la deuxième partie, nous avons proposé l'algorithme WaSER, permettant la récupération automatique de cartes d'inondation raffinées et de niveaux d'eau distribuées, grâce à la

fusion de données satellitaires SAR et de données topographiques. Les résultats ont montré des cartes d'inondation WaSER en très bon accord avec une carte d'évaluation dérivée d'une photographie aérienne et des résultats du modèle à porosité présentés dans la partie 1, notamment lors de l'utilisation des approches HAND L. et DEM L. Globalement, les résultats obtenus avec WaSER sont améliorés par rapport à ceux obtenus avec SAR exclusivement, atteignant une précision globale de l'ordre de 86-91%. La méthode proposée contribue ainsi à améliorer l'efficacité de la détection de l'eau par rapport à la seule utilisation de la technique de cartographie des inondations SAR. Les cartes de niveaux d'eau issues de WaSER présentent la meilleure concordance avec les résultats du modèle SW2D-DDP lors de l'utilisation de l'approche DEM L. avec des données topographiques et des images SAR à haute résolution (RMSD = 0,69 m avec le CopDEM et RMSD = 0,52 m avec le LiDAR). Ceci est dû au fait que les ensembles de données à haute résolution contiennent des informations précises sur une topographie complexe, ce qui permet une bonne estimation des directions d'écoulement. Cependant, l'approche HAND G. donne de meilleurs résultats (RMSD = 0.90 m) en utilisant les données à moyenne résolution telles que le SRTM à 30 m et l'image Envisat à 150 m. En effet, le niveau de détail de l'information topographique doit être compatible avec la résolution de l'image SAR afin d'éviter la production d'artefacts. Alors que les travaux antérieurs dans la littérature [21] ont atteint une précision de l'ordre de 0,38 m pour les cartes WSE interpolées, l'algorithme que nous proposons a démontré des résultats légèrement moins précis mais du même ordre de grandeur, tout en proposant une approche innovante pour produire des cartes de WSE spatialement distribuées. Cette étude a également montré que la RMSD peut être davantage réduite, en fonction de la résolution des données topographiques et satellitaires disponibles, ainsi que de la taille de la fenêtre locale utilisée pour le lissage. La méthode WaSER proposée permet donc une cartographie d'inondation rapide à large échelle et devrait être testée encore sur d'autres sites d'application. Elle s'avère prometteuse pour pallier le manque de données dans les zones mal instrumentées. De plus, les données topographiques (par exemple CopDEM, SRTM) et les images satellites à haute résolution (par exemple Sentinel-1) sont disponibles gratuitement et à échelle globale, ce qui rend cette méthode facilement applicable partout dans le monde.

Dans la troisième partie, nous avons proposé un algorithme d'assimilation de données qui permet de combiner les sorties du modèle SW2D-DDP et les cartes probabilistes d'étendues inondées issues du RSO. Bien que les erreurs retrouvées sur les niveaux d'eau sont réduites (de l'ordre de moins de 0.5 m) grâce à l'assimilation, nous ne retrouvons pas la bathymétrie des données de profils en travers ponctuels, après assimilation. Ceci est certainement dû à l'estimation très simplifiée de la bathymétrie à travers la loi de porosité SW2D-DDP. En effet, l'assimilation permet avec peu de données, l'estimation d'une bathymétrie effective simplifiée (trapézoïdale) dans laquelle les paramètres de forme peuvent se compenser : largeur au fond, au miroir, pente de berge dans le lit mineur et majeur, etc. De plus, l'utilisation d'images SAR disponibles après le pic de crue uniquement, pourrait créer un manque de variabilité en terme de cartes d'inondation. Ainsi, il serait judicieux de tester cet algorithme avec plus d'images qui offrent

---

cette variabilité, pour améliorer l'estimation de la bathymétrie. En conclusion, les résultats de cette dernière partie sont encourageants et méritent d'être examinés davantage. La calibration de la bathymétrie et le Froude pourrait être bénéfique dans des zones peu instrumentées, où les paramètres hydrauliques et de géométrie du domaine sont en manque.

# General introduction

Anthropogenic activities greatly impact the dynamics of the global water cycle, which is expected to intensify with climate change and increase the risk of flooding [112]. The Floods directive by the European Union defines the term “flood” as “the temporary covering of land not normally covered by water”. Several types of floods can be distinguished<sup>2</sup>. Coastal flooding is often a combination of storm surges and unusually high tides. Flash flooding is caused by heavy and sudden rainfall that saturates the top layer of ground surfaces which can no longer drain properly the water excess, and leads to runoff. While this type of flooding can subside quickly, it can be fast moving and dangerous while it lasts due to the peak discharge reached within only a few hours. Riverine (also known as fluvial) flooding is one of the most common types of inland flood. It occurs when the river bursts its banks because it reached its maximum capacity due to increased streamflow. A flood becomes a problem for human activities and security when it hits for example agricultural or urban areas. When that hazard carries a potential damage and poses a threat to humans, environment, material and property assets, the flood is identified as a risk [66]. Therefore the risk of a population to a flood is defined through the risk triangle, where the risk is a combination of the potential magnitude of the hazard, the exposure of the population in terms of where it is located in relation to the impact of the hazard, and the vulnerability of the population in terms of how important the impact of the flood will be [106]. Damages caused by floods can be devastating on many socio-economic levels. In 2011, the Southeast Asian floods resulted in a total of 2,282 deaths and affected nearly 9.6 million people. In Thailand alone, economic damages were estimated for nearly 40 Billion US\$, and the 2011 flood event was marked as the worst in 60 years [116]. Flooding can also occur in well developed countries that highly invest in infrastructure and flood management planning. Europe has not been immune to severe flooding in the summer of 2021, despite its economic development and progress in science and technology. While infrastructure was not heavily impacted and emergency response was quick to act, the event resulted in 243 deaths [84]. A recent study analysed satellite images for 913 major floods worldwide from 2000 to 2018, and estimated an increase in flood exposure for 32 countries to which will join another 25 by 2030 [115]. This means that in less than 10 years, an additional 179.2 million people will be at risk of flooding (from floods with a 1% annual chance of occurring). Therefore, sharing knowledge and good practice is needed to adapt to this natural hazard all around the world. A better understanding of the flooding phenomena and its hydrological consequences is needed to improve our flood forecasting chains, through the careful analysis of past floods and the

---

<sup>2</sup><https://www.envirotech-online.com/>

---

calibration of flood forecasting models.

Hydraulic models are popular and powerful tools for the assessment of flood hazard and flood-induced damages. To enable an accurate representation of flood dynamics, the area of interest needs to be discretized into cells in a way that high-resolution topographic data represents well enough hydraulic structures that might affect flood dynamics. This often requires small cells, which leads to an increase of computation times and becomes particularly problematic when modelling large areas. Sub-grid models have tackled this challenge and gained a growing interest as they are a good compromise between accuracy and high computational efficiency. Indeed, they enable faster simulations as they use coarser computation cells while accounting for small-scale topography variations within these cells. For example, Lisflood-FP [12, 89] is a fast-running and relatively easy-to-set-up model that enables subgrid capability in the channel, while assuming a simplified channel shape and using a 1D approach for the channel flow simulation and a 2D approach for the floodplain. The adopted subgrid channel approach allows representing any river channel size, even below the grid resolution. However, the subgrid approach only applies to the river and the resolution in the floodplain has to be rather high to accurately represent floodplain flows and inundation extent. Other modelling techniques that have evolved over the past twenty years, rely on two dimensional shallow water models including the porosity concept as a way to upscale the traditional shallow water equations [17, 29, 49, 51, 52, 64, 110]. In these models, porosity is defined as the fraction of a computational cell/edge available to the flow, and it takes into consideration small-scale features of obstacles that affect the flow, using coarse grid cells, thus allowing the reduction of run time while preserving subgrid topography information.

Flood forecasting models require input data that is subject to two main challenges: 1) the lack of *in situ* data that provides water depth and/or flow discharges used as boundary conditions, and 2) the lack of river channel information about hydraulic parameters such as river width, bed friction and elevation, etc. The first issue lies in having enough spatially distributed data across an area of interest, and is due to data being rarely available at a sufficiently high resolution. Measurements *in situ* cannot be easily made because of the inaccessibility of water courses at flood peaks, and the decline of operational gauging stations worldwide [58]. In this context, satellite earth observation (EO) technology becomes an attractive alternative source of information for monitoring and mapping floods at a large scale [128]. Spaceborne sensors can acquire images for large zones, but at a coarse resolution and a usually low revisit time, and airborne sensors provide more accurate images only at a much smaller scale [32]. Optical imagery is often hampered by cloud cover, and can capture images only during the day. Radar sensors and more particularly Synthetic Aperture Radars (SAR), are performing regardless of the sun-illumination and the cloud cover. Moreover, they are popular in flood mapping because of their straightforward ability to detect water on open and calm water bodies rather easily, due to the specular reflection phenomena. While many efficient and automatic flood mapping algorithms already exist, to the best of our knowledge, there are currently only few

studies focusing on the automatic retrieval of water surface elevation maps from SAR images. In this context, we believe making use of SAR data, which is becoming more globally and freely available at a high spatial resolution (*e.g.* Sentinel-1 at 20 m spatial resolution), holds great potential for the estimation of water depth from space, and contributes to the compensation of the lack of *in situ* data and to the support of flood forecasting models.

The second issue faced in surface hydrology is the observation of certain hydraulic parameters through remote sensing derived techniques. For instance, digital elevation models do not provide ground elevation below the water surface. Knowing that river channel morphology is crucial as input to flood forecasting models, there is a number of studies focusing on retrieving this information by existing means. The hydrological community awaits for the future SWOT mission (to be launched on November 2022) to get key hydraulic variable measurements – water surface elevation, width and slope – for open water bodies larger than 250 m  $\times$  250 m. Meanwhile, to address the mentioned issue, some studies have relied on data assimilation – a mathematical approach whose goal is to optimally combine uncertain model predictions with uncertain observations – to estimate unknown parameters that are needed in forecasting models. Some of the proposed methods have been found particularly efficient in retrieving missing data in ungauged areas *e.g.* [13, 36, 40, 96]. In this context, DA techniques should be further exploited in order to retrieve unknown data that is essential for flood forecasting models.

In this context, this PhD thesis targets three main objectives:

1. Developing a fast hydraulic modelling framework applicable at a large scale while preserving high-resolution information,
2. Developing an algorithm to enable the automatic retrieval of water levels using only satellite earth observation and topographic data,
3. Developing a data assimilation framework enabling the retrieval of riverbed bathymetric characteristics using time series of satellite earth observation data.

Chapter 1 is from an article published in *Advances in Water Resources* [8], Chapter 2 has been submitted to *Remote Sensing of Environment* in June 2021 and is currently under review, and Chapter 3 will be submitted after the submission of the thesis. Chapter 3.5. briefly reviews the results obtained in the three parts of the thesis and proposes perspectives for future improvements.

# A porosity-based flood inundation modelling approach for enabling faster large scale simulations

*This chapter is adapted from [8] published in Advances in Water Resources*

Ayoub et al. 2022

---

1.1. Introduction . . . . .	15
1.2. Methodology and experimental setup . . . . .	18
1.2.1 Modelling framework . . . . .	18
1.2.2 Experimental design . . . . .	21
1.3. Study area, experimental data and model setup . . . . .	23
1.3.1 Model setup . . . . .	25
1.4. Results . . . . .	27
1.4.1 Evaluation of simulated flood extent maps . . . . .	27
1.4.2 Evaluation of simulated water level maps . . . . .	29
1.4.3 Evaluation of simulated water levels time series . . . . .	31
1.5. Discussion . . . . .	32
1.6. Conclusion . . . . .	35

---

## 1.1. Introduction

With the increasing risk of more frequent and severe floods [7] due to climate change and growing urbanization, there is a crucial need to make more investments in flood management. Impacts of floods include human, socio-economical and environmental losses. Poorly conducted hazard assessments can lead to inefficient risk management, from insufficient protective mit-

igation measures to expensive rebuilding of devastated areas [10, 82]. Instead, well-conducted flood risk assessments provide a valuable support for decision making related to urban planning and emergency response preparedness. Therefore, it is essential to improve flood management systems to better anticipate and further reduce potential flood risk [95, 114]. In this context, hydrological and hydraulic models play a central role in flood forecasting as they provide predictions of water streamflows and levels across various temporal and spatial scales [59, 101].

The most common flood inundation (hydraulic) models are based on the depth-averaged Navier Stokes equations, also called de Saint-Venant or Shallow Water Equations (SWE). The resolution of these equations can be carried out in one (1D) or two dimensions (2D). 1D models solve the 1D formulation of the SWE [12] where the flow is assumed to be unidirectional and water levels are assumed to be constant across sections. Although they are relatively easy to setup and fast to run [26], these models fail to provide accurate predictions of overbanking flow and in presence of complex topographies, especially because the momentum transfers between the channel and the floodplain are neglected. 1D-storage area models (also often referred to as 1D+ or quasi-2D) are sometimes preferred as they include a representation of floodplain storage using a series of user-defined polygonal compartments into which overbank flows can spill. The flow between the main channel and the floodplain storage cells is modelled using stage-discharge equations, such as weir, gate or orifice laws. These can also be used to link storage cells to one another, and the water level is then computed using volume conservation in each storage cell. However, these models also neglect the momentum conservation between storage areas in floodplains. To tackle the previously described issues, 2D approaches are adopted. In 2D flood modelling, a fine discretization of the area of interest (including main channel and floodplains) is required to accurately represent topography. Consequently, the main limitation of accurate modelling of large scale floods is associated with a very expensive computational cost. An alternative approach relies on the coupling of 1D and 2D models. This approach is not completely satisfying as it only accounts for mass transfers between the two models. The actual key for this approach to be reliable is correctly representing edges of the 1D and 2D models making it possible to keep the spatial and temporal correlations of 1D and 2D models consistent [131]. For instance, [125] represents the floodplain by fictitious river-branches for which the calibration of friction coefficients is required to account for momentum. A precise mapping of these branches is necessary to accurately delineate the flood extent that is otherwise often overestimated. [38] proposed a shallow water based model for river-floodplain interactions using 1D and 2D elements in the main channel and floodplain, respectively. This allowed to improve the portraying head loss phenomena that can happen due to channel bends or meander short-cuts, thanks to the inclusion of lateral momentum transfer between the river and the floodplain.

To correctly capture flood dynamics there is a need to further reduce the computational time while ensuring precise representation of river-floodplain connections. Sub-grid modelling approaches have tackled this challenge and gained a growing interest as they are a good compromise between accuracy and high computational efficiency. Indeed, they enable faster simulations

as they use coarser computation cells while accounting for small-scale topography variations within the cells. For example, Lisflood-FP is a fast-running and relatively easy-to-set-up model and its standard version was introduced by [12]. It was further developed by [89] who proposed a version enabling subgrid capability in the channel. This assumes a simplified channel shape and uses a 1D approach for the channel flow simulation and a 2D approach for the floodplain. The adopted subgrid channel approach allows representing any river channel size, even below the grid resolution. However, the subgrid approach only applies to the river and the resolution in the floodplain has to be rather high to accurately represent floodplain flows and inundation extent.

Other modelling techniques rely on two dimensional shallow water models including the porosity concept as a way to upscale the traditional shallow water equations. Porosity is defined as the fraction of a computational cell/edge available to the flow. Porosity-based models have evolved over the past twenty years. First, [29] introduces the shallow water model with isotropic porosity. The formulation for partially wet/dry areas over irregular domains is later improved by [17,30,56]. In the single porosity model [52] a differential formulation is derived using a finite volume scheme, which is further evaluated by [110]. Later, [104] shifts the focus from isotropic to anisotropic porosity by proposing the Integral Porosity model, where connective porosity (through edges) is distinguished from storage porosity (within cells). [49] then merges the isotropic and anisotropic models and introduces a multiple porosity approach for applications in urban areas. [64] investigates the porosity-based model errors and show that they are lower for anisotropic models than for isotropic approaches. This approach is further extended by introducing a Dual Integral Porosity (DIP) model [51]. The SW2D-DDP model was presented and evaluated in [50]. In this article, synthetic test cases (a series of dam-break configurations and a meandering channel) and an experimental test case were used to evaluate and validate the model results. Two closure laws (Integral Porosity and the depth-dependant Dual Integral Porosity) were compared to a fine 2D model that solves the classical shallow water equations with the second-order MUSCL-EVR scheme. Results show the superiority of the proposed DIP closure model on the IP model. Moreover, the paper presented a shallow water model based on the DIP approach, with depth-variable porosity fields: SW2D-DDP, and it has been found that although porosity approach cannot represent details within the cells, it shows good agreement with the average values of the fine 2D model. Moreover, the CPU ratio between DDP and fine 2D models ranges from 310 to 2900. In this paper, we apply and validate the SW2D-DDP model on a real large scale test case, since it was already evaluated on synthetic test cases in [50].

The provision of accurate bathymetric data is critical in hydrodynamic modelling, yet obtaining this information where in situ measurements are lacking is not always possible. In this context, [58] proposes a method for retrieving effective riverbed bathymetry based on the assimilation of water level measurements acquired by a drifting GPS buoy into a 1D hydraulic model and many bathymetry retrieval methods have been recently developed in the frame-

work of SWOT satellite mission preparation (*e.g.* [37, 93, 129]). In the perspective of retrieving bathymetry that is often unknown [68] [31], we propose here to represent it via depth-dependant porosity functions. We therefore hypothesise that bathymetry can be effectively represented through depth-dependant porosity parameters.

In this context, the main objective of this study is to develop and evaluate a modelling framework based on SW2D-DDP enabling fast flood inundation simulations at a large scale, while representing for the first time both bathymetry and small-scale floodplain topography using depth-dependant porosity within comparatively large computational cells. To evaluate the proposed modelling framework with scrutiny, we compare the SW2D-DDP simulation result with a standard 2D shallow water model on one hand. Moreover, we evaluate both model results using ground truth data (in situ measured and remote sensing-derived). Benchmarking the SW2D-DDP model against a high-resolution 2D model enables the evaluation of our approach across space and time. It also helps to explore strengths and limitations of the proposed approach in comparison with state of the art approaches. Our study site is a 1,500km<sup>2</sup> floodplain located at the confluence of the Severn and Avon rivers in the United Kingdom, which has frequently experienced flooding especially in the last decades. The 2007 and 2012 flood events are used as test cases.

The remainder of this paper is organised as follows. In section 3.2., we present the proposed modelling framework enabling the simplified representation of bathymetry and topography via porosity, and then the design of the experiment to evaluate the model performance. Next, the study site and available data, as well as the models set up are described in section 3.3.. In section 3.4., we evaluate the simulated flood extent and water level maps. Finally, section 1.5. discusses the main outcomes of the study.

## 1.2. Methodology and experimental setup

This section first describes the proposed modelling approach based on the shallow water 2D model with SW2D-DDP. Next, it presents the experimental setup for evaluating the model performance using a standard 2D shallow water (SW2D) model as a reference, as well as in situ measured and remote sensing-derived data.

### 1.2..1 Modelling framework

SW2D<sup>1</sup> is a modelling suite that has been progressively developed and further improved since 2002. It solves the 2D shallow water equations with a finite volume scheme on structured or unstructured grids. The SW2D-DDP model [50], introduces a Depth-Dependant Porosity that accounts for small-scale effects of obstacles to the flow in a macroscopic way without the need to detail their geometry in the mesh. Although the whole domain is represented as flat in the

---

<sup>1</sup><https://SW2D.inria.fr/>

mesh, a bottom elevation  $z_b$  is provided inside each cell via a porosity distribution as a function of the water depth.

Within a domain  $\mathcal{D}$ , the model distinguishes storage (cell) porosity  $\phi_\Omega$  from edge (connective) porosity  $\phi_\Gamma$ . The domain-based porosity takes into account the mass and momentum storage and the edge-based one takes into account the mass and momentum transport [70]. The storage porosity for a given cell is the adimensional area available for water at the elevation  $z_s$ . As detailed in [50], the standard shallow water equations are multiplied by the phase function  $\varepsilon$ , defined as:

$$\varepsilon(x, y, z) = 1 \text{ if } z > z_b, 0 \text{ otherwise} \quad (1.1)$$

where  $\varepsilon(x, y, z)$  is the phase indicator for the point coordinates  $(x, y, z)$  that is equal to 0 if the point is in the solid phase (i.e. lower than the bottom elevation  $z_b$ ). The porosities represent the amount of water that can be stored per unit domain and boundary for a unit variation in the free surface elevation  $z_s(x, y)$ , which is assumed to be known. Thus, the porosities over cells ( $\Omega$ ) and edges ( $\Gamma$ ) are defined as:

$$\phi_{\mathcal{D}}(z) = \frac{1}{\mathcal{D}} \int_{\mathcal{D}} \varepsilon(x, y, z) d\mathcal{D}, \quad \mathcal{D} = \Omega, \Gamma \quad (1.2)$$

where  $\mathcal{D}$  stands for either a cell ( $\Omega$ ) or an edge ( $\Gamma$ ). This allows to uniquely define the volume of water stored per unit area/length in the sub-domain  $\mathcal{D}$  between the ground and the elevation  $z$  as:

$$\theta_{\mathcal{D}}(z) = \int_{-\infty}^z \phi_{\mathcal{D}}(\zeta) d\zeta \quad (1.3)$$

Small scale topography information is therefore taken into account via porosity laws [50]. In the SW2D-DDP software, four law types are proposed. In this model setup, we have chosen to use only two types of porosity law (0 and 3) for the sake of simplicity and in order to show how porosity represents and preserves high resolution topographic data.

Law 0 is used for defining storage porosity in the floodplain (Fig. 1.1). The distribution of ground elevations  $z_b(x, y)$  within each cell is first retrieved from the digital elevation model (DEM). Next, it is discretised using a piecewise constant function of  $N$  segments with ‘‘equidistant’’ porosity values associated to elevation values with the following relation:

$$\phi(z_i) = i/N, i = 1 \dots N \quad (1.4)$$

where  $z_i$  is the subgrid water depth associated to a porosity  $\phi_i$  and  $N$  is the number of segments.

Law type 3 allows us to handle porosities inside riverbed cells. In line with the objective of minimising the number of cells in the model mesh and therefore reducing computational time, we propose to define cells with dimensions larger than the riverbed width. Moreover, to avoid elongated cells that can be responsible for model instabilities, we maintain the length of

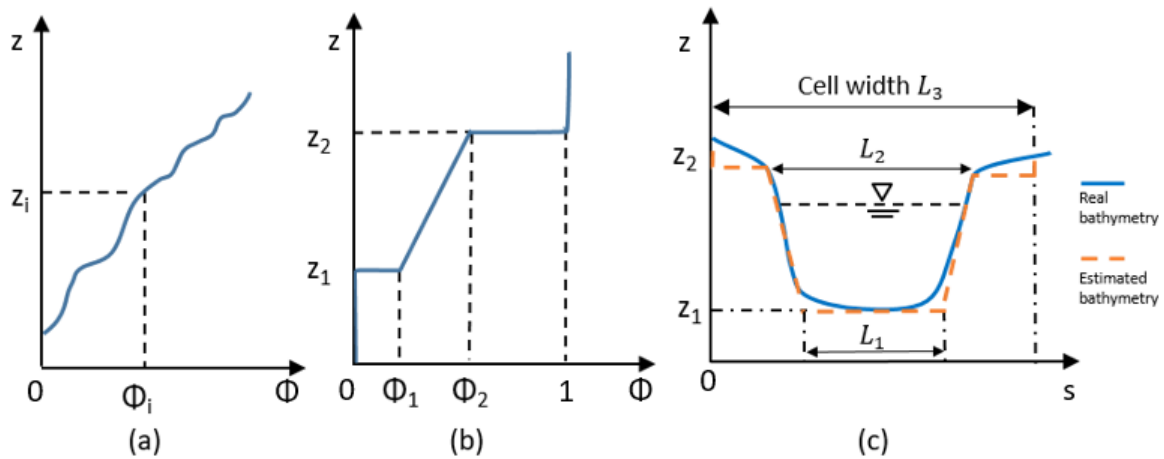


**Figure 1.1:** Porosity laws: a) law type 0; b) law type 3; c) bathymetry representation using law type 3.  $z$ : elevation,  $\phi$ : porosity,  $s$ : abscissa along the river cross-section.

the computational cells along the streamflow direction at maximum twice its width (Fig. 1.2). Since bathymetric data is rarely available, we propose to represent riverbed geometry using a simplified trapezoidal shape assumption via the porosity law type 3 (Fig. 1.1).

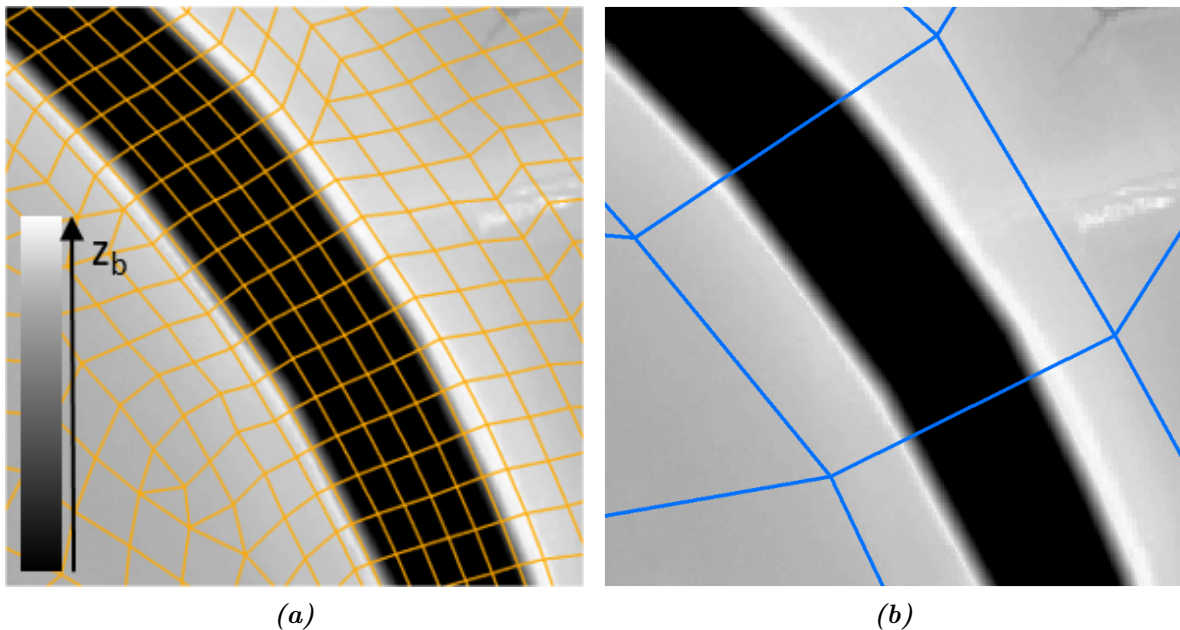


**Figure 1.2:** 0.25 km<sup>2</sup> subset of: a) the standard model mesh, b) the porosity model mesh.

First, storage porosities are computed. Then, the porosity law type used for the edges is selected depending on the location of their adjacent cells: law type 3 is used inside the riverbed (cross sections, i.e. edges between two cells of type 3) and law type 0 is used in the floodplain (between two cells of type 0) and on river banks (between a riverbed and a floodplain cells). To accurately represent overbank flows, the nodes of the river bed cells are positioned on the dikes in both models. Indeed, when positioning interfaces upon constrictions and obstacles,

these latter are implicitly considered in the interface flux calculation, while the same obstacles disappear from the numerical representation when they are located inside the cells. Moreover, to ensure that high points are correctly taken into account without too much overloading the mesh design process, we choose to automatically compute the edge porosity values as the minimum of the porosities of their neighbouring cells. It is worth mentioning that the parameter retrieval of the porosity law in each cell and edge is carried out automatically using the available DEM and bathymetric information.

### 1.2..2 Experimental design

To the best of our knowledge, our modelling framework enables for the first time to represent both riverbed and floodplain subgrid topography using porosity laws. To evaluate its advantages and limitations, we compare the SW2D-DDP model with a standard fine 2D model, namely SW2D [62], in terms of simulated water depths and inundation extents. Moreover, to further assess our modelling approach, we evaluate it against observed flood extents from aerial photographs and satellite images, and against observed water level time series from in situ measurements when available.

#### 1.2..2.1 The standard 2D shallow water model

To enable a meaningful comparison between the two approaches, the standard model has to use exactly the same input data as the porosity model: topography, bathymetry, boundary and initial conditions and parameters (*e.g.* friction coefficient, numerical scheme). The two models differ only in the way they represent the floodplain and riverbed topography. The standard model being based on a classical finite volume scheme, the bottom elevation inside a computational cell has a unique value, equal to the average elevation of the cell's nodes. As a consequence, topography can be smoothed out within each cell, when flow obstructions, drains or structures (*e.g.* dikes, roads, streams) are not intrinsically represented via cells smaller than their dimensions. Indeed, adequately representing dikes, drains or river channels, requires to include several mesh cells within each of these structuring elements. Therefore, in the standard SW2D model, the mesh needs to be designed in a way that entire cells are placed explicitly on hydraulic structures or singularities. For instance when representing a drain of 5m width, cells have to be well-placed to capture its effect, otherwise it would be transparent for the model. Having many of these structures in large scale areas would require a long time to represent them in a standard SW2D model.

#### 1.2..2.2 Evaluation method

To evaluate the porosity model performance, we propose an approach composed of several successive steps detailed in the following paragraphs: i) post-process model results to derive flood extent and water depth maps in the same format, ii) compare flood extent and water level maps extracted from both models, on a daily basis; iii) evaluate flood maps extracted from both mod-

els using remote sensing derived data; and iv) evaluate simulated water level time series against in situ observation data. In this study we chose to evaluate the proposed modelling approach in terms of simulated water levels first using punctual in situ water level measurements. Next, as spatially distributed water level cannot be derived from in situ observation, we also compare the SW2D-DDP results with those obtained using the standard SW2D model. Whether we use the SW2D model results or the measurements provided by a camera or a gauging station to evaluate water levels, we computed the root mean squared deviations (RMSD, eq. 1.7). When we evaluate the model in terms of flood extents, two types of references are used : i) the flood extent maps simulated by SW2D and ii) the ones derived from a satellite imagery.

**Post-processing of model results:** We aim to compare the results of the porosity and the reference models in terms of flood extents and water levels. By definition, the bottom elevation of the cells in the porosity and standard model meshes are taken into account differently. In the standard SW2D model, as previously mentioned, the bottom elevation of a cell corresponds to the average elevation of its nodes. In the porosity model, the subgrid elevation variability is accounted for via the porosity. Since the edges of the fine and coarse grid cells do not overlay, the flood extent maps derived from the two models are resampled to the original DEM resolution (2m), to enable a pixel-to-pixel comparison. To do so, the cell is considered flooded when the simulated water depth reaches a minimum value  $h_{\min}$  i.e. when  $z_s > z_b + h_{\min}$  where  $z_b$  is the cell bottom elevation for the standard model and the DEM elevation for the porosity model). The  $h_{\min}$  is set to 0.1 m, which corresponds approximately to the vertical accuracy of the LiDAR DEM.

**Evaluation of simulated flood extent maps:** The simulated flood extents evaluation is carried out twice, using as a reference either (i) the standard model or (ii) the available Earth Observation data. Based on a pixel-by-pixel comparison, we compute a confusion matrix composed of four metrics: 1) the number of pixels that are unflooded in both maps, i.e. TN: true negatives, 2) the number of pixels flooded only in the standard model, i.e. FN: false negatives, 3) the number of pixels flooded only in the porosity (SW2D-DDP) model, i.e. FP: false positives, and 4) the number of pixels flooded in both maps, i.e. TP: true positives. To compare the simulated and the reference maps, we compute contingency maps. As overall performance metrics we use the Critical Success Index (CSI) [105] and the Overall Accuracy (OA) that are both derived from the confusion matrix. CSI and OA quantify the goodness of fit between the evaluated map and the reference maps (see Eqs. 2.4 and 2.3). The CSI represents the ratio of the number of pixels correctly predicted as flooded (TP) over the number of all flooded pixels:

$$\text{CSI} = \frac{\text{TP}}{\text{TP} + \text{FP} + \text{FN}} \quad (1.5)$$

The OA takes into account the agreement of non flooded areas and is defined as follows:

$$OA = \frac{TP + TN}{TP + FP + FN + TN} \quad (1.6)$$

These scores vary between 0 and 1, with the highest value attained when the predictions present a perfect fit with the reference.

**Evaluation of simulated water level maps:** To quantitatively measure discrepancies between the simulations and reference water level maps, we use the root mean square deviations (RMSD, Eq. 1.7) between the porosity model predicted water levels  $z_{i,sim}$  and the reference water levels  $z_{i,ref}$  (eq. 1.7), resampled at the DEM resolution (2m), and for each of the  $n$  inundated pixels of the entire domain.

$$RMSD = \sqrt{\frac{1}{n} \sum_{i=1}^n (z_{i,sim} - z_{i,ref})^2} \quad (1.7)$$

Moreover, to further evaluate the distribution of the differences between the simulated and reference water levels, we make use of boxplots showing the deviation distribution based on statistical metrics: 1) the lower bound; 2) the first quartile, Q1=25th percentile; 3) the median, Q2=50th percentile; 4) the third quartile, Q3=75th percentile and 5) the upper bound. The interquartile range (IQR) goes from the 25th to the 75th percentile, and therefore represents 50% of the data values. The maximum value of the boxplot is defined as  $Q3 + 1.5 \cdot IQR$ , and the minimum value  $Q1 - 1.5 \cdot IQR$ . Outlier points are thus eliminated from the plot for the sake of readability.

**Evaluation of simulated water levels time series:** Water level time series obtained from each of the porosity and standard models are evaluated against in situ observation data. For visual comparison, these time series are plotted. Then, to quantitatively measure the discrepancies, we compute the root mean square deviations (RMSDs), as described in the previous section.

### 1.3. Study area, experimental data and model setup

The Severn, the longest river in Great Britain, extends from its source at Plynlimon in the Welsh hills to the mouth of the Bristol channel. The overall catchment area covers approximately 11,000 km<sup>2</sup> and is predominantly rural, apart from some urban settlements like Worcester, Tewkesbury and Evesham. Fig. 1.3 shows the model domain and river network with the location of the available gauging stations and the camera location offering live imagery on the river Severn. The study site is located at the confluence of rivers Severn and Avon around the city of Tewkesbury and has been subject to frequent flooding due to intense precipitation. The area of interest covers approximately 15 × 10 km<sup>2</sup>. Two flood events of different magnitude will be simulated and analysed to better understand the model behaviour with changes in boundary conditions: the July 2007 and November 2012 flood events.

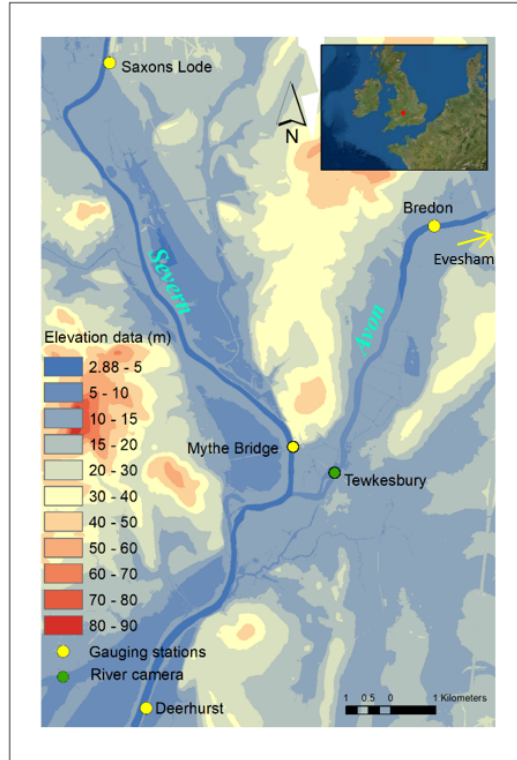


**Figure 1.3:** Study site: model boundaries and location of the gauging stations and the river camera. The background colours illustrate the classification of ground elevation.

**Hydrometric data:** Two suitable gauging stations are located at Saxons Lode (along the Severn River) and Evesham (along the Avon River) upstream of the confluence. Due to the backwater effect observed at Bredon, the streamflow time series is estimated there from that recorded at Evesham gauging station (located upstream of Bredon) and delayed in time based on an estimated wave travel time. Mythe Bridge is situated upstream the confluence of the Severn-Avon rivers and Deerhurst is situated downstream. Hydrometric data are provided by the UK Environmental Agency (EA) at 15 min-intervals. Moreover, the Tewkesbury stationary camera (Fig. 1.3) mounted on the wall of a building in March 2011, provided a view on the Avon river, which allowed taking hourly daylight images during the 2012 flood event. This camera enabled the estimation of water levels in the river [122], which are used to evaluate the hydraulic model performance inside the domain.

**Earth observation data:** The flood event of July 2007 is particularly interesting because an airborne campaign imaged the flood at a very high resolution (50 cm) on July 24, close to the flood peak [44]. Flood extents were manually digitised on this imagery. This extracted flood map allows evaluating the simulated flood extents at the same date (24 July). The hierarchical split-based approach proposed by [19] is used to derive flood extent maps from the Cosmos-SkyMed images acquired on the following dates: 27, 28, 29, 30 November and 01, 02, 04 December 2012.

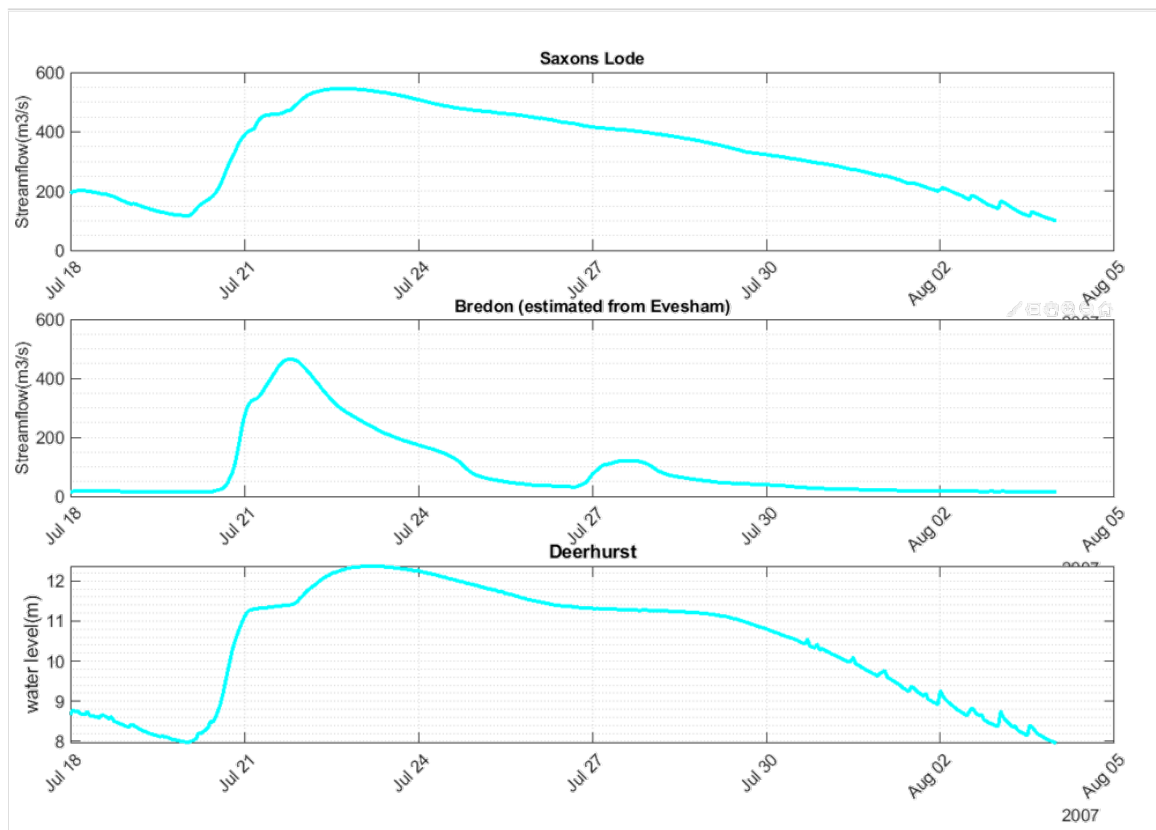
These flood maps are considered for evaluating synchronous flood extent maps simulated by the porosity and the standard models.

**Topographic and bathymetric data:** A LiDAR DEM at 2m-spatial resolution with a vertical accuracy of 0.10 m provided by the UK Environmental Agency (EA) [126] is used to provide the model with ground elevation. Bathymetric data is reconstructed using three river cross section measurements at the upstream (Saxons Lode and Bredon) and downstream (Deerhurst) boundaries of the model. To do so, first, we approximate the observed cross sections using a trapezoidal shape. The bank lines are manually digitized along the Avon and Severn river streams and river stream bottom lines are automatically generated as parallels to the bank lines (using a distance estimated based on the observed cross sections). Next, the bank elevations are estimated by extracting ground elevation (provided by the Lidar DEM) along the bank lines. Then, the river bottom elevation is linearly interpolated between the three trapezoidal cross sections along the Avon and Severn bottom lines. Based on the river banks and bottom lines (with associated elevation values) we interpolate river bathymetry. Finally, the interpolated bathymetric data is merged with topographic data to form a single model input.

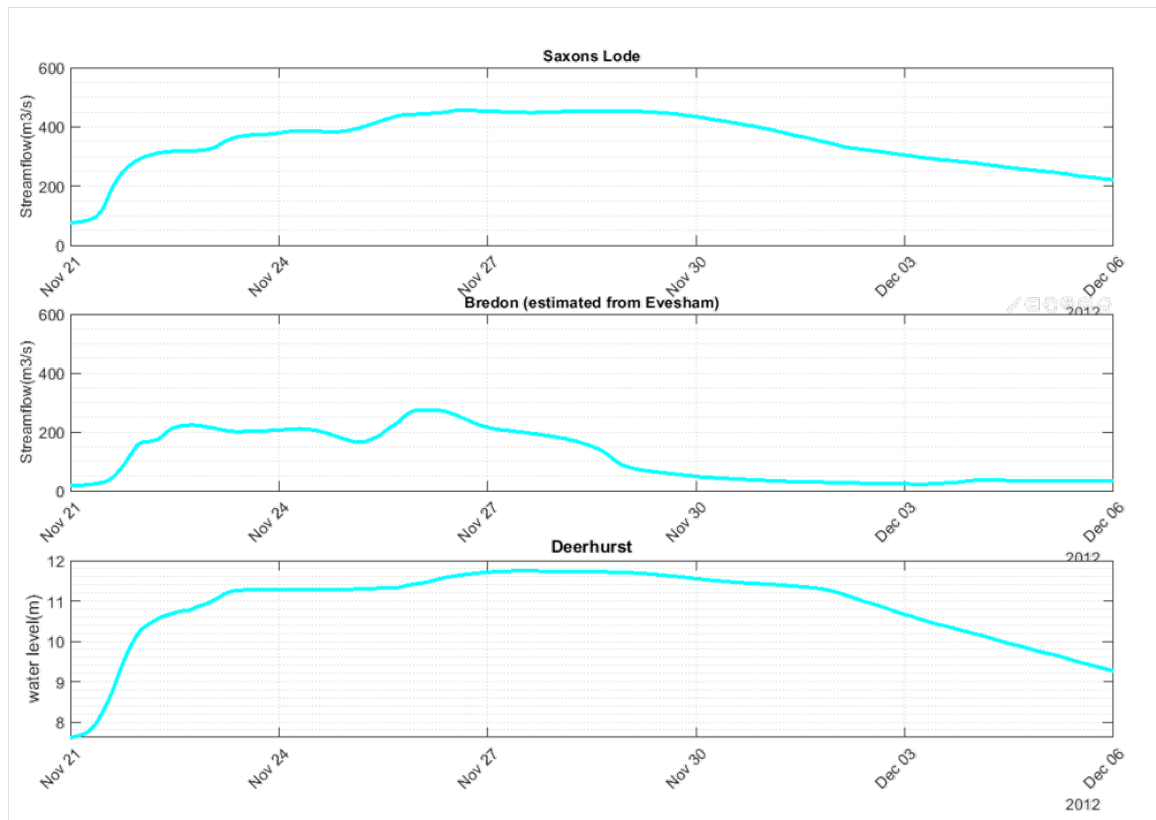
### 1.3..1 Model setup

While the standard model mesh is composed of 29,772 cells, the porosity model mesh contains only 1,042 cells. Concerning the mesh design in the SW2D-DDP model, just like in any other hydraulic model, the cell including the river should not be too large as the porosity law used in river cells considers the flood plain as horizontal (rectangular above trapezoidal shape). For other cells, no brutal variations in terms of surface should be found between adjacent cells. The influence of the number of tabulations  $N$  inside a cell has been investigated in [50]. Since the spatial information is lost within a coarse grid cell, it is essential to ensure that obstacles are captured by the 5 tabulation levels.

Discharge time series are imposed as upstream boundary conditions of the hydraulic model (Severn at Saxons Lode and Avon at Bredon). The streamflow time series in Saxons Lode are derived from water surface elevation records using a rating curve. Water level time series are used as downstream boundary condition at Deerhurst (fig.1.4). The initial condition is a fixed water level equal to the downstream condition. A uniform Strickler coefficient  $K_s = 50 \text{ m}^{1/3}\text{s}^{-1}$  is used for the riverbed and the floodplain. Spatially distributed parameters could easily be prescribed but a sensitivity analysis (not shown in this paper) showed that the influence of the friction coefficient was limited for the studied flood event. The durations of 2007 and 2012 flood event simulations are 17 days (18 July - 04 August) and 15 days (21 November - 06 december), respectively.



(a)



(b)

**Figure 1.4:** Model boundary conditions for the 2007 (a) and the 2012 (b) flood events: Upstream streamflow (Saxons Lode and Bredon) and downstream water level (Deerhurst) time series.

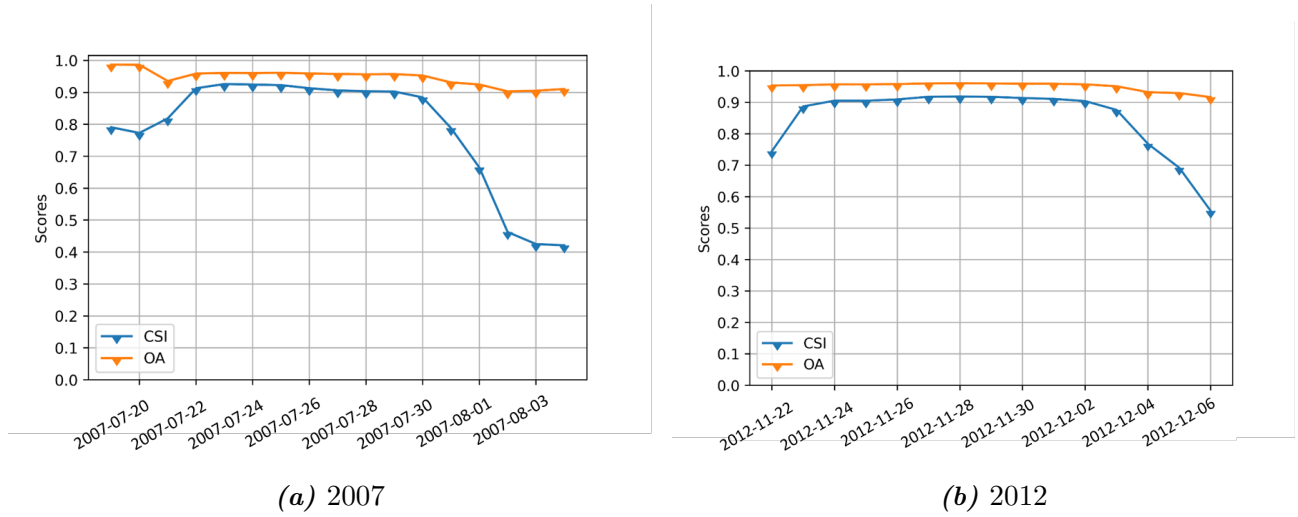
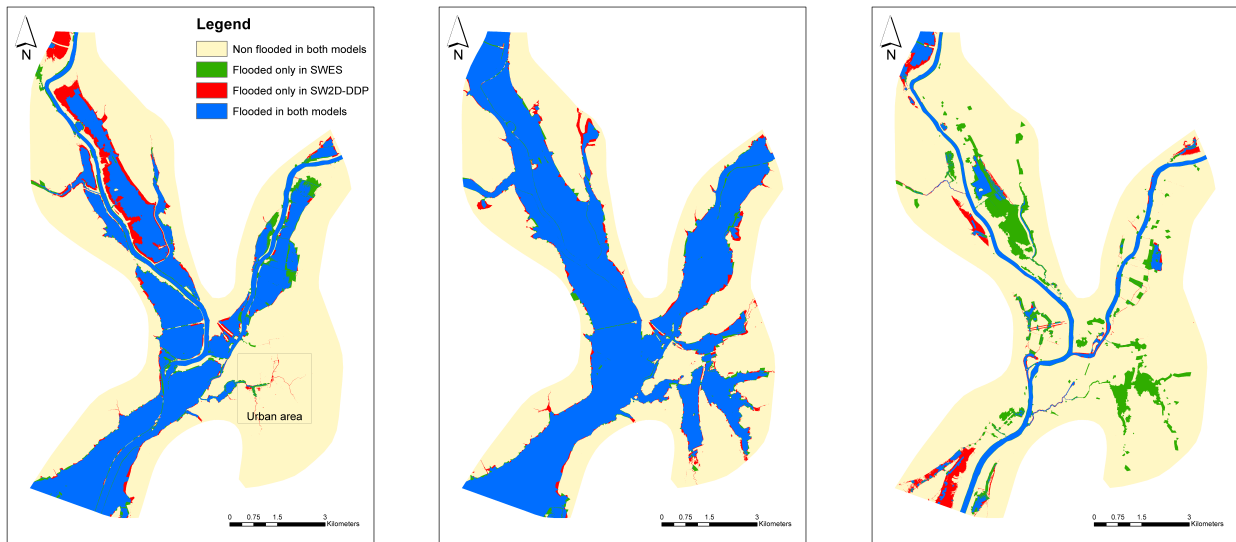


**Figure 1.5:** CSI and OA scores time series showing agreement between simulated (porosity) and “reference” (standard) flood extent maps, CSI: Critical Success Index & OA: Overall Accuracy.

## 1.4. Results

### 1.4.1 Evaluation of simulated flood extent maps

Fig. 1.5 shows the CSI and OA time series computed on a daily frequency for evaluating the SW2D-DDP simulated flood maps using the SW2D simulated flood maps as reference. It can be seen that both simulated flood extent maps are most of the time in agreement for both flood events. At the flood peak, in Fig. 1.6b and 1.7b, there is a very good agreement between the two models (accuracy of 95%). The model agreement is slightly lower in the rising limb, and decreases more in the falling limb. This implies that the draining dynamic in the SW2D-DDP model is different from that in the SW2D model. Fig. 1.6 and 1.7 show a series of contingency maps obtained by comparing the simulated flood extent maps (by the SW2D-DDP and SW2D models) during the 2007 and 2012 flood events. During the rising limbs (Fig. 1.6a and 1.7a) the porosity model exhibits a good agreement with the standard model, while locally inundating slightly larger areas especially in the upstream part as well as in little drains in the urban zone, at the Severn-Avon confluence (see box in Fig. 1.6a). This indicates the porosity model induces overbanking earlier than the standard model. Oppositely, a smaller inundation extent is visible locally nearby the Avon river. Fig. 1.6c and 1.7c show a substantially larger flood extent simulated by SW2D. This indicates that almost all floodplain water came back to the stream in the SW2D-DDP simulation while a substantial volume of water remains present in the floodplain in the SW2D simulation. This effect is dominant in the eastern Severn floodplain and around the urban settlements. Overall, Fig. 1.6c and 1.7c suggest that the porosity model fills in and drains floodplain water faster than the standard model. To better understand and assess this aspect, we also compare both model results to remote-sensing derived data.

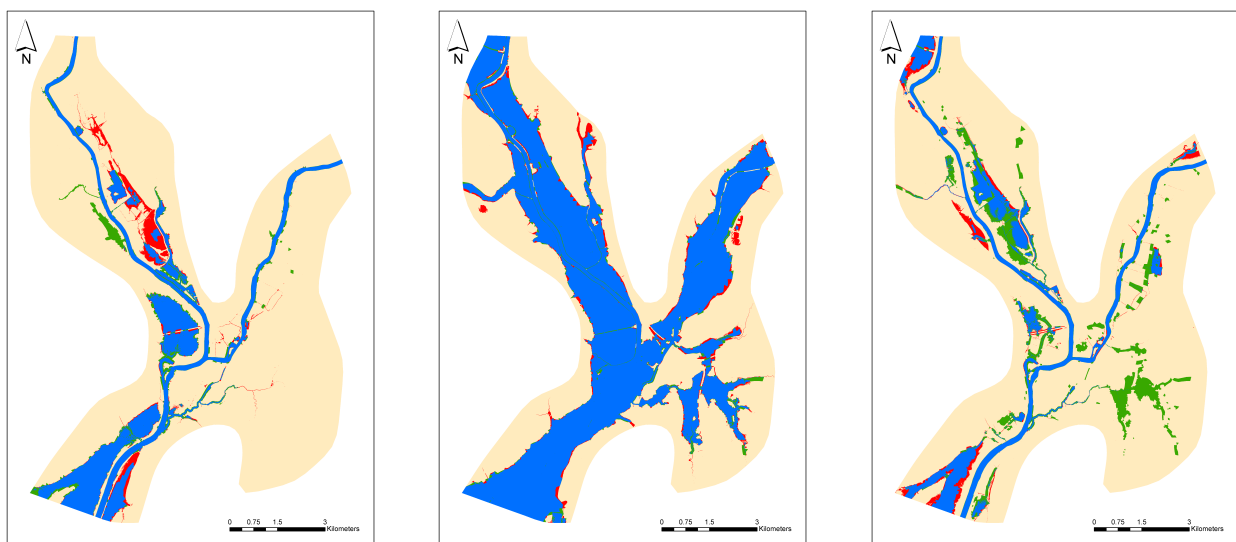


(a) Day 3 - 2007

(b) Day 7 - 2007

(c) Day 16 - 2007

**Figure 1.6:** Contingency maps between porosity and fine models for simulation days 3, 7 and 16 of the 2007 flood event



(a) Day 1 - 2012

(b) Day 5 - 2012

(c) Day 15 - 2012

**Figure 1.7:** Contingency maps between porosity and fine models for simulation days 1, 5 and 15 of the 2012 flood event

**Table 1.1:** Performance of the flood inundation extents simulated by the porosity (SW2D-DDP) and standard (SW2D) models computed using as a reference the satellite flood extent maps available for the 2007 and 2012 events. CSI: Critical Success Index; OA: Overall Accuracy.

Year	2007		2012					
Day	25-07	27-11	28-11	29-11	30-11	01-12	02-12	04-12
CSI (SW2D)	0.9	0.691	0.677	0.687	0.649	0.658	0.657	0.453
CSI (SW2D-DDP)	0.92	0.699	0.687	0.698	0.655	0.665	0.667	0.506
OA (SW2D)	0.94	0.852	0.847	0.855	0.843	0.848	0.853	0.866
OA (SW2D-DDP)	0.95	0.856	0.851	0.86	0.844	0.851	0.857	0.894

For the 2007 event, the porosity and standard model-derived flood maps were evaluated against the flood map extracted from aerial photography, and showed similar levels of agreement (CSI=0.92; OA=0.95 and CSI=0.9; OA=0.94 respectively for SW2D-DDP and SW2D). During the 2012 flood simulation, both models are in good agreement, with lower scores for the last satellite image (04 December, see Table 1.1). CSI and OA are rather similar for the two models but it is worth highlighting that the metrics of the porosity model are always exceeding those of the standard model. Fig. 1.8 shows the contingency maps computed by each of the models using as a reference the satellite flood map acquired on December 04. The most important differences between the two simulated flood extent maps are exhibited close to Tewkesbury where SW2D-DDP drains water faster than SW2D. The flood extent map derived from SW2D therefore exhibit in Fig. 1.8a a substantial overestimation when compared to the flood extent map derived from a Cosmo-SkyMed image. However, this overestimation has to be interpreted carefully as SAR backscatter images do not enable floodwater detection in dense urban areas [20]. Moreover, [44] showed for the same study area that part of the floodwater was detectable during the 2007 flood event inside Tewkesbury using a high resolution SAR backscatter image (i.e. a Terrasar-X image). As a consequence, one can argue that the absence of floodwater within Tewkesbury in the Cosmo-SkyMed images acquired in 2012 lends more weight to the SW2D-DDP flood extent map reliability.

### 1.4..2 Evaluation of simulated water level maps

Fig. 1.9 shows time series of root mean square deviations (RMSD) calculated between the porosity and standard model-derived water levels at a daily frequency, across the inundated areas. The corresponding time-averaged RMSDs are equal to 12.32 cm and 6.3 cm for the 2007 and the 2012 flood events respectively. The highest deviations are observed in the falling and rising limbs. During the flood, peaks are reduced and vary between 3 and 9 cm. From a practical point of view, depth deviations ranging from 10 to 15 cm in flood predictions can arguably be considered as acceptable given the vertical accuracy of the LiDAR used:  $\pm 10$  cm [75, 103]. Furthermore, boxplots are used to assess the distribution of differences between water levels simulated by the porosity and the standard models at a daily time step (Fig. 1.10). At first sight, it is found that the model results present a very good agreement at the flood peak

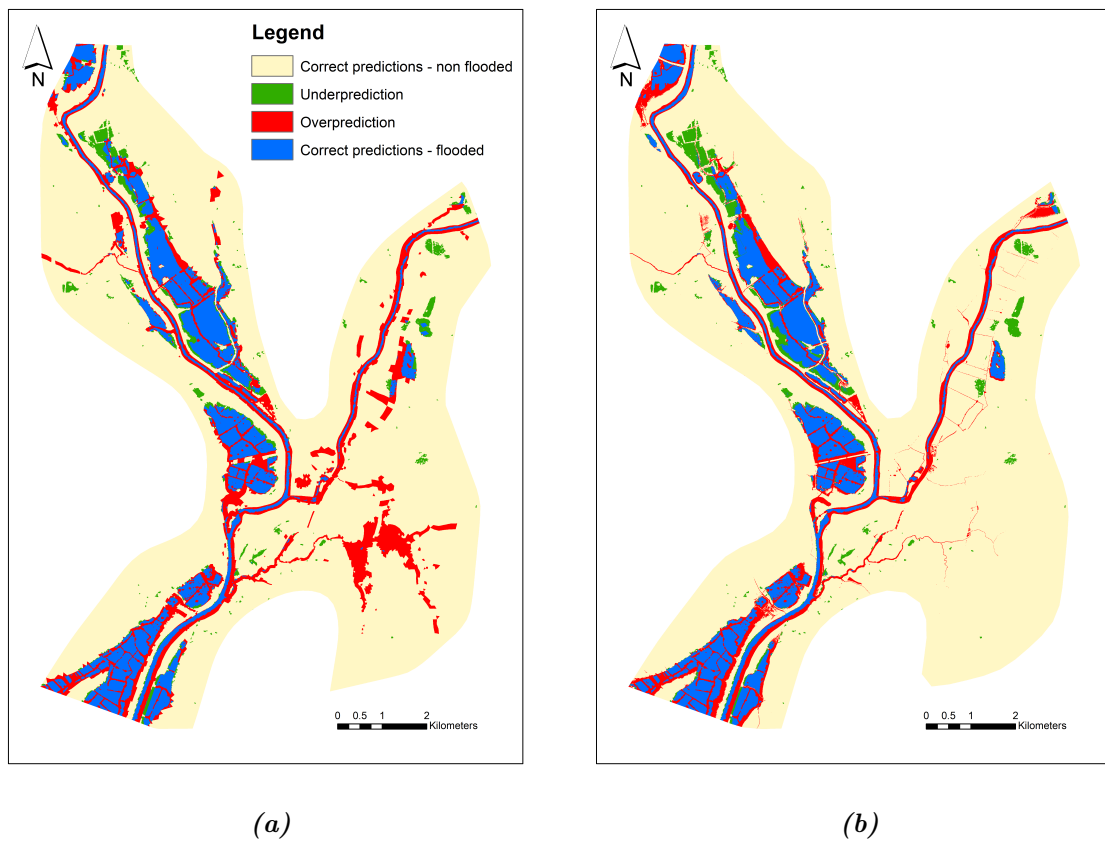
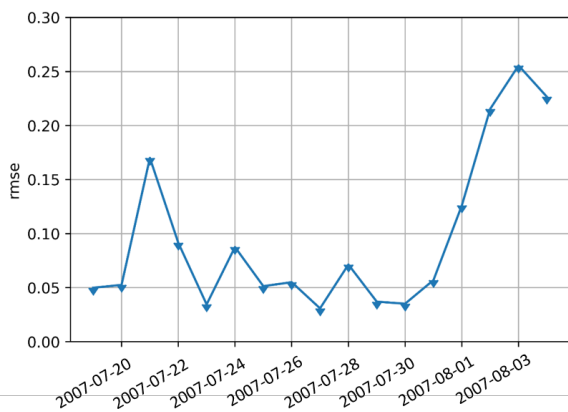
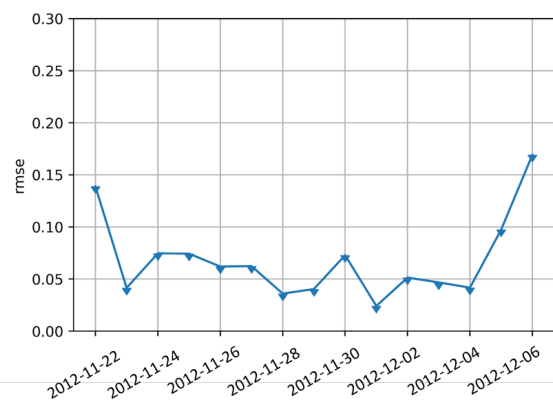


**Figure 1.8:** Contingency maps computed from the satellite and each of the standard (a) and porosity (b) model flood maps, on December 04, 2012.



(a) RMSD 2007



(b) RMSD 2012

**Figure 1.9:** Root mean square deviations (RMSD) in meters, between SW2D-DDP and SW2D simulated water level maps (resampled at DTM resolution): a) 2007 and b) 2012 flood events.

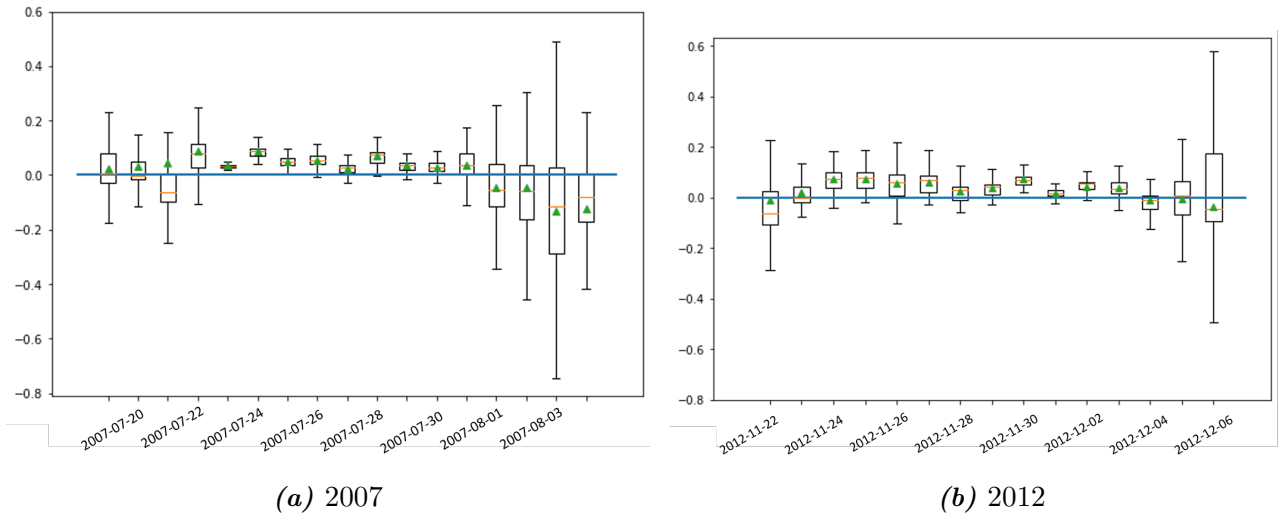


**Figure 1.10:** Boxplots drawn from the simulated water level deviations using as a reference the standard model - orange line: median; triangle: mean; box: interquartile range; whisker ends: the lower and upper bounds: (a) 2007 and (b) 2012 flood events.

since the boxplot height is very small. Positive values in the boxplots refer to higher water levels simulated by the porosity model. This is mainly observed during the rising limb and at the flood peak. This indicates that the porosity model simulates the overbanking earlier. This result is in agreement with the larger water extent simulated by the porosity model (see Fig. 1.6a and 1.7a). During the falling limb, lower values of water levels simulated by the porosity model express a larger inundation extent computed by the standard model, as obtained in (Fig. 1.6c and 1.7c).

### 1.4..3 Evaluation of simulated water levels time series

Simulated (porosity and standard model) water level time series are first evaluated using in situ observations at the Mythe Bridge hydrometric station and second using water levels estimated from the Tewkesbury camera images. When inter-comparing the two models, the results present a very good agreement (Fig. 1.11a, 1.11b and 1.11c). The highest discrepancies of simulated water levels compared to the gauge observations (0.90 and 0.60 m) are reached just before the 2007 flood peak (Fig. 1.11a) and on the first day of the 2012 flood simulation (Fig. 1.11b), respectively. The evaluation further shows reduced model errors during the falling limb of the 2012 flood event where the porosity model exhibit an error of less than 5 cm approximately. This is probably related to the initial condition fixed in the simulation that is set as uniform and fits the downstream level (Deerhurst). On another note, RMSDs are slightly improved, albeit not significantly, in the porosity model (Fig. 1.9). Both model results are also assessed using the camera images at Tewkesbury (see location in Fig. 1.3). The highest discrepancies with the gauge data are found in the rising limb. They are reduced when approaching the flood peak and almost fit the model results at the falling limb. Table 1.2 shows the porosity and standard model scores, using the RMSD metrics computed on water level time series. The considered

**Table 1.2:** RMSDs computed between the water level time series simulated by the porosity (SW2D-DDP) and standard (SW2D) models and Mythe Bridge gauge data for both flood events and Tewkesbury camera data of the 2012 flood event; RMSD: root mean square deviation.

	Mythe Bridge (2007)	Mythe Bridge (2012)	Tewkesbury (2012)
RMSD (SW2D)	0.388	0.255	0.444
RMSD (SW2D-DDP)	0.371	0.237	0.425

reference is the data observed at Mythe Bridge for the 2007 and 2012 events and at Tewkesbury for the 2012 event.

## 1.5. Discussion

As described in section 1.4.2, the water depth deviations of the porosity-based model with respect to the standard SW2D model, are acceptable given the vertical accuracy of the LiDAR used (c.a. 10 cm). The average flow depth in the rivers estimated over the entirety of the flood event, is about 7 m. Generally speaking, the average errors (c.a. 6 to 12 cm) are not substantial. High errors - reaching a maximum of 25cm - are observed in the rising and the falling limb, where the porosity model seems to fill in and evacuate faster than the standard model. On the other hand, errors with respect to the gauge/camera data reach a maximum of 60 to 90 cm respectively. Since the real bathymetry and bed-shape of the river are unknown, this potentially affects the simulation results in general, and can be further improved.

In Fig.1.11, the simulated levels at Mythe Bridge are lower than the observed ones, especially during the rising limb and the flood peak. This is arguably due to the simplified representation of the bathymetry in the models and to an underestimated upstream inflow for the Severn River at Saxon's Lode under high flow conditions. Indeed, as the river burst its banks around Saxon's Lode, the floodplain starts conveying a part of the flow that is not accounted for in the corresponding model boundary condition derived from the riverstream gauging station.

In terms of flood extents, results show the porosity model fills in and drains floodplain water faster than the standard model. To better assess this behaviour, we compared both model results to a series of remote sensing derived flood maps. It was shown that, during the falling limb, the observed inundation extent is closer to the one simulated with the porosity model, especially in the areas around Tewkesbury. This faster flooding and receding dynamic in the porosity model is mainly related to its ability to represent small scale topography and drains via porosity. As mentioned in section 1.2.2.1, representing small drains in the standard model requires cells with dimensions smaller than that of the drains. This means that drains should in theory be finely discretised by very small cells (Fig. 1.12) in the SW2D model. These drains are visible in the LiDAR topographic data (Fig. 1.3), but they are not captured by our standard model mesh, because the mesh cells are comparatively large. For example, the size of a cell

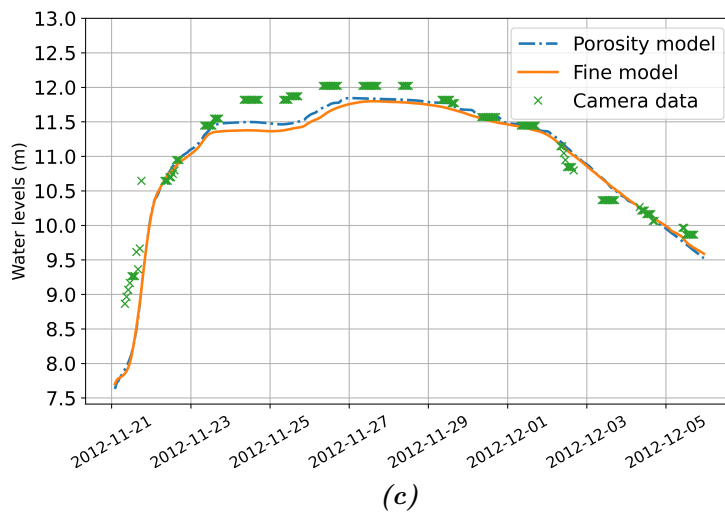
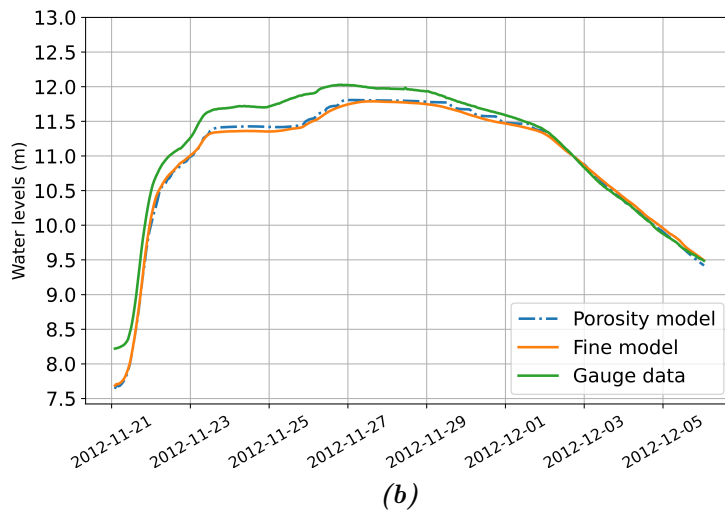
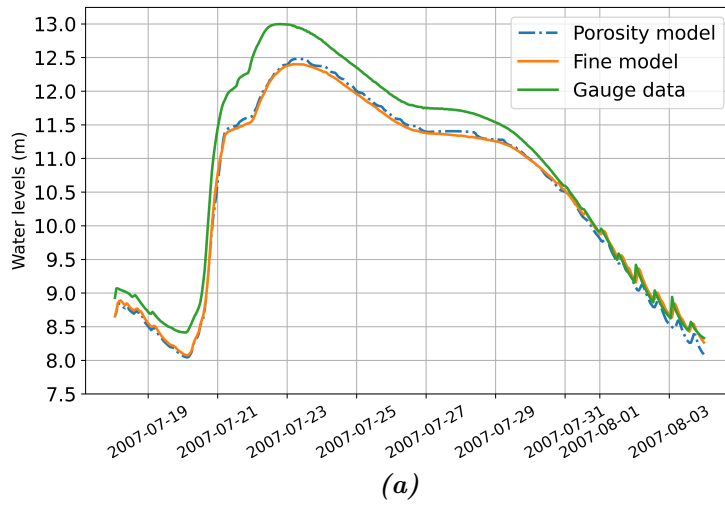


**Figure 1.11:** Water level time series evaluation using data at Mythe Bridge for the 2007 event (a), 2012 event (b) and at Tewkesbury for the 2012 event (c).

capturing a drain would have dimensions smaller than 5 m, which would increase the number of computational cells along the drainage network. The standard mesh designed in this study consists of 29,772 cells, representing approximately 28 times more cells than that in the porosity mesh (1,042 cells). Moreover, the simulation run time in that case would escalate drastically with the decrease of the simulation time step becoming inconvenient for large scale applications. Table 1.3 summarizes the CPU times necessary for the standard and the porosity model simulations, carried out on a computer with an i7-4770 CPU processor and a memory of 16 GB RAM. For an area of 1500km<sup>2</sup> and in both test cases, the CPU time required for the model simulation is 13 min vs. 3.2 days for the standard model for a 17 days flood simulation, and 12 min vs. 2.9 days for a 15 flood day event. The porosity model therefore offers the advantage of a fast model setup, while preserving high resolution data by using coarse grid cells, thus enabling reduced computational efforts. This paves the way for real time applications and long terms simulations over large areas.

All singularities and types of cross-section can be taken into account in the porosity laws as long as they are visible in the DTM. However, the spatial localisation of the singularity inside a coarse grid cell is lost, this is why it is preferable to place the interfaces on the singularities so as not to create artificial links between the cells. Since cross-sections are rarely available along the entire river and only punctual measurements are provided, a riverbed shape approximation must be made, which is facilitated by the use of porosity laws. The interpolation of river bathymetry between observed cross sections certainly has an influence on the model results, but it is the only available information. In this study we compared both models using the same bathymetric data. The linear interpolation of these profiles along the river appeared to be reasonable since no brutal variations of the slopes were observed while examining longitudinal profiles. However, further improvements are expected when having more precise bathymetry data. In this study the topography information is derived from a high resolution LiDar DTM originally at 2m resolution and resampled at 10m. With increasing availability of global DEMs (*e.g.* SRTM 30m at a global scale), the modelling approach can be applied in poorly gauged areas. For the specific case of urban areas, the building location map could be used to improve the DEM, based on widely available databases such as OpenStreetMap. The vegetation remains more complex to be accounted for and for the moment we may consider vegetation effects through an increased friction coefficient, as usually done in hydrodynamic modelling. In the SW2D software (classical or DDP), all parameters such as infiltration rates and friction, can be spatially distributed (*e.g.* based on land use maps).

As discussed in [50], one main limitation of the porosity modelling approach is the definition of a unique water level per computational cell, which is equivalent to considering a horizontal free surface elevation in each cell. Although the consequences of such an assumption are limited when dealing with large-scale and slow floods, they may not be negligible and should be assessed. The porosity-based approach also leads to a loss of spatial information inside coarse grids.

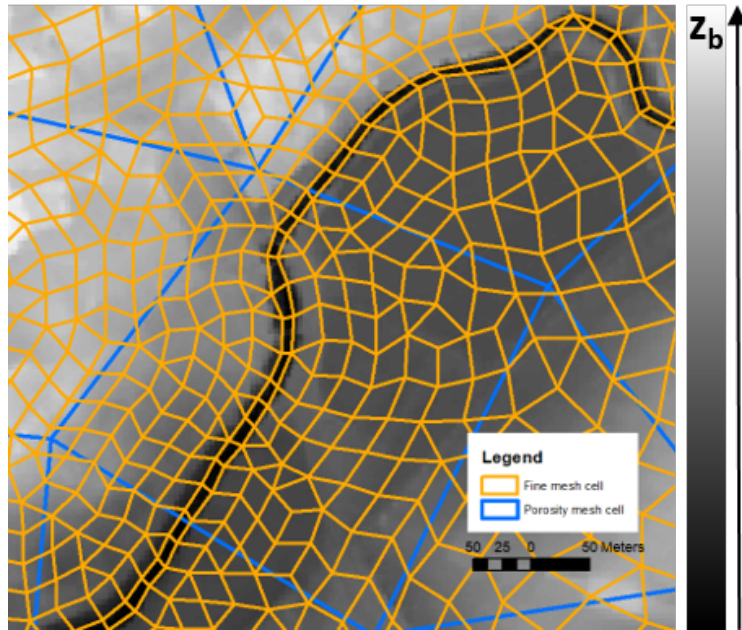


**Figure 1.12:** Drains representation by computational cells in the SW2D (orange) and SW2D-DDP (blue) models.

This can potentially create artificial links between cells unless the edges are carefully placed upon local highest points. However, one should keep in mind that this is also true for other hydrodynamic models, such as classical 2D ones. Moreover as seen before, it is possible to recover spatial information by resampling the results on the DTM as proposed in this paper, therefore preserving the original DTM data at its original resolution.

**Table 1.3:** Simulation run time for the porosity (SW2D-DDP) and standard (SW2D) models, with the run time reduction factor

Flood event	Simulation period	SW2D	SW2D-DDP	Reduction factor
2007	17 days	3.2 days	13 min	354 times
2012	15 days	2.9 days	12 min	348 times

## 1.6. Conclusion

In this paper, we proposed an innovative modelling framework based on porosity to rapidly simulate flood inundations. This framework enables, for the first time, to represent both bathymetry and small-scale floodplain topography using depth-dependant porosity within comparatively large computational cells. Simulating two real test case floods over a 1500 km<sup>2</sup> area around the Severn and Avon confluence, has shown the following:

1. The proposed modelling approach enable to simulate flood extent maps very similar to the one simulated by the standard SW2D model with 90 % agreement.

2. The evaluation based on in situ measurements indicates that the porosity model is exhibiting levels of performance comparable to and even higher than those of a standard model.
3. It is found that the porosity model is able to account for small drains within comparatively very large cells. Representing these small drains in a standard model would require very small cells, therefore leading to a much higher number of cells and a large computational demand.
4. Our experiment shows that the SW2D-DDP model simulations are c.a. 350 times faster than that of the standard model, thereby substantially reducing computational costs.

In perspective, the proposed modelling framework facilitates the retrieval of an effective bathymetry as this is represented via the porosity parameters. This opens up new perspectives for large scale applications over areas where bathymetric data are not available.

# Estimating flood depth from space: an automatic method based on satellite imagery and topography data

*This chapter is adapted from an article submitted to Remote Sensing of Environment*

Ayoub et al., submitted

---

2.1. Introduction . . . . .	37
2.2. Materials and methods . . . . .	40
2.2.1 Flood extent mapping from SAR imagery . . . . .	40
2.2.2 Pre-processing of topographic data . . . . .	41
2.2.3 WaSER: Water Surface Elevation Retrieval algorithm . . . . .	42
2.2.4 Post-processing . . . . .	44
2.2.5 Evaluation approach . . . . .	45
2.3. Study site and available data . . . . .	46
2.4. Results and discussions . . . . .	47
2.4.1 Evaluation of SAR-derived flood extent maps . . . . .	47
2.4.2 Evaluation of the WaSER flood extent maps . . . . .	49
2.4.3 Evaluation of the WaSER water surface elevation maps . . . . .	53
2.4.4 Window size sensitivity analysis . . . . .	56
2.5. Conclusion . . . . .	57

---

## 2.1. Introduction

Floods are among the most common and devastating weather-related natural phenomena and it is predicted that global change will lead to more frequent and severe floods in the future.

Hydrodynamic modelling is recognised as the best option to assess flood hazard and how it may change from now and into the future. However, to reduce the uncertainty associated with their predictions, models need to be calibrated and controlled using independent data sources. With floods becoming more frequent and severe due to global change [24,83,112], there is a crucial need to continuously improve flood management systems. Floods cause damages on many levels, including human, socio-economical and environmental losses. Risk assessment makes sure that resources are allocated optimally in the prevention and emergency phases [3,63]. When mitigation measures are properly identified, the cost of rebuilding areas after a flood event can be significantly reduced. Flood forecasting and monitoring tools are necessary for defining and implementing adequate mitigation measures enabling the reduction of disaster risk [33]. In this context, it is fundamental to have access to accurate and reliable observations of flood extent (FE) and water surface elevation (WSE) in order to calibrate and periodically control numerical modelling-based predictions.

Flood inundation (hydraulic) models numerically solve the Shallow Water Equations (SWE), also called de Saint-Venant equations. They simulate surface water dynamics accurately but are often associated with a high computational cost, especially when applied at a large scale [8,88,118]. Moreover, to be reliable, these models need to be calibrated and periodically controlled, ideally with spatially distributed in situ measurements of streamflows and/or WSE. However, this kind of data is rarely available and the decline of operational gauging stations worldwide has led to an increased scarcity of spatially distributed data [4,111]. In this context, satellite Earth Observation (EO)-derived data are a relevant and complementary source of information [27,59]. Indeed, as the number of satellites and EO missions is increasing rapidly, attractive opportunities await for the effective integration of such information into flood inundation models.

Since the 1970s, many studies have shown that flood mapping from space is feasible with “good accuracy” [87]. Both optical and microwave sensors can be used for inundation mapping, offering different potentials for water detection. Among satellite EO sensors, Synthetic Aperture Radars (SARs) tend to be the first choice for flood mapping applications due to their all-weather and day-and-night image acquisition capability, and their straightforward detection of smooth open water areas [61,123]. Various methods have been proposed in the state-of-the-art to delineate water from SAR data, either using a singular process or a combination of several processes (*e.g.* [73,117]). In these papers, recorded backscatter values are used to classify pixels as flooded and non-flooded. In the literature, classification methods include thresholding, region growing, change detection, active contour models [55,57], graph-based techniques [15,74], fuzzy theory [47,97], supervised machine-learning techniques [92,94] and SAR time series analysis [107]. However, while many efficient and automatic flood mapping algorithms already exist, to the best of our knowledge, there are currently only few studies focusing on the automatic retrieval of WSE maps from SAR images.

Like FE, WSE is a very important piece of information in risk assessment studies, since it provides further information on flood-prone areas and helps estimating socio-economic flood

damages and risk [113]. Currently, WSE can be estimated from space via radar or LiDAR altimetry techniques [14,39]. The main limitation of this approach is the limited Earth coverage, only along hundred kilometre-spaced profiles. The SWOT mission - to be launched in December 2022 and based on radar interferometry [53] - promises to provide a larger coverage allowing up to 65% of water surfaces of the world to be measured. The need for global coverage to be able to monitor floods all around the world has indeed triggered the launching of the Sentinel-1 mission, which provides enhanced revisit frequency and global coverage every few days.

An indirect estimation of WSE is also possible by combining satellite EO-derived FE maps and topographic data [109]. This is usually carried out by intersecting the flood extent shoreline with a Digital Elevation Model (DEM). In this respect, a small number of studies have targeted the conversion of inundation extent into inundation depth, by applying constraining protocols to guarantee the hydraulic coherence of the water depth (WD) estimates [61,77,98]. Other methods have suggested segmenting the floodplain using river-floodplain cross-sections, perpendicularly placed with respect to the river course, in which WSE are assumed to be horizontal [80,108,135]. Apart from these initial studies, several works *e.g.* [18,76,77] focused on improving the accuracy of the estimated WSE. Cohen et al. [21] have recently developed a water-depth assessment algorithm using a flood extent and a DEM, to provide spatially distributed WSE based on an interpolation of flood boundary WSE. In the remote sensing derived inundation map, two types of cells are distinguished: the boundary cells (at flood shorelines) and the domain cells (inside the flooded area). The algorithm is first based on computing a raster of the flooded area, with all cell values equal to “No Data” except for flood boundary cells which receive the value of the underlying DEM. Then, for the domain cells, each cell is assigned with the elevation of its nearest boundary cell, using a focal statistics loop. The iterative loop is conditioned in a way that the value of a cell in the new raster layer will be assigned the elevation value of the smallest neighbourhood size, *i.e.*, the nearest boundary cell. Finally, the water depth is obtained by deducting this final iteration of the focal statistics loop and the DEM. A post-processing step smoothes sharp changes in floodwater depths and assigns an average value for each cell based on its  $3 \times 3$  neighbourhood. Results of this method have shown that the differences in predictions of WSE compared to hydraulic modelling simulations were small ( $< 0.5$  m) for a large part of the inundated area. However, some zones at flood boundaries, urban areas or steep terrain, exhibited errors greater than 5 m. While flood delineation methods are fast and fully automated, the estimation of WSE from SAR images still encounters important limitations: i) information is generally only obtained at the flood extent shorelines, ii) the estimation methods are often not straightforward or automatic, iii) they typically require high-resolution topographic data (*e.g.* Lidar DEM) that are not available globally, iv) some of the methods are based on hydraulic assumptions that cannot always be validated, and v) they require hydraulic expertise for interpretation [61, 78, 126].

In this context, with the increasing availability of global and free EO and DEM datasets, our main objective is to develop an unsupervised and automatic algorithm enabling WD retrieval and FE map refinement using satellite EO-derived FE maps and topography data. To do

this, the proposed algorithm uses a  $FE_{SAR}$  map and a topography map as inputs. For the second input, two types of topographic data are proposed and compared: the DEM, representing the altitude of the terrain, and the Height Above Nearest Drainage (HAND) that normalises terrain elevations with respect to the drainage network [91,130]. An additional objective of this study is to allow for the computation of spatially distributed WSE, while most of the previous state-of-the-art studies estimated WSE at the FE shorelines only. To fulfil these objectives, we propose comparing the three variants of an algorithm, all based on the following generic steps: i) generating synthetic flood maps from topography data (DEM or HAND) via iterative global or local thresholding, ii) comparing these synthetic flood maps with the EO-derived ones to identify optimal threshold(s), and iii) generating a refined FE map, a WSE map and a WD map using the optimised threshold values and the topography data. To evaluate the accuracy of the refined FE maps and the WSE estimates, we use flood maps derived from high-resolution aerial photographs and hydraulic model simulation results. We use a flood event that took place in summer 2007 in the Severn basin (United Kingdom) as our test case.

The remainder of this paper is organised as follows: First, in Section 2.2., we present the three proposed variants of the algorithm. Next, we describe the evaluation approach making use of high-resolution remote sensing-derived data and of hydraulic model results. Then, the study site and available data are described in Section 2.3.. Section 3.4. presents the results of our study and Section 3.5. discusses and concludes its main outcomes.

## 2.2. Materials and methods

This section presents the proposed algorithm, referred to as WaSER (Water Surface Elevation Retrieval). As previously mentioned, WaSER is presented and tested in three variants, namely HAND G. (Global), HAND L. (Local) and DEM L. (Local), all relying on the same rationale, and based on the steps described hereafter.

### 2.2..1 Flood extent mapping from SAR imagery

To derive FE maps from SAR imagery, we adopted the method proposed by [19]. This algorithm classifies flooded and non-flooded pixels into four main steps: i) image histogram parameterisation based on the distribution of backscatter values, ii) thresholding, iii) region growing and iv) change detection. As water often covers a limited fraction of the image, it is very difficult to reliably parameterise the image histogram. To circumvent this limitation, the method includes a fully automated Hierarchical Split Based Approach (HSBA) that identifies, within the entire flood image, tiles of variable size, covered by a substantial amount of water that enable a more robust parameterisation of the image histogram. The advantage of this SAR-based flood mapping technique is that it is automated, unsupervised and easily applicable to large datasets. In the WaSER algorithm, the  $FE_{SAR}$  is used to globally (G.) or locally (L.) optimise the threshold applied to the topographic data, as detailed hereafter.

### 2.2..2 Pre-processing of topographic data

In this study, two types of competing topographic data are used and compared as inputs: i) the DEM and ii) the HAND. If we consider a pixel with  $(x, y)$  coordinates, the  $DEM(x, y)$  map is the digital representation of elevation data. The  $HAND(x, y)$  is a relief descriptor originally used for terrain classification [91, 100], which has been used in previous studies for flood mapping at the regional and continental scales [2]. When deriving a HAND map from a DEM, the height reference to sea level is removed and the topography is normalised with respect to the drainage network. In other words, pixels belonging to this drainage network have a zero HAND value.

From a technical point of view, the required inputs for generating a HAND map are the DEM and the river network rasters. If not available, the drainage network can be extracted from the DEM, following a sequence of four steps [11]: i) creating a hydrologically coherent DEM through depression filling, ii) defining flow paths by directing flow from a pixel to the neighbouring pixels using a d8 approach following the steepest slope, iii) computing a flow accumulation raster using the flow direction raster as a source data, and, iv) fixing a flow accumulation threshold above which the drainage/river channels start. The HAND thus represents the difference in elevation for each pixel and its nearest draining point in the drainage network.

Figure 2.1 shows how the  $HAND(x, y)$  grid is obtained, using a  $DEM(x, y)$  and flow direction rasters. The pixels belonging to the drainage network are represented in blue. For example, if we look at the red-framed pixels in the grids, the upstream cell in the DEM with an elevation of 40 m, will drain into the cell with an elevation of 32 m following the steepest slope direction, and will have a corresponding HAND value of  $40-32=8$  m.

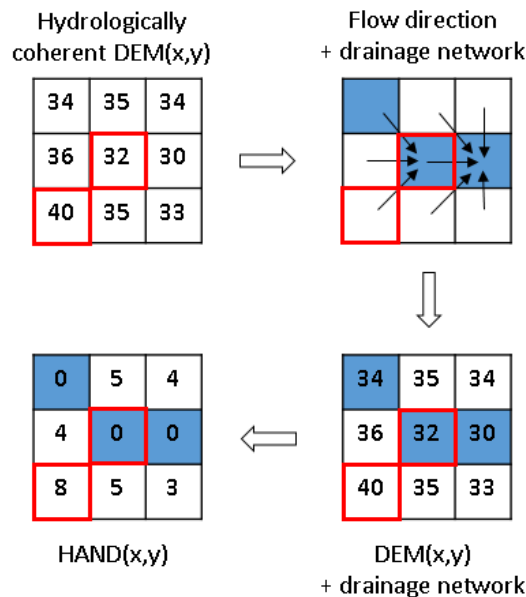
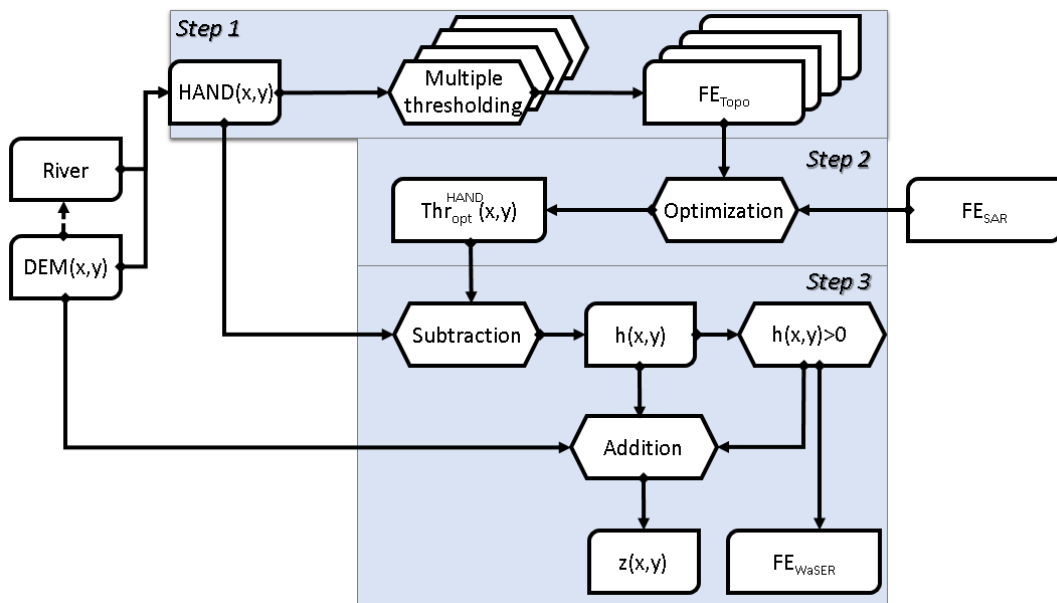


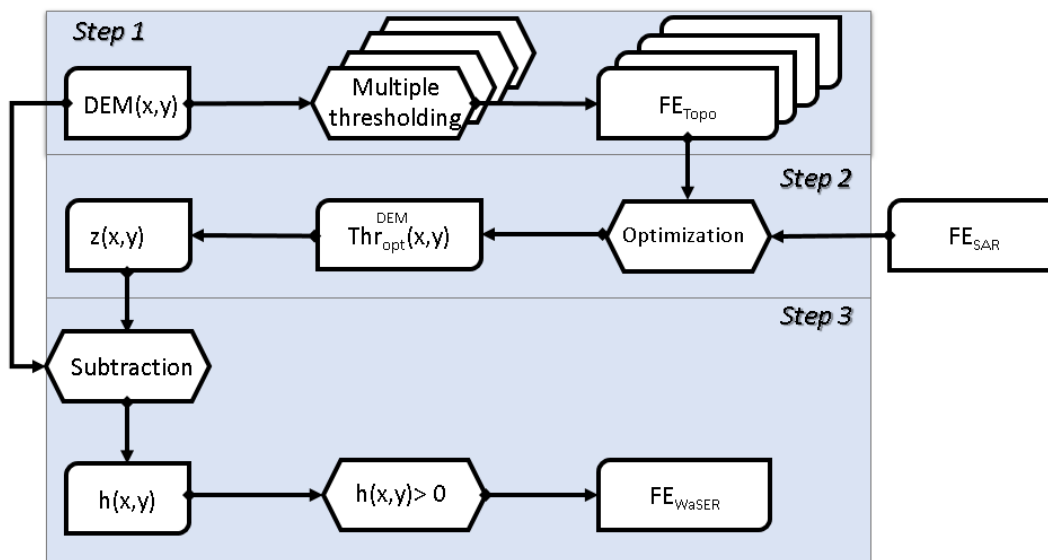
**Figure 2.1:** Computing HAND values using a DEM and a flow direction rasters.

### 2.2..3 WaSER: Water Surface Elevation Retrieval algorithm

The three variants of the WaSER algorithm we propose rely on the following steps: i) applying a thresholding procedure on topographic data (HAND or DEM) iteratively to generate synthetic flood maps, ii) optimising the (global or local) threshold ( $\text{Thr}_{\text{opt}}$ ) by making use of the  $\text{FE}_{\text{SAR}}$  map, and iii) deriving a refined  $\text{FE}_{\text{WaSER}}$  map along with WD and WSE maps with the optimised threshold(s). Figures 2.2a and 2.2b outline the WaSER algorithm if using the  $\text{HAND}(x, y)$  map (i.e. variants HAND G. and HAND L.), and the  $\text{DEM}(x, y)$  map (i.e. variant DEM L.), *resp.*, as thresholded topographic data.



(a)



(b)

**Figure 2.2:** WaSER HAND G. and HAND L. (a), DEM L. (b) algorithm variant flowcharts.

The first step of the WaSER algorithm is the iterative thresholding of the topography data: either  $\text{HAND}(x, y)$  or  $\text{DEM}(x, y)$  (see Figure 2.2). At each iteration, a threshold is applied to the topography data and a synthetic flood map (i.e.  $\text{FE}_{\text{Topo}}$ ) is therefore generated. Depending on the variant of the algorithm that is considered, the threshold is applied globally (on the whole image) or locally. Each pixel with topography values ( $\text{HAND}$  or  $\text{DEM}$  depending on the WaSER variant) lower (*resp.* higher) than the considered threshold value is classified as flooded *resp.* non-flooded) in the synthetic FE map. At each iteration, the threshold value is increased by a constant amount (*e.g.* 10 cm). This iterative process generates a stack of synthetically generated FE maps, each one associated with a specific threshold value.

The second step of WaSER is the threshold optimisation (see Figure 2.2).  $\text{FE}_{\text{Topo}}$  maps obtained at the first step are compared to the  $\text{FE}_{\text{SAR}}$ . The comparison is carried out using the overall accuracy (OA) (Eq. 2.3), over the thresholding area (i.e. globally or locally). In the three variants, the thresholds yielding the best fit between the  $\text{FE}_{\text{SAR}}$  and the  $\text{FE}_{\text{Topo}}$  are selected as optimal thresholds ( $\text{Thr}_{\text{opt}}(x, y)$ ), as explained below. In the HAND G. and HAND L. variants, the optimised threshold(s) refers to the water level above the drainage network and is denoted  $\text{Thr}_{\text{opt}}^{\text{HAND}}(x, y)$  in the following. In the DEM L. variant, the optimised threshold(s) refers directly to the WSE (i.e. with respect to sea level) and is denoted  $\text{Thr}_{\text{opt}}^{\text{DEM}}(x, y)$ . In the HAND G. variant, the optimisation is carried out globally, meaning that the OA is computed over the whole area of interest (AOI) and that the threshold value yielding the best OA is selected as the optimal value. As a consequence,  $\text{Thr}_{\text{opt}}^{\text{HAND}}(x, y)$  is a map with a uniform value in the HAND G. variant. In HAND L. and DEM L., the optimisation is done locally using a  $n \times n$  sliding window. More precisely, the OA is computed iteratively and the threshold value yielding the best OA over this sliding window is selected as the optimal value and associated with the central pixel of the sliding window. As a consequence,  $\text{Thr}_{\text{opt}}^{\text{HAND}}(x, y)$  (*resp.*  $\text{Thr}_{\text{opt}}^{\text{DEM}}(x, y)$ ) is a map with a non uniform value in the HAND L. (*resp.* DEM L.) variant.

The third step of the WaSER algorithm is the generation of a refined FE map, along with the WD and WSE maps. In the HAND G. and HAND L. approaches, WaSER first computes the WD map  $h(x, y)$  as the difference between the  $\text{Thr}_{\text{opt}}^{\text{HAND}}(x, y)$  map and the  $\text{HAND}(x, y)$  map (Eq. 2.1a). From this, a refined  $\text{FE}_{\text{WaSER}}$  is obtained while keeping only positive values which correspond to flooded pixels. Next, the WSE map  $z(x, y)$  is computed by adding the ground elevation  $\text{DEM}(x, y)$  to  $h(x, y)$  (see Figure 2.2a and Eq. (2.1b)).

$$h(x, y) = \text{Thr}_{\text{opt}}^{\text{HAND}}(x, y) - \text{HAND}(x, y) \quad (2.1a)$$

$$z(x, y) = \text{DEM}(x, y) + h(x, y) \quad (2.1b)$$

In the DEM L. variant, the WSE map  $z(x, y)$  is directly obtained when the optimal threshold map,  $\text{Thr}_{\text{opt}}^{\text{DEM}}(x, y)$ , is computed as in Eq. (2.1b). The WD map  $h(x, y)$  is subsequently derived as the difference between  $z(x, y)$  and  $\text{DEM}(x, y)$ . In the refined  $\text{FE}_{\text{WaSER}}$ , flooded pixels have positive water depths (see Figure 2.2b and Eq. (2.2b)).

$$z(x, y) = \text{Thr}_{\text{opt}}^{\text{DEM}}(x, y) \quad (2.2a)$$

$$h(x, y) = z(x, y) - \text{DEM}(x, y) \quad (2.2b)$$

The overall accuracy metric is defined as follows:

$$\text{OA} = \frac{\text{TP} + \text{TN}}{\text{TP} + \text{FP} + \text{FN} + \text{TN}} \quad (2.3)$$

where: TP stands for true positives (i.e. flooded in both maps), FP for false positives (i.e. flooded in the synthetic map but not flooded in the SAR-derived map), FN for false negatives (i.e. not flooded in the synthetic map but flooded in the SAR-derived map) and TN for true negatives (i.e. not flooded in either map). By making use of this metric, a pixel-to-pixel comparison is conducted between the SAR-derived and the synthetic flood maps.

In the HAND G. approach, a unique threshold is applied to the entire image, presupposing a water level that is parallel to that of the drainage network. This assumption relies on a uniform flow hypothesis and is suitable for rivers with smooth and limited variations of river characteristics (*e.g.* slope, shape, roughness). This can also be valid when applied to small areas where, for example, along river cross-sections, wetted area change is neglected. However, these conditions may become unrealistic in some areas. In particular, meanders and confluences introduce water slope discontinuities, thus requiring the HAND G. approach assumptions to be relaxed. In this context, the calibrated threshold should be computed locally rather than globally. Therefore, in the HAND L. approach, we propose the same concept while applying the thresholding in a localised manner, over  $n \times n$  pixels sliding windows. Moreover, as HAND might also induce deviations related to the nearest drainage identification due to deviations or inaccuracies in the DEM, we propose a third variant of WaSER using  $\text{DEM}(x, y)$ , instead of  $\text{HAND}(x, y)$ . In addition, using the altitudes of pixels (DEM) removes the burden of computing HAND from the DEM. Consequently, in this variant (DEM L.), the thresholding is applied to the  $\text{DEM}(x, y)$  map in a localised way. Therefore, this last variant approximates the WSE as a plane surface over a sliding window.

To enable a meaningful comparison and evaluation of the local thresholding methods, we use the same fixed window size for all tests. This size is a parameter that might affect the accuracy of the results. We argue here that the window size should be large enough to include both dry and wet pixels at any point. If it contains only wet pixels, the computed optimal threshold will be equal to the highest elevation in  $\text{DEM}(x, y)$  or the highest  $\text{HAND}(x, y)$  value within the window. This would not reflect the WSE as it could be substantially above the terrain in the considered window. Moreover, the window size should be small enough that the hypothesis of a constant WSE over the sliding window is reasonable. In Section 2.4.4, a sensitivity analysis is conducted to better understand the influence of this parameter, and outcomes are discussed later in the Results section.

#### 2.2..4 Post-processing

In the local variants of WaSER, the threshold is calibrated using a sliding window, which potentially leads to highly variable WSE locally. Therefore, it is essential to post-process the

WSE maps to reduce the noise that can originate from a spatial mismatch between the DEM and the flood extent map. In this study, we propose the use of a moving average in the  $x$  and  $y$  directions. This means that the  $z(x, y)$  value of each pixel is replaced by the mean of all  $z(x, y)$  values over the sliding window. In the HAND G. and HAND L. variants, the post-processing step is done after obtaining the initial WSE map (i.e.  $z(x, y)$ ), as in Eq. (2.1b). Then, the WD map  $h(x, y)$  is deducted by subtracting  $z(x, y)$  and DEM( $x, y$ ), as in Eq. (2.1a). In the DEM L. variant, the post-processing step is done after obtaining the initial WSE map  $z(x, y)$ , as in Eq. (2.2a).

### 2.2..5 Evaluation approach

In this section, we describe how we evaluated the estimated FE and WSE maps. The three WaSER variants are tested using the different combinations of available SAR flood maps (i.e. FE<sub>SAR</sub>) and topographic datasets with different spatial resolutions.

**Flood extent evaluation** The estimated flood maps are evaluated using the following as references: i) a FE map simulated by a hydraulic model (SW2D-DDP) [9] and ii) a FE map extracted from aerial photography. First, a pixel-to-pixel comparison is carried out to determine whether there is agreement or disagreement on whether the area is flooded or not between the two paired maps. The confusion matrix used for the evaluation includes four values, defined as follows: 1) number of pixels correctly estimated as flooded (TP), 2) number of pixels associated with the overestimation of the flooding extent, (FP), 3) number of pixels associated with underestimation, (FN), and 4) number of pixels correctly estimated as non-flooded (TN).

Second, performance metrics are computed to quantify how well the maps fit to the reference. The Overall Accuracy (Eq. 2.3) and Critical Success Index (CSI) (Eq. 2.4, [105]) are used in this respect.

$$\text{CSI} = \frac{\text{TP}}{\text{TP} + \text{FP} + \text{FN}} \quad (2.4)$$

In contrary to OA, CSI does not take true negatives into account. These two scores attain their highest value of 1 at best, indicating a perfect skill.

Moreover, to better understand the spatial distribution of discrepancies between the maps, we derive contingency maps. They represent the agreement and disagreement between the evaluated maps and the reference maps with four different values indicating *resp.* TP, TN, FP and FN. We evaluate the various estimated maps (SAR, HAND G., HAND L., DEM L.) using the flood maps derived from aerial photography and hydraulic modelling as references.

**Water surface elevation evaluation** To compare the WSE<sub>WaSER</sub> map  $z_{i,\text{est}}$  with the reference (hydraulic model) map,  $z_{i,\text{ref}}$ , we compute the Root Mean Square Deviations (RMSD) as follows:

$$\text{RMSD} = \sqrt{\frac{1}{n} \sum_{i=1}^n (z_{i,\text{est}} - z_{i,\text{ref}})^2} \quad (2.5)$$

where  $n$  is the number of pixels over the entire domain. Deviations are computed in a manner that takes into account areas that are flooded either in the estimation or in the reference. When the pixel is flooded in the WaSER map only, the deviation is equal to the water depth computed and vice versa, if the pixel is flooded according to the reference only, the water depth computed by the hydraulic model is considered as the deviation value.

To spatially evaluate the differences, we compute difference maps between the WaSER and the reference WSE maps, where WSE overestimation is reflected by positive values. To further evaluate the distribution of the differences, we make use of boxplots showing the statistics of the deviation distribution in a graphical way: 1) the lower boundary, 2) the first quartile,  $Q1=25$ th percentile, 3) the median,  $Q2=50$ th percentile, 4) the third quartile,  $Q3=75$ th percentile, and 5) the upper boundary. The interquartile range (IQR) goes from the 25th to the 75th percentile, and therefore represents 50% of the data values. The maximum value of the boxplot is defined as  $Q3 + 1.5 \cdot IQR$ , and the minimum value  $Q1 - 1.5 \cdot IQR$ . Outlier points are thus eliminated from the plots for the sake of readability.

## 2.3. Study site and available data

The study site is located around Tewkesbury, United Kingdom, at the confluence of Rivers Severn and Avon. Figure 2.3 illustrates the  $15 \times 10 \text{ km}^2$  study area. This area was chosen because it has often been subject to widespread flooding in recent decades. Moreover, the SW2D-DDP hydraulic model simulations (FE and WSE maps) are available from a previous study [9], which enables us to perform a comprehensive evaluation of the results obtained over this study area.

The flood event of interest occurred in summer 2007. Envisat (150 m spatial resolution) and TerraSar-X (3 m spatial resolution) images were acquired on 23 July and 25 July 2007, *resp.*. Both SAR images were used to extract FE maps using the approach described in section 2.2.1. The high-resolution photograph comes from an airborne campaign that imaged the flood at a very high-resolution (50 cm) on 24 July 2007, close to the flood peak [44]. The FE was obtained through manual photo-interpretation. The derived flood map allowed the FE estimated by our three proposed variants to be evaluated. Moreover, the numerical model-derived maps are used to evaluate each of the estimated maps at the equivalent time step. The SW2D-DDP hydraulic model used discharge time series as upstream boundary conditions (Severn at Saxons Lode and Avon at Bredon), and WSE time series as a downstream boundary condition at Deerhurst. The initial condition was a fixed WSE equal to the downstream condition. A uniform Strickler coefficient  $K_s = 50 \text{ m}^{1/3} \text{ s}^{-1}$  was used for the riverbed and the floodplain. This model is evaluated and presented in more detail in [9].

The topographic datasets are derived from the globally available Shuttle Radar Topography Mission (SRTM) of 30 m spatial resolution and absolute height accuracy of ca. 16 m [130, 134]), the Copernicus DEM (CopDEM) of 10 m spatial resolution and absolute height accuracy of ca. 4 m available for Europe, and the Light Detection and Ranging (LiDAR) of 2m spatial

resolution (re-sampled at 10m) and 0.1 m height accuracy. It is worth mentioning that the SRTM provides topographic data at 0.5 m intervals.

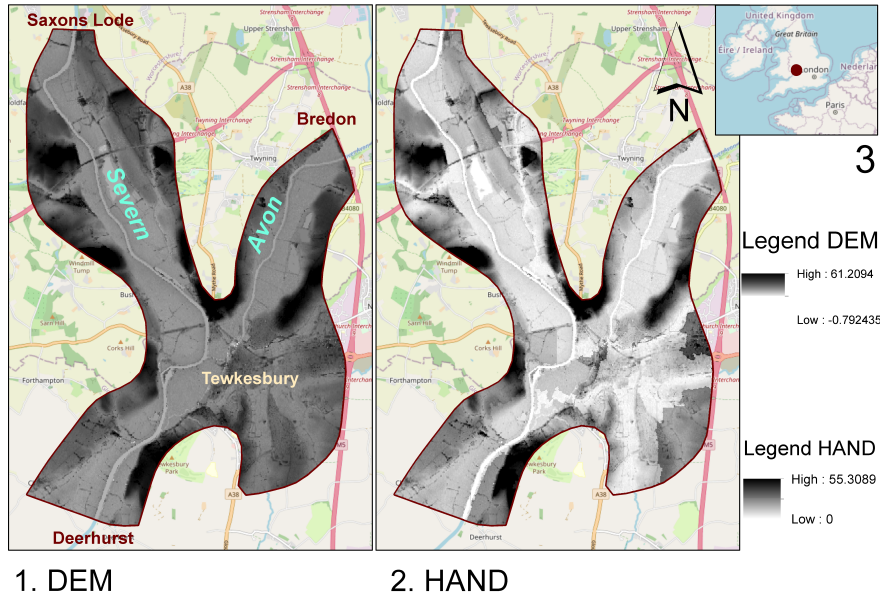


**Figure 2.3:** Study area showing the area of interest (AOI), Rivers Severn and Avon, and the urban area of Tewkesbury. 1) CopDEM topographic data (DEM), 2) HAND map derived from CopDEM, 3) Extent indicator.

Figure 2.3 shows the CopDEM original data (i.e.  $DEM(x, y)$ ) and the HAND data derived from it (i.e.  $HAND(x, y)$ ). It can be seen that in the  $HAND(x, y)$  map, lower values are attributed to the Rivers Severn and Avon floodplains.

## 2.4. Results and discussions

The WaSER maps are derived from 18 different combinations of SAR-derived flood extent, topographic dataset and variant used. The total number of  $FE_{WaSER}$  maps to evaluate is thus 18. As we also investigate the effect of the spatial smoothing (i.e. post-processing), we evaluate a total of 36  $WSE_{WaSER}$  maps. To enable a meaningful comparison between datasets of different spatial resolutions, all output maps are resampled at a 10 m resolution. The results evaluation is carried out in two steps: i)  $FE_{WaSER}$  are assessed using the aerial photography and SW2D-DDP-derived FE maps as references, ii)  $WSE_{WaSER}$  maps are evaluated using the SW2D-DDP-derived WSE maps as references.

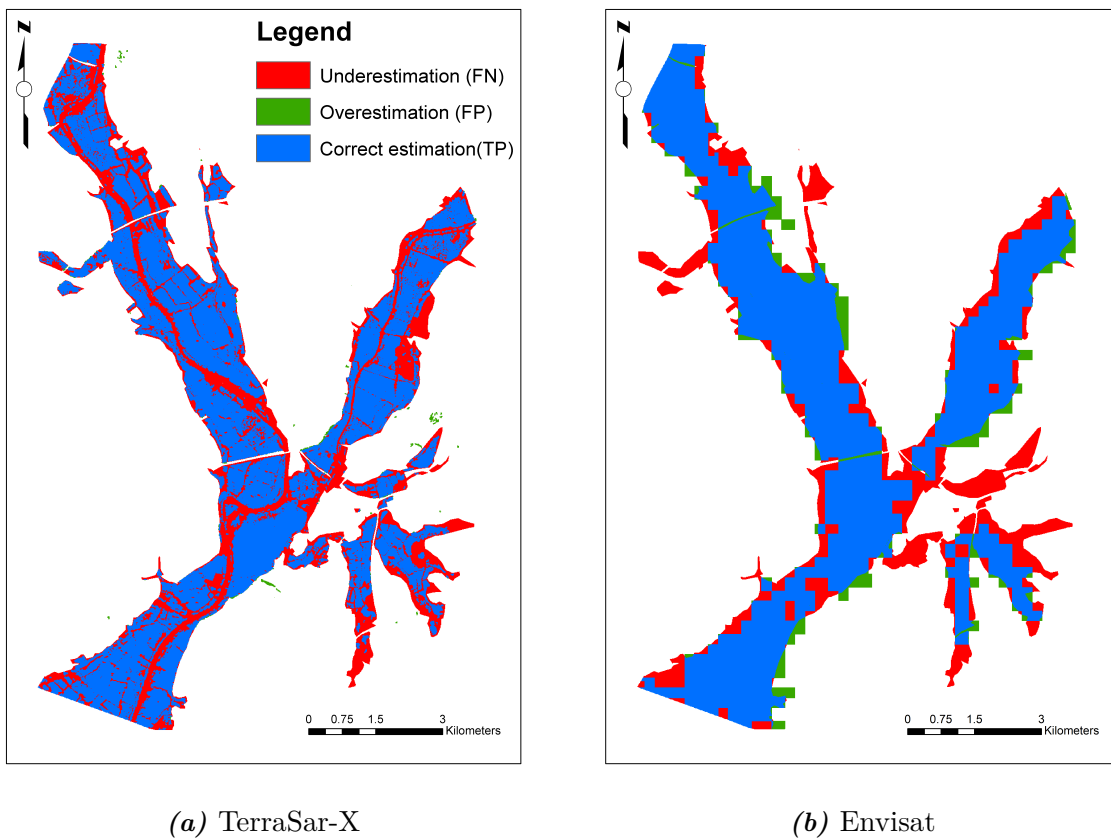
### 2.4.1 Evaluation of SAR-derived flood extent maps

Table 2.1 shows the CSI and OA scores computed by comparing the two  $FE_{SAR}$  (from TerraSAR-X and Envisat) with the aerial photography (P.) and the hydraulic model (M.) flood maps. As expected, both  $FE_{SAR}$  maps are in good agreement with the evaluation maps. Figure 2.4 shows contingency maps obtained by comparing the two  $FE_{SAR}$  maps to the aerial photography-derived flood map, where correct estimation (i.e, TP) appears in blue, underestimation (i.e,

FN) in red and overestimation (i.e, FP) in green. As can be seen in Figure 2.4a, the river stream is not considered as flooded in the  $FE_{SAR}$  map as this is derived using a change detection approach (there is no change of backscatter in the river stream). Adding permanent waters in this TerraSAR-X-derived flood map is possible. However, we preferred to use the raw information in the WaSER algorithm to keep the method independent from ancillary data. In Figure 2.4b, we can clearly see the effect of the spatial resolution with larger pixel-shaped patches in the Envisat-derived flood map (150 m). This figure shows an overall good agreement in the river and floodplains. Moreover, underestimation (FN in red) is predominantly observed close to the flood extent shorelines and in the northern part of Tewkesbury’s urban area.

**Table 2.1:** Goodness of fit metrics between the  $FE_{SAR}$  map (TerraSAR-X (TSX.) and Envisat (Env.)) and i) the aerial photograph (P.), ii) the model simulations (M.)-derived flood maps. OA: Overall Accuracy, CSI: Critical Success Index.

		TSX	Env.
OA	(M.)	0.845	0.821
	(P.)	0.839	0.839
CSI	(M.)	0.684	0.677
	(P.)	0.678	0.698



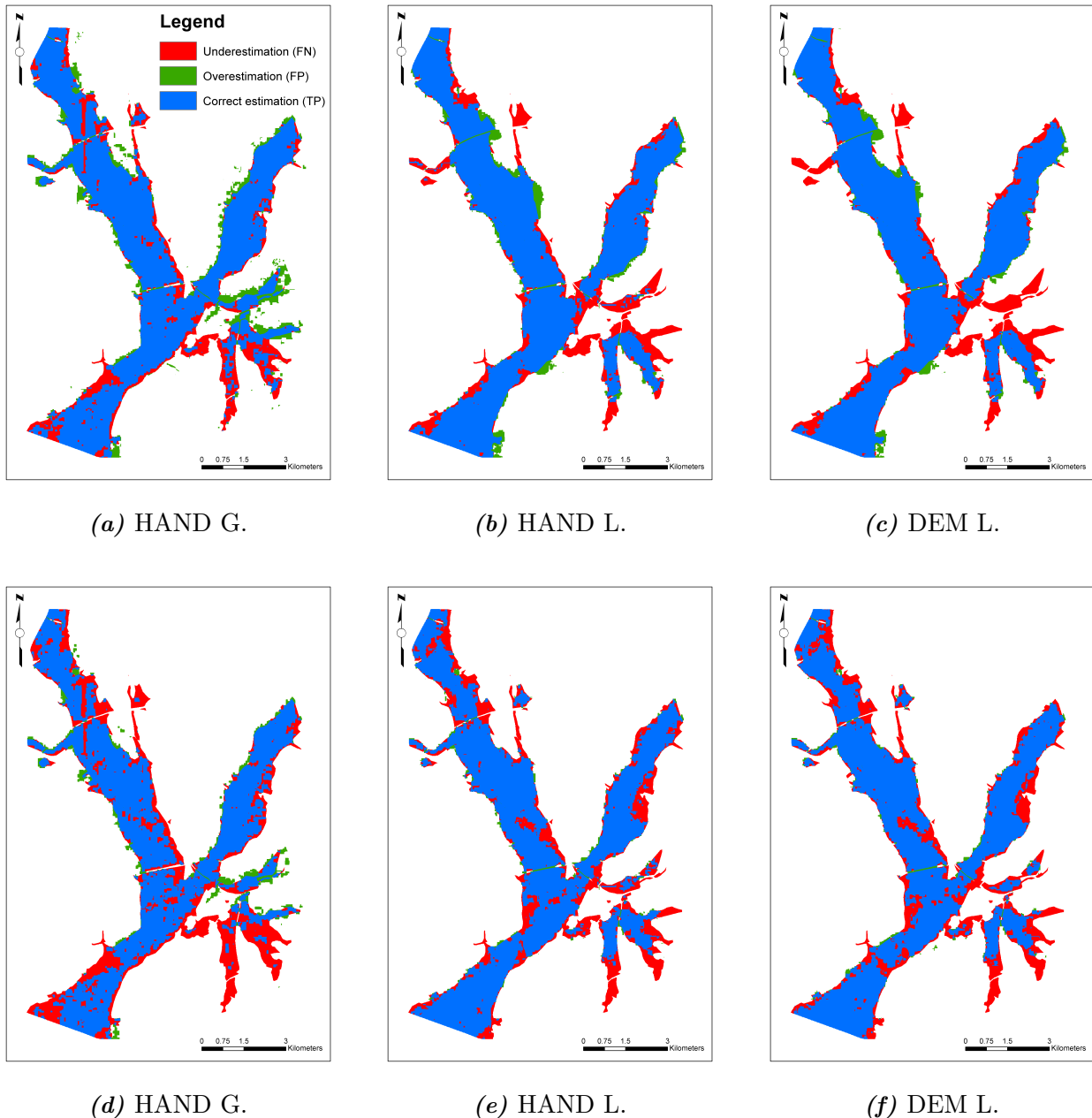
**Figure 2.4:** Contingency maps between the SAR and the aerial photography-derived flood maps: left: TerraSAR-X; right: Envisat.

**Table 2.2:** Performance metrics evaluating the  $FE_{\text{WaSER}}$  and  $WSE_{\text{WaSER}}$  maps using as a reference: i) the aerial photograph (P.), ii) the model results (M.). OA: Overall Accuracy, CSI: Critical Success Index, RMSD: Root Mean Square Deviations, Sm.: Smoothing, No sm.: No smoothing, TSX: TerraSAR-X, Env.: Envisat. Values in pink and orange correspond to the best results in terms of OA(P.) and RMSD, respectively.

			SRTM		CopDEM		LiDAR	
			TSX	Env.	TSX	Env.	TSX	Env.
HAND G.	OA	M.	0.827	0.845	0.770	0.808	0.815	0.762
		P.	0.821	0.852	0.776	0.814	0.805	0.781
	CSI	M.	0.665	0.725	0.562	0.676	0.635	0.554
		P.	0.658	0.729	0.575	0.676	0.622	0.570
	RMSD	No sm.	1.19	1.18	1.67	1.85	1.59	1.78
Sm.		0.93	0.90	1.20	1.5	1.09	1.18	
HAND L.	OA	M.	0.866	0.853	0.884	0.867	0.930	0.882
		P.	0.860	0.870	0.879	0.883	0.906	0.893
	CSI	M.	0.732	0.733	0.769	0.753	0.858	0.785
		P.	0.724	0.753	0.762	0.773	0.816	0.797
	RMSD	No sm.	2.59	3.73	1.55	2.64	1.72	2.39
Sm.		1.96	3.01	0.69	1.46	0.96	1.45	
DEM L.	OA	M.	0.865	0.853	0.899	0.880	0.945	0.906
		P.	0.860	0.871	0.890	0.900	0.918	0.917
	CSI	M.	0.730	0.731	0.795	0.776	0.888	0.823
		P.	0.723	0.753	0.781	0.805	0.838	0.838
	RMSD	No sm.	1.71	2.42	0.73	1.49	0.56	1.21
Sm.		1.35	1.97	0.69	0.83	0.52	0.81	

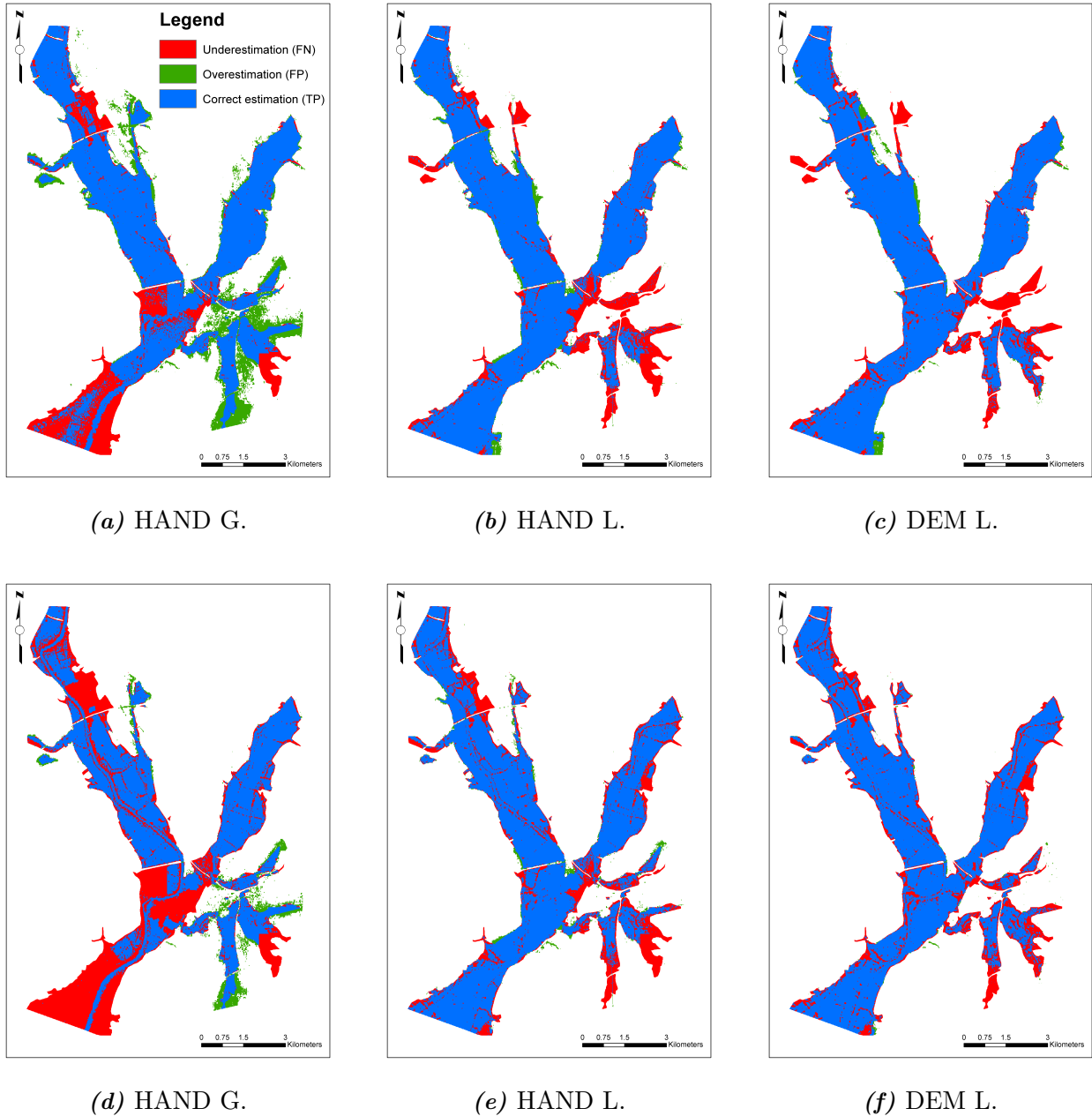
### 2.4..2 Evaluation of the WaSER flood extent maps

Table 2.2 summarises the  $FE_{\text{WaSER}}$  evaluation scores (OA and CSI) computed using the aerial photography (P.) and the hydraulic modelling-derived (M.) FE as references, quantifying the performance of each scenario. Figures 2.5, 2.6 and 2.7 show a series of contingency maps computed between the WaSER and the aerial photography-derived FE. In these figures,  $FE_{\text{WaSER}}$  uses respectively the SRTM, the CopDEM and the LiDAR individually with the SAR-derived data (Envisat in the first row and TerraSAR-X in the second row). It can be seen that the  $FE_{\text{WaSER}}$  is generally able to correctly capture flooded areas. The comparison between Tables 2.1 and 3.1 clearly shows that the  $FE_{\text{WaSER}}$  outperforms the  $FE_{\text{SAR}}$  when generated using the HAND L. and the DEM L. approaches, reaching OA of 86% and up to 91%. The DEM L. variant outperforms the HAND L. variant when using high-resolution datasets (i.e. CopDEM and LiDAR). Moreover, Table 3.1 shows that the HAND G. variant exhibits the best results when using the medium-resolution topographic (SRTM) and SAR (Envisat) datasets. We examine maps reflecting these scores in Figure 2.5a and 2.5d, where a correct estimation of flood extent is predominant (TP in blue). In these figures, the underestimation reflected by red patches is due to higher HAND values in these areas in comparison to those of the surrounding areas, appearing in blue (TP). In fact, optimising the HAND threshold  $\text{Thr}_{\text{opt}}^{\text{HAND}}$  globally when



**Figure 2.5:** Contingency maps between the WaSER and the aerial photography-derived flood maps: (a,d) HAND G., (b,e) HAND L. and (c,f) DEM L. variants, 1st row: SRTM/Envisat; 2nd row: SRTM/TerraSAR-X.

contiguous flooded pixels have markedly different HAND values results in such location-specific underestimations. It makes it impossible for WaSER to retrieve a unique  $\text{Thr}_{\text{opt}}^{\text{HAND}}$  value producing a  $\text{FE}_{\text{WaSER}}$  100% similar to the  $\text{FE}_{\text{SAR}}$  one. When the HAND value of a pixel is above the calibrated threshold it is classified as non inundated. This greatly depends on whether the area is considered as flooded or not, according to the  $\text{FE}_{\text{SAR}}$  map. If it is seen as non flooded in the observation, even if the corresponding HAND values of the area are high, this wouldn't cause any problem to correctly estimate a non flooded area. However, if the area is flooded according to the observation, and the HAND map presents markedly different values for con-



**Figure 2.6:** Contingency maps between the WaSER and the aerial photography-derived flood maps: (a,d) HAND G., (b,e) HAND L. and (c,f) DEM L. variants, 1st row: CopDEM/Envisat; 2nd row: CopDEM/TerraSAR-X.

tiguous pixels, this could lead to a substantial underestimation at a local level. And this is directly related to the resolution of the DEM used to compute the HAND map. It seems that using a coarse resolution DEM to derive a HAND data, allows adequately taking into account the general flow directions. Conversely, this global approach (i.e, HAND G.) is not optimal when using higher-accuracy datasets such as CopDEM and the LiDAR DEM, as it appears in large underestimated areas in Figure 2.6a, 2.6d, 2.7a and 2.7d. For instance in Figures 2.6a and 2.6d, this underestimation is located in a large area of the floodplain in the downstream part. This can also be seen at the eastern upstream part of the Severn floodplain in Figures 2.7a

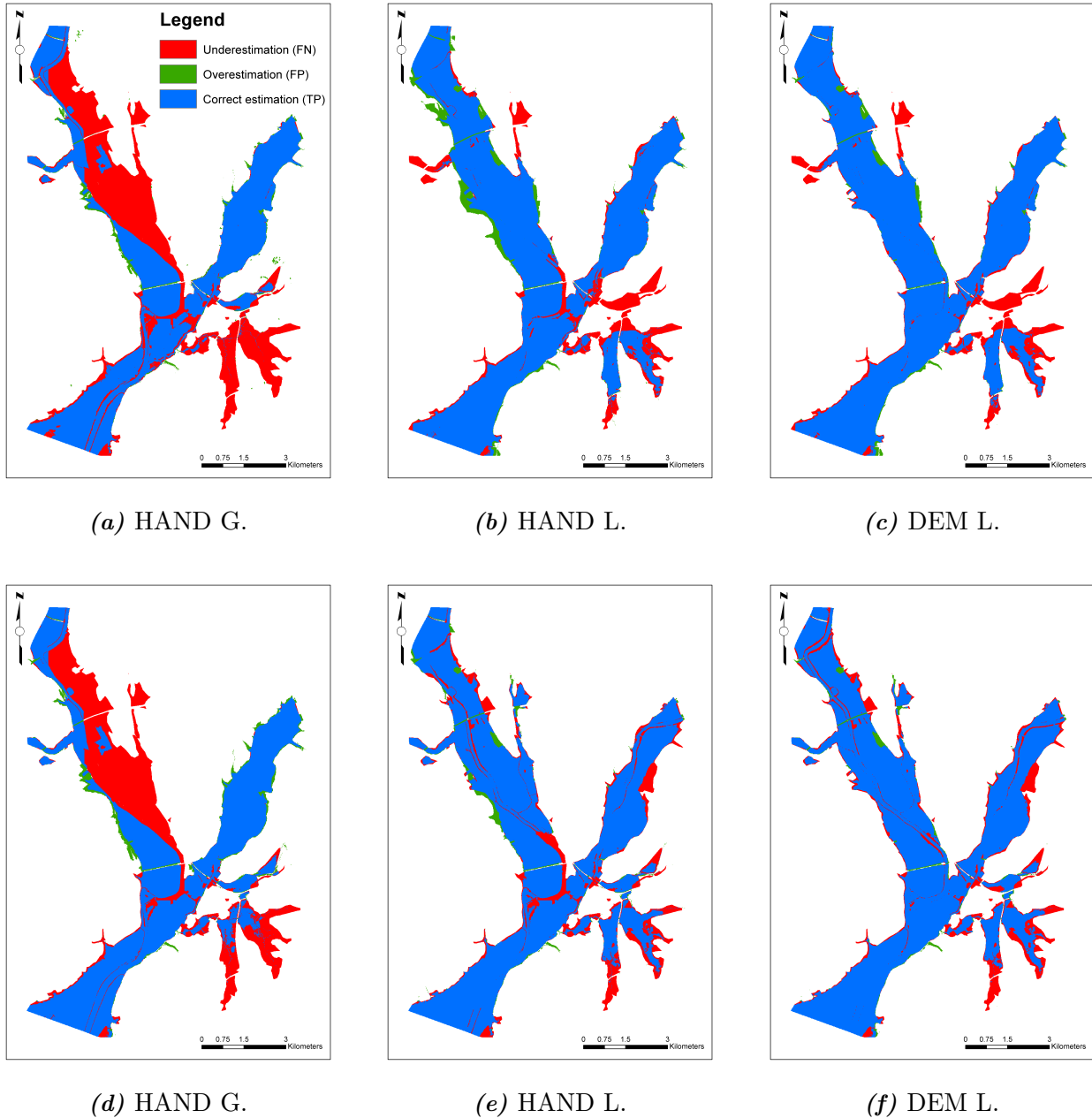


**Figure 2.7:** Contingency maps between the WAsER and the aerial photography-derived flood maps: (a) HAND G., (b) HAND L. and (c) DEM L. variants, 1st row: LiDAR/Envisat; 2nd row: LiDAR/TerraSAR-X.

and 2.7d. These areas exhibit, as previously explained, rather high HAND values which are very quite different of the surrounding areas HAND values.

With the advantage of reducing underestimations by the  $FE_{SAR}$ , by filling the gaps by the HAND G., comes a risk of overestimation (FP in green). A mix of under and over-estimation is due to the use of a single threshold over the entire domain resulting in the best “global” compromise. This is particularly visible in Figures 2.5a, 2.5d, 2.6a and 2.6d, where flood extent is underestimated in the southern part of Tewkesbury, and overestimated in its northern part.

When optimising the HAND (resp. DEM) threshold value locally (HAND L. or DEM L.), we observe a significant improvement when comparing the resulting flood maps (table 3.1 and Figures 2.5, 2.6 and 2.7) to the maps obtained with the SAR only and HAND G. approaches, respectively. The DEM L. variant is the best performing of all variants in terms of flood extent mapping. It is worth mentioning that the underestimation found in the northern region of Tewkesbury in Figures 2.5b, 2.5c, 2.6b, 2.6c, 2.7b and 2.7c, is most likely due to the Envisat  $FE_{SAR}$  underestimating flood extent in this area (see Figure 2.4b). This is also the case at the boundaries of the urban area of Tewkesbury that is already underdetected by SAR (FN in red) in Figure 2.4b and 2.4a. Although the same input HAND map is used for generating the results showed in Figure 2.6d and 2.6e using the CopDEM and 2.7d and 2.7e using the LiDAR, the underestimation seen in red patches when using the HAND G. variant is reduced when using the HAND L. variant as the calibrated threshold is adapted locally, to better reflect the water classification in the  $FE_{SAR}$ . This step enables WaSER to improve the correct estimation of inundated areas, as we overcome the drawback of the best “global” compromise effect when we apply the local approaches.

Overall, the WaSER algorithm in its three variants provides better predictions in rural areas than urban ones.

### 2.4..3 Evaluation of the WaSER water surface elevation maps

Table 3.1 shows the  $WSE_{WaSER}$  map evaluation (before and after post-processing) with respect to the hydraulic model results. Figure 2.8 shows boxplots of the deviations between the WaSER (before and after post-processing) and the hydraulic model-derived WSE maps.

First, in Figures 2.8a and 2.8b, we observe that the distribution of deviations of SRTM-derived WSE varies between -1 and 1 m for the HAND G. variant and presents the smallest spreads, compared to other scenario derived data. The distribution becomes positively skewed when using local approaches (i.e. HAND L. and DEM L.). This reflects an overestimation with respect to the model outputs. Although means (represented by diamonds) are skewed, medians (represented by white horizontal segments) are mostly located between 0 and 1 m. This means that the overestimation by the local variants, is driven by  $WSE_{WaSER}$  that are particularly high at some specific location level. Examining the effect of post-processing WSE, we also observe that minimum and maximum deviations are reduced after smoothing, especially when using local variants. Overall, when the WaSER uses the medium-resolution dataset (i.e. SRTM), the HAND G. approach exhibits the lowest deviations and means which are close to zero.

In Figures 2.8c and 2.8d showing results obtained with CopDEM, we can see at a first glance that the DEM L. approach shows the best results overall. Indeed, with Envisat (Figure 2.8c), the mean values of the WSE deviations are closer to zero, but the boxplots are larger than in Figure 2.8d. Moreover, medians are mostly between 0 and -1, reflecting a general underestimation of the HAND G.- and DEM-derived WSE particularly when using the TerraSAR-X flood map.

Figures 2.8e and 2.8f, show results obtained with the LiDAR DEM. Here, the smallest deviations are yielded by the Dem L. variant. Results are pretty similar to those derived with the CopDEM, except with more underestimation of WaSER-derived WSE when using the LiDAR and the Envisat data.

Overall, we notice for the three graphs that the spreads are smaller when using the higher resolution image (i.e. TerraSar-X). Figure 2.9 shows boxplots of deviation between the SRTM (resp. the CopDEM) and the LiDAR DEMs. It can be seen that the CopDEM exhibits better agreement with the LiDAR, with a mean of 0.2 m and a standard deviation of ca. 2 m. The SRTM shows a mean of 1.3 m and a higher standard deviation of 3.5 m. RMSDs and large spreads obtained when using the SRTM and the CopDEM datasets are very likely correlated to the higher uncertainties of SRTM and CopDEM compared to the LiDAR DEM. Moreover, one can notice in Table 3.1 and Figure 2.8 that RMSDs significantly improve as a result of the smoothing, especially when using the local approaches.

To further investigate the spatial distribution of WSE deviation, we next propose to examine difference maps. Figure 2.10 shows a set of WSE deviation maps computed as the difference between the  $WSE_{\text{WaSER}}$  and their synchronous hydraulic model outputs. The WaSER maps used for this comparison are the: SRTM/Envisat (first row in Figure 2.10) and the LiDAR/TerraSAR-X (second row in Figure 2.10) using the 1) HAND G., 2) HAND L. and 3) DEM L. variants. The maps are displayed with deviations ranging from -2 m (i.e, underestimation in red) to 2 m (i.e, overestimation in green). In Figure 2.10a (i.e, using the SRTM/Envisat for WaSER), one can notice a general homogeneous distribution of the deviations overall. A further observation shows a global underestimation in the Severn floodplain. Underestimated WSE are especially found at the downstream part of the Severn floodplain, and in the southern part of Tewkesbury. Moreover, overestimation is observed in the northern part of the urban zone, globally at the River Avon and at an affluent coming from the upstream western part of the Severn. This under and over-estimation mix using the HAND G. variant, is consistent with what was observed in the contingency maps (e.g: Figure 2.5a). When using local approaches, it is clear that overestimation is predominant (Figures 2.10b and 2.10c) while underestimation is more localised. We also observe some important local deviations, like in the east downstream part of the River Severn. This result is in agreement with what we observed in Figure 2.8d. In the second set of difference maps computed using LiDAR/TerraSAR-X results, a global overestimation is observed in the Avon and in some parts of the upstream the River Severn when using the HAND G. variant (Figure 2.10d). This clearly reveals the HAND presents discontinuities due to contrasted pixel values, when it is generated using high-resolution datasets. While the overestimation is accentuated in the upstream part of the Severn and River Avon when testing the HAND G. variant, as seen in Figure 2.10d, it becomes reduced while using the HAND L. variant (Figure 2.10e), as the the capability of adaptation increases with this optimisation method. Finally, the DEM L. outperforms the other variants and shows the most homogeneous distributed deviations (around zero) in Figure 2.10f.

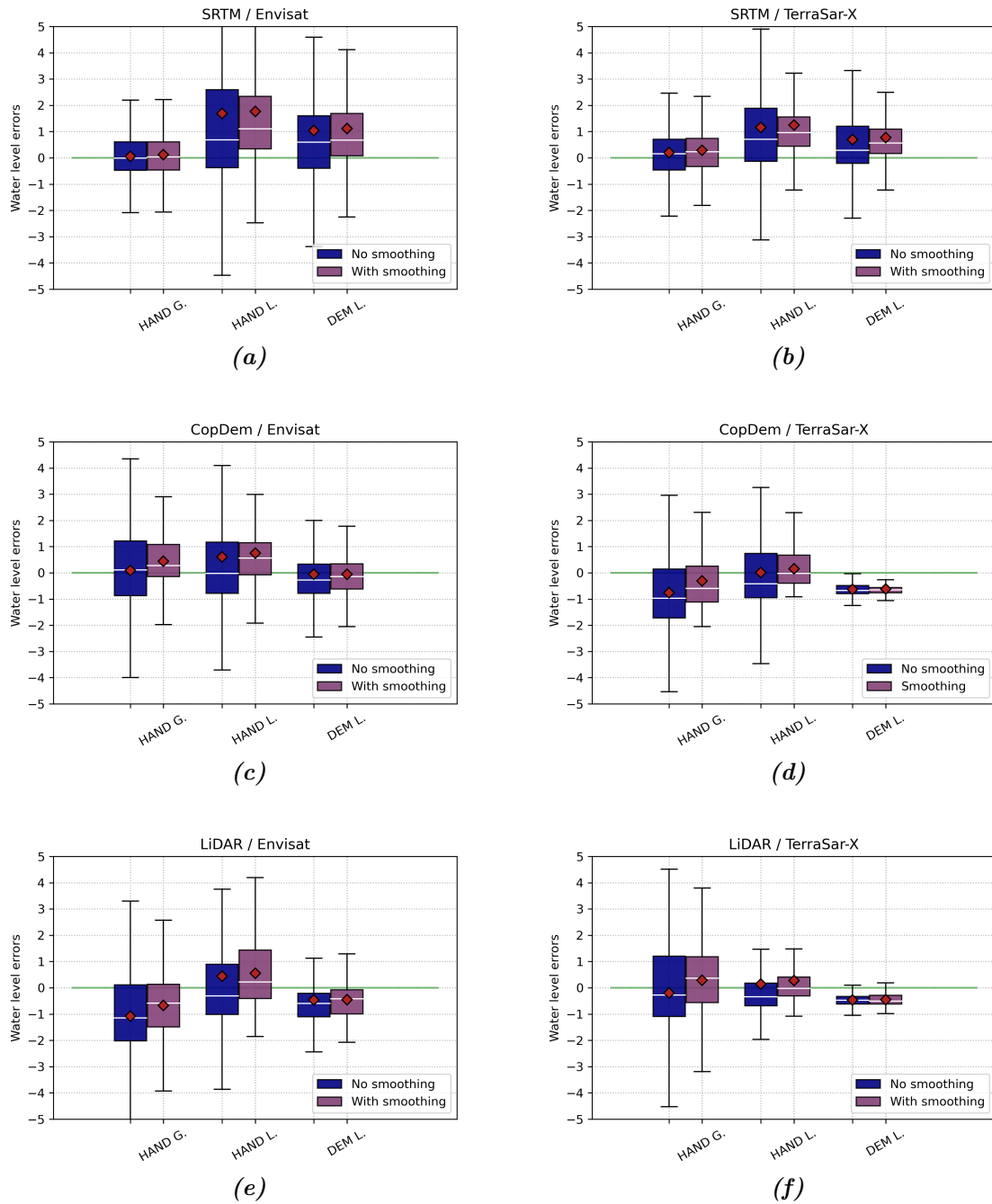


**Figure 2.8:** Boxplots of WSE deviations of the WaSER with respect to the hydraulic model outputs (a-f). White horizontal segments and red diamonds represent the median and mean, respectively.

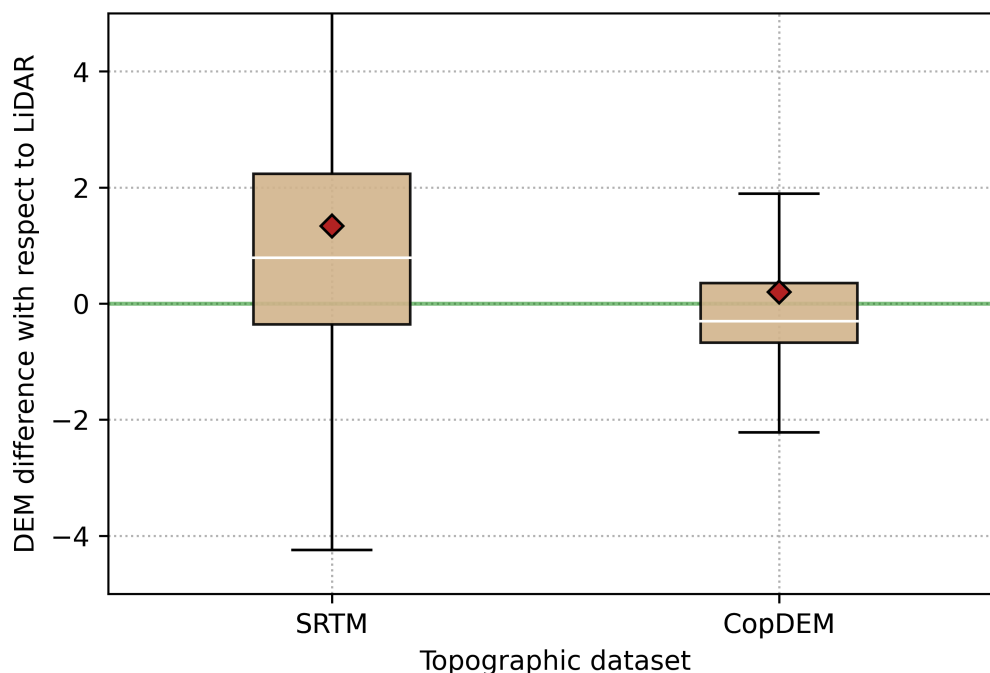


**Figure 2.9:** boxplot of the SRTM/CopDEM deviations with respect to the LiDAR (g). White horizontal segments and red diamonds represent the median and mean, respectively.

#### 2.4.4 Window size sensitivity analysis

The window size determined a priori in this study is equal to  $locws=2010$  meters, therefore representing 10 pixels with a pixel size of 10 m. The choice was made based on the width of the downstream Severn floodplain and it was constrained to respect two conditions: i) the window size has to be sufficiently small to ensure the hypothesis of a rather constant water level over the entire window, and ii) the window size has to be large enough to include inundated and non-inundated pixel (so that the OA include all types of errors and agreement over the window). To better understand the effect of the local window size in the proposed method, a twofold sensitivity analysis was conducted to assess accuracy in terms of FE and WSE estimation in the DEM L. variant. Figure 2.11 shows respectively the CSI and OA performance metrics and the RMSD variation with respect to the local window size (i.e, Locws) variation. As we can see, the optimum local window size is found at  $locws=250$  pixels. As the window size increases, the scores are stabilised. The RMSD reaches its minimum at  $locws=250$ .

We believe that further investigation should be conducted to verify and refine rules defining the optimal window size over various test sites. If the sliding window size is either too big to capture any detail, or too small to capture dry and wet pixels, this can generate errors. For example, in the event all pixels in the window are flooded, the optimised threshold would be equal to the maximum HAND or the DEM pixel values over the window.

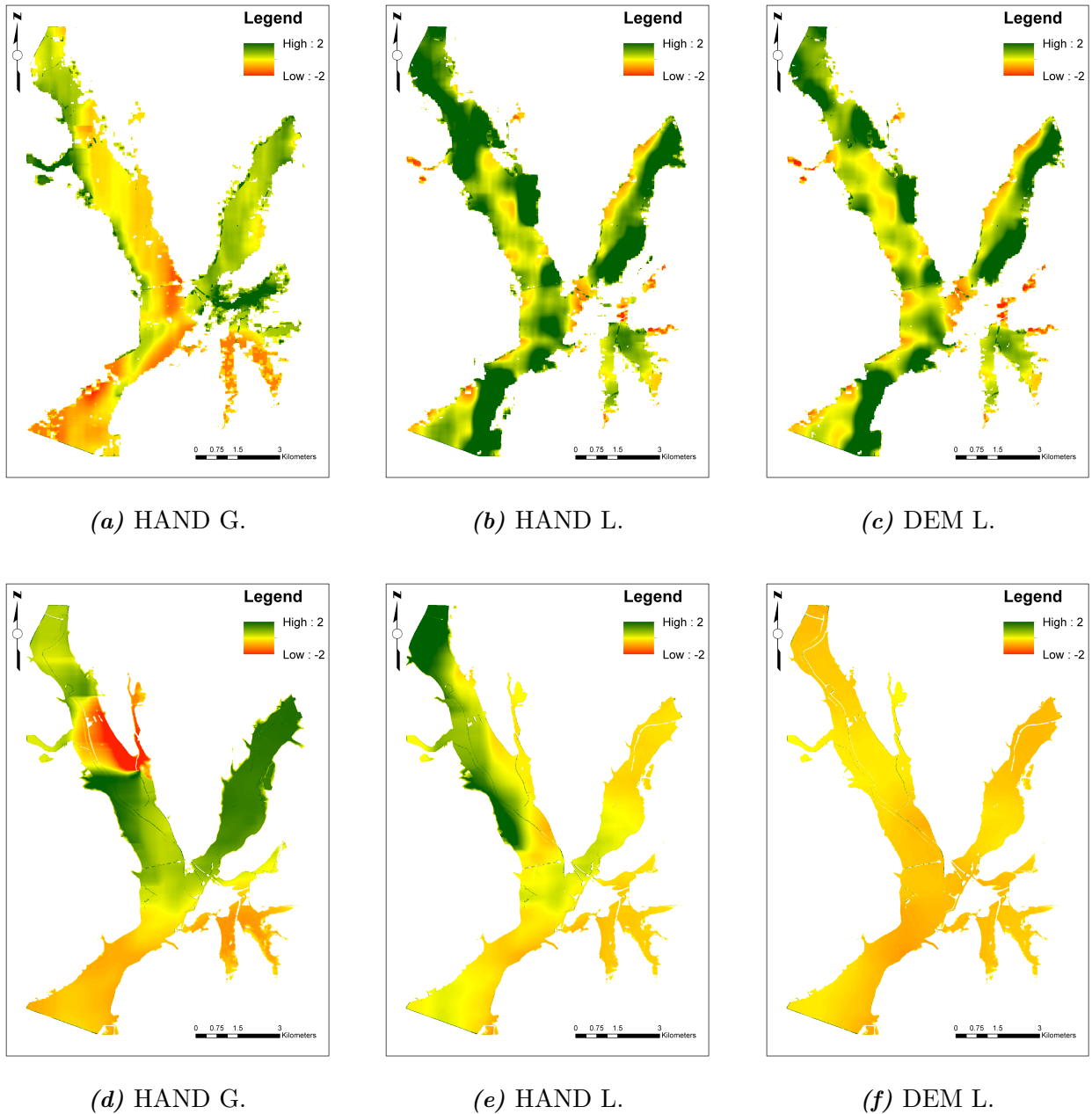


**Figure 2.10:** WSE deviation maps between the WaSER (after post-processing) and the hydraulic model WSE maps. From left to right, 1st row: Srtm/Envisat HAND G., HAND L., DEM L., 2nd row: LiDAR/TerraSAR-X HAND G., HAND L., DEM L.

## 2.5. Conclusion

In this paper, we proposed the WaSER algorithm, allowing for the automatic retrieval of refined flood extent and distributed water surface elevation maps using satellite EO-derived data and topographic data. Three different variants of the algorithm were tested: HAND G., HAND L. and DEM L., based on the same concept and rationale but making use of different input topographic data requiring different intermediate steps.

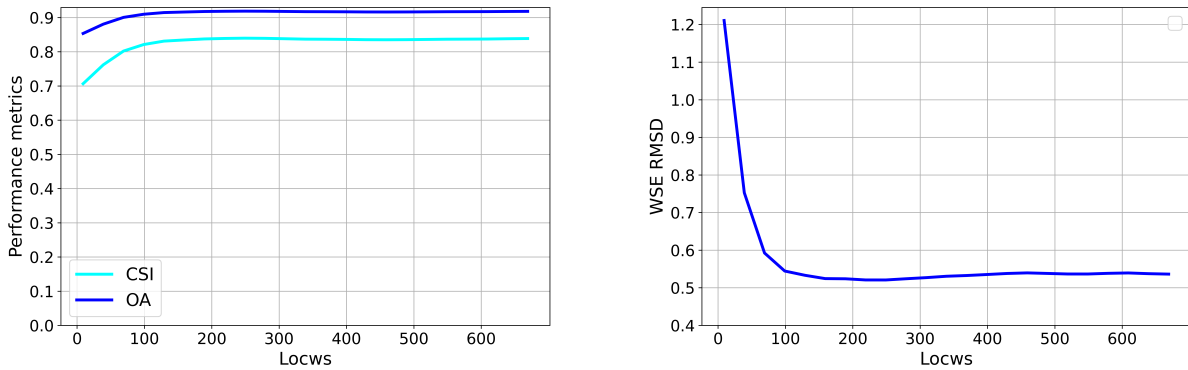


**Figure 2.11:** CSI, OA and RMSD scores using the DEM L. variant with LiDAR/TSX.

The WaSER flood extent maps were in very good agreement with the evaluation maps derived from an aerial photograph and the shallow water model results, especially when using the HAND L. and the DEM L. approaches. The obtained results outperformed the SAR-derived flood extent maps, reaching an overall accuracy in the range of 86-91%. The proposed method generally provides better results using its local variants, thus helping to improve the efficiency of water detection with respect to the sole use of the SAR flood mapping technique. The WaSER water surface elevation maps show the best agreement with the model results when using the DEM L. approach with high-resolution topographic datasets and SAR images, i.e. TerraSAR-X. However, the HAND G. approach yields better results with medium-resolution datasets such as the SRTM (30m resolution) and the Envisat image. Indeed, the level of topographic information detail should be compatible with the resolution of the SAR image in order to prevent the production of artifacts. The best average RMSDs are found using the HAND G. with medium-resolution datasets (i.e, SRTM/Envisat) with a medium-resolution SAR image (i.e, Envisat):  $\text{RMSD} = 0.90$  m; DEM L. using high-resolution datasets (i.e, CopDEM and LiDAR) with high-resolution SAR image (i.e, TerraSAR-X):  $\text{RMSD} = 0.69$  m and  $\text{RMSD} = 0.52$  m, respectively. This is due to the fact that high-resolution datasets contain sufficiently accurate information in the form of a DEM. With the availability of a high-resolution image, the level of information detail in these inputs is compatible and leads to accurate results. While previous works in the literature such as [21], have reached an accuracy of the order 0.38 m for interpolated WSE maps, our proposed algorithm demonstrated slightly less accurate results but in the same numerical range, while proposing an innovative approach to produce distributed WSE maps. This study also showed that RMSD may be further reduced, depending on the topographic dataset and the size of the local window used. In perspective, the proposed method should be further tested on other application sites.

Although the proposed WaSER algorithm is not meant to replace hydraulic models that embrace both the time and space dimensions of the flood dynamic, it constitutes a relevant tool for rapidly estimating large-scale flood depth and extent maps. This can complement in-situ data, and hold promises for ungauged areas. Moreover, with topographic datasets (*e.g.*

CopDEM, SRTM) and high-resolution satellite images (*e.g.* Sentinel-1) being globally and freely available, this method can be easily implemented anywhere across the globe.

# Assimilation of probabilistic flood maps into large scale hydraulic models using a tempered particle filter

---

3.1. Introduction . . . . .	60
3.2. Method . . . . .	62
3.2.1 Probabilistic flood mapping . . . . .	62
3.2.2 The shallow water modelling framework . . . . .	63
3.2.3 The data assimilation framework . . . . .	64
3.3. Study site, available data and experimental design . . . . .	66
3.3.1 Study site and available data . . . . .	66
3.3.2 Experimental design . . . . .	67
3.4. Results . . . . .	70
3.5. Discussion and conclusion . . . . .	74

---

## 3.1. Introduction

As climate change worsens, intensified natural events are expected to happen in the future [112]. Among these events, floods can be the most destructive and can cause significant damages on many levels. According to new data from World Resources Institute’s Aqueduct Floods Tool [133], by 2030 the number of people impacted by floods will double worldwide, from 65 million to 132 million, which could lead to an increase of urban property damage from 157 billion US\$ to 535 billion US\$<sup>1</sup>. This strengthens the need for improving cost-effective flood forecasting models in order to obtain accurate dynamic simulations for flood risk assessment. However, current models are affected with high uncertainties and need to be constrained with independent data that must be acquired from *in situ* measurements or remote sensing derived observations [48,60]. If the network of hydrometric stations was well developed, flow rate and/or

<sup>1</sup><https://www.wri.org/research/aqueduct-floods-methodology>

stage time series would be provided at a relatively sufficient spatial and temporal coverages, and used as inputs for flood models. However, in many areas around the world, stream gauges are sparsely distributed and can be lacking in ungauged basins [86]. To compensate the lack of *in situ* data, we propose to exploit earth observation (EO) and particularly make use of Synthetic Aperture Radar (SAR) imagery due to its ability to provide frequent updates of flooded areas at a large scale, regardless of atmospheric conditions. Moreover, the specular reflection of the emitted backscatter on open water bodies allows a relatively straightforward detection of water on the SAR image. Thus, these images hold an added value and a potential to improve the predictive accuracy of flood forecasting models through data assimilation (DA).

Widely used in the fields of hydrology, hydraulics and geosciences [16,25,99,102,119], DA is a mathematical discipline that aims to optimally combine uncertain model predictions and uncertain observations. This relies on the estimation of optimal model states and/or parameters and allows thereby for the reduction of model uncertainties. DA can be carried out sequentially, for example in near-real time, by updating model states and/or parameters using observations as they become available, or in a reanalysis by assimilating all observations at once, i.e, retrospectively. Among the various available DA methods, the ensemble Kalman filter (EnKF) and the particle filter (PF) are found to be the most popular in hydrological applications [35, 124, 127]. Among other DA methods based on variational assimilation, the most common is the 4DVar, which comes from the optimal theory control of partial differential equations [69]. This approach allows the retrieval of the initial and boundary conditions as well as the optimal parameters, but often requires a complex implementation of the adjoint code to compute the derivatives of a pre-defined cost function *e.g.* [71, 72]. EnKFs and its variants are usually relatively easier to set up but can be computationally demanding especially when computing a large number of covariance matrices corresponding to the number of observations available for the assimilation. Moreover, EnKFs assume the observation uncertainties are normally distributed [78], which is seldom the case when tackling real-world problems [120]. This encouraged the hydrologists to look into other DA techniques, such as Particle Filters (PFs), which are non linear and present the advantage of not requiring a gaussian distribution of the data. Moreover, their performance is not reliant on a good representation of the error covariance of the model state [120].

Among the various types of observations that can be assimilated in hydrodynamic models, flood extent (FE) and water surface elevation (WSE) are key variables that retain a particular attention since they help identifying flood-prone areas and estimate socio-economic flood damages and risks [113]. The SWOT mission (CNES-NASA) scheduled for launch in November 2022 will provide observations of FE, WSE, width and slope of 90% of the world's water bodies that are wider than 50-100 m, with unprecedented resolutions for a remote sensing tool (one to four revisits every 21 days) [13]. With the collection of consistent and spatially distributed information, inverse modelling can be used to estimate discharge, slope and geometry within a DA framework *e.g.* [40, 65, 85, 93, 129]. Using existing technology, many studies have used *in situ* or EO-derived WSEs, obtained by merging EO-derived FE with a digital elevation model (DEM), to improve flood forecasts [5, 22, 23, 42, 45, 58, 60, 79, 102, 129]. While assimilating WSE

may be straightforward since it is a state variable, the downside of this approach is the requirement of precise flood contour maps and high-resolution topographic datasets [78], which are not always available. Furthermore, several studies have shown that the assimilation of EO-derived FE maps improves flood forecasts, and enables the retrieval of model parameters or boundary conditions *e.g.* [34, 59, 81, 126]. [43] proposed to take into account observation related uncertainties through the use of probabilistic flood maps (PFMs) that are derived from SAR images. The principle of this approach is based on the Bayes theorem, which assigns a probability of a pixel to be flooded depending on its backscatter value. The assimilation of PFMs strongly rely on their precision and on the quality of the hydrodynamic model [90]. In this context, more investigation on this topic needs to be carried out in order to complete relevant literature studies *e.g.* [22, 23, 28, 67, 101].

Another major challenge tied to the hydrodynamic modelling is the lack of hydraulic parameter data that are needed as inputs, such as the river bed shape and elevation. While the knowledge of such information is critical for the good functioning of flood models, it can rarely be available from remote sensing observations, digital elevation models (DEMs), or ground data measurements. Most studies have estimated river discharges and depths assuming the bathymetry and bed roughness to be known *a priori* (see *e.g.* [6, 13]). [129] estimated bathymetry assuming the bed roughness to be known, while [58] gave an estimation knowing the slope information, using a drifting GPS buoy. The complexity of implementing DA to estimate these hydraulic parameters all together have led to the use of simplified models derived from the Saint-Venant equations, proposed in [36, 37, 41]. The methods were assessed on 14 non-braided rivers and at least one of the approaches has shown an improvement of 35% on relative root mean square errors with respect to observed discharges [93].

In this study, we propose to calibrate the SW2D-DDP model, a 2 dimensional shallow water equations model with depth-dependent porosity, in order to retrieve the unknown bathymetry of a river. The porosity functions in this model, enable an easy representation of the bathymetry by a parameter. We assume the bed shape to be trapezoidal, and the bed roughness to be known *a priori*. The DA framework is thus based on integrating PFMs into the SW2D-DDP model *via* a Tempered Particle Filter (TPF), and takes into account the SAR observation and the SW2D-DDP model related uncertainties. The remainder of this paper is organised as follows: first, in Section 3.2., we present the probabilistic flood extent mapping algorithm, the shallow water porosity-based model and the proposed DA framework. Next, we describe the study site and available data in Section 3.3.. Section 3.4. reports and evaluates the results of our study and Section 3.5. discusses our findings and concludes the paper.

## 3.2. Method

### 3.2.1 Probabilistic flood mapping

As observational uncertainty is an important information in DA, we propose here to assimilate probabilistic flood maps (PFMs) because they take into account this uncertainty. These

maps are obtained based on a method previously introduced and developed by [43, 45, 79]. To generate the PFMs, we use SAR images and assume that their backscatter histogram can be approximated using a mixture of two distributions: i) a class of flooded (i.e. wet area including permanent water) pixels ( $f$ ) with low backscatter and ii) a class of non flooded pixels ( $\bar{f}$ ) with higher backscatter both approximated by Gaussian distributions. The Hierarchical Split Based Approach (HSBA) proposed by [19] is used to parameterize the two separate distributions, as flooded area often represents a small fraction of the entire image: the SAR image is iteratively splitted into decreasing size tiles that identify well enough a bimodal histogram, allowing an automatic calibration of the open water bodies distribution. The output is a PFM where each pixel is assigned a probability  $p \in [0, 1]$  of being flooded given its backscatter value  $\sigma^0$ :

$$p(f|\sigma^0) = p(f) \frac{p(\sigma^0|f)}{p(\sigma^0)} \quad (3.1)$$

where  $p(\sigma^0)$  is the probability of recording the backscatter for any pixel, whether it is flooded or not:

$$p(\sigma^0) = p(\sigma^0|f)p(f) + p(\sigma^0|\bar{f})p(\bar{f}) \quad (3.2)$$

$p(f)$  and  $p(\bar{f})$  are the prior probabilities of a pixel being flooded and a pixel not being flooded, respectively. In this study, as this information is unknown, we set  $p(f) = p(\bar{f}) = 0.5$ , as suggested in [43].  $p(\sigma^0|f)$  is the conditional probability of recording the backscatter if the pixel is flooded, and  $p(\sigma^0|\bar{f})$  is the probability distribution of backscatter values of a pixel not being flooded. These two probability distributions are derived from the image histogram, as previously described. More details can be found in [43].

### 3.2..2 The shallow water modelling framework

SW2D<sup>2</sup> is a 2-Dimensional Shallow Water modelling software, that has been continuously developed since 2002. It uses the finite volume method to solve the 2D shallow water equations on unstructured grids. In the standard version of this model, the bottom elevation inside each computational cell holds a unique value obtained by averaging the elevations of the cell's nodes, which means that hydraulic structures affecting water flow can only be represented by cells which are smaller than their dimensions. The Depth Dependant Porosity version of the model (SW2D-DDP) upscales the 2D shallow water equations and introduces a porosity concept that represents the fraction of the cell (or interface) available to the water flow. This allows taking into account small-scale topography variations and hydraulic structures, without the need of detailing their geometry in the mesh. The representation of topographic and bathymetric data is done through coarse grid cells, where each cell is associated with a porosity distribution as a function of the water elevation. As described in [8], the porosity law of the cells located in the floodplain can be retrieved directly from the DEM. "Riverbed cells" – which contain both topographic and bathymetric data – are represented by cells larger than the river width. As

---

<sup>2</sup><https://SW2D.inria.fr/>

the DEM does not provide information below water, a simplified trapezoidal shape is defined using a porosity law of “type 3”, as shown in Figure 3.1. In this figure,  $z_1$  refers to the minimum bottom elevation of the riverbed,  $z_2$  to the maximum riverbed elevation, extracted from the DEM, and  $d$  the river depth, defined as  $d = z_2 - z_1$ . The porosity is therefore variable with water depth (or elevation) and represents the fraction of the cell available for water storage or flow.  $\phi_1$  corresponds to the ratio  $L_1$  over  $L_3$ , the former being the river bottom width, and the latter being the cell width. When the cell is entirely available to the flow,  $\phi$  reaches  $\phi_3$ , taken equal to 1. The SW2D-DDP model simulates water depth maps. Thresholding these maps above 10 cm allows us to generate FE maps, which will be used as input in our DA framework.

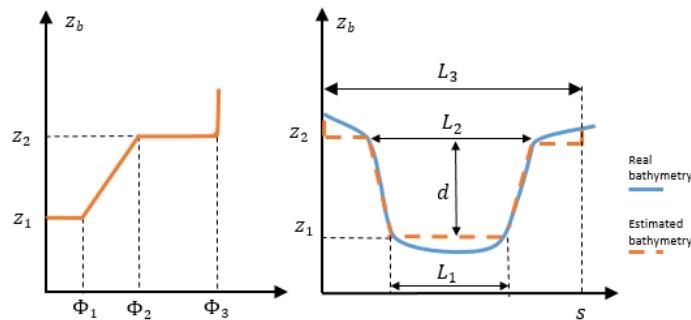


**Figure 3.1:** Riverbed porosity law: Left: Law type 3 attributed to riverbed cells in the mesh; Right: bathymetry representation;  $z$ : elevation,  $\phi$ : porosity,  $d$ : river depth,  $s$ : abscissa along the river cross-section.  $L_1$ : Bottom width;  $L_2$ : River width,  $L_3$ : Riverbed cell width.

### 3.2..3 The data assimilation framework

The goal of this study is to estimate bathymetry, i.e.  $z_1$ , the lowest elevation in the trapezoidal cross section of riverbed cells, as defined in Figure 3.1, via the assimilation of SAR-derived PFMs into the shallow water model SW2D-DDP. The proposed DA framework is based on a particle filter variant call tempered particle filter (TPF) [54, 121]. Particle filters are based on Bayes theorem:

$$p(\theta|o) = p(\theta) \frac{p(o|\theta)}{p(o)} \quad (3.3)$$

where observations  $o$  are assimilated and represent the probability to be flooded knowing the backscatter, given by the PFM (see Eq. 3.1). The SAR-derived information  $o$  is combined with the prediction of the hydraulic model  $\theta$ .  $p(o|\theta)$  is the likelihood, i.e. the probability of the observation knowing the model prediction.  $p(\theta)$  is the prior probability of the model before any observation is taken into account. As usual in a particle filter, the prior (see Eq. 3.4) and posterior probabilities (see Eq. 3.5) are approximated by an ensemble of model realisations called particles:

$$p(\theta) \approx \sum_{j=1}^J \frac{1}{J} \delta(\theta - \theta_j) \quad (3.4)$$

where  $\delta$  is the Dirac delta function and  $\theta_j$  is the model prediction for the  $j^{th}$  particle.

Combining Eq. 3.4 and Eq. 3.3 gives the posterior probability:

$$p(\theta|o) \approx \sum_{j=1}^J W_j \delta(\theta - \theta_j) \quad (3.5)$$

where  $W_j = \frac{p(o|\theta)}{p(o)}$ .

In this study, the likelihood ( $p(o|\theta)$ ) is obtained by multiplying the local weights associated with the individual pixels  $k$  across the simulated area according to the formula used in [59] and [34]. The local weight represents the adequacy between the probability of a pixel being flooded given from the PFM, and the prediction of the hydraulic model that is equal to 1 if the area is predicted as flooded, and 0 otherwise. The main underlying assumption is that observations are independent from each other across time and space.

Ensemble collapse, also known as degeneracy, occurs when only a few high weight particles remains as a result of the assimilation while other particles get a negligible weight. In order to circumvent this limitation, [54] proposed the factorization of the likelihood (see Eq. 3.6) in the application of the Bayes theorem iteratively. This factorization is carried out through an iterative process enabling to smooth out the transition from the prior to the posterior probability, which makes it particularly interesting for calibration purposes. With the inflation of the likelihood variance and the reduction of the weight variance, more particles with significant weights are kept. [34] demonstrated through a synthetic test case assimilation of FE, that this factorization helps reducing degeneracy.

$$\frac{p(o|\theta)}{p(o)} = \prod_{i=1}^I \left( \frac{p(o|\theta)}{p(o)} \right)^{\alpha_i} \quad (3.6)$$

where  $0 < \alpha_i < 1$  for each iteration  $i$ , and  $\sum_{i=1}^I \alpha_i = 1$ .

The DA framework consists of the following steps:

- We first make a random guess of the parameter sets  $z_1$  with the same initial weight. The random guess will be referred to as Open Loop (OL) in the remainder of the study; it represents the results before the assimilation.
- The sampled particles representing the parameters, are then assigned a likelihood weight that represents their probability being sampled from the posterior density function.
- At each iteration  $i$ , the model is run and provides predictions  $\theta_i$ , the observation data is assimilated, and the likelihood of the model output  $p(o|\theta_i)$  is computed.

The tempering coefficient value  $\alpha_i$  is optimized so that the ensemble inefficiency ratio  $\text{Ineff}_{\alpha}$  equals a target value  $r^*$ :

$$\text{Ineff}(\alpha_i) = \frac{1}{J} \sum_{j=1}^J (W_j^i(\alpha_i))^2 \quad (3.7)$$

$\text{Ineff}_{\alpha_i}$  gives an indication of how many particles keep a significant weight. For instance when  $\text{Ineff}(\alpha_i) = 2$ , it means that half of the particles have significant weights. These particles

with the highest weights are used to carry out a sequential importance re-sampling (SIR) [46], in order to get replicated particles. The number of replicas of each particle directly relates to its importance weight. The particles with low weights are therefore replaced by replicas of particles with higher weights, so that the total number of particles remains unchanged. Replicating particles with the highest weight iteratively, will make particles equally weighted after re-sampling. Even though it is a powerful tool in reducing the degeneracy, SIR potentially comes with sample impoverishment. This occurs quite often when particles with high weights are likely to be drawn multiple times during re-sampling, which may result in a loss of diversity among particles [1]. In order to circumvent this limitation and re-gain diversity across the particles, a mutation is applied to the particles by perturbing the parameters, using a Metropolis-Hastings (MH) [54]; we add to the parameter values ( $z_1$ ) or the re-sampled particles a random number taken from a gaussian distribution of zero mean value and a low variance. Then the ratio between the perturbed (after mutation) and re-sampled (before mutation) likelihoods is compared to a randomly generated number  $u \in [0, 1]$  to accept or reject new particles. If the ratio of the likelihoods is greater than  $u$ , we accept the new particle, and if not we reject it and keep the particle as before its mutation. This ensures the best particles with the higher likelihoods are kept. The accepted particles then replace the corresponding replicates. The mutation procedure is repeated twice. Next the sequence of SIR and two mutations is carried out again, using a new value of  $\alpha_{i+1}$ . This sequence is repeated until the  $\alpha_i$  values sum up to one so that the likelihood factorization is completed and the bayes theorem is respected.

### 3.3. Study site, available data and experimental design

#### 3.3.1 Study site and available data

The study site, covering an area of 1,50 km<sup>2</sup>, is located at the confluence of the Severn and Avon Rivers in the United Kingdom, around the urban area of Tewkesbury. Figure 3.2 shows the model domain, the available gauging stations and river camera, and the riverbed cells in the two considered reaches separated by the confluence: the Severn River and the Avon River. Stations upstream, at Saxons Lode and Bredon provide flow rates and water levels and the station downstream at Deerhurst provides water levels. Mythe Bridge, an internal gauging station, and Tewkesbury with a river camera view (detailed description in [122]), provide water surface elevation (WSE) measurement data which are used for evaluation purpose. Topography data is derived from a LiDAR DEM at 2 m spatial resolution, and re-sampled at 10 m, with a vertical accuracy of 0.10 m. Moreover, river cross-sections (see Figure 3.4) are available at the stations of Saxons Lode, Bredon, and Deerhurst. Hydrometric and topography data have been provided by the UK Environment Agency, and will be used in this study for the purpose of evaluation. Furthermore, a previous study [8] (hereby referred to as ADWR in the remainder of the study) is a control simulation considered as a reference for the evaluation. In this simulation, discharge time series were imposed as upstream boundary conditions of the hydraulic model (Severn at Saxons Lode and Avon at Bredon). The streamflow time series in Saxons Lode were

derived from water surface elevation records using a rating curve. Water level time series were used as downstream boundary condition at Deerhurst. The initial condition is a fixed water level equal to the downstream condition. A uniform Strickler coefficient  $K_s = 50 \text{ m}^{1/3}\text{s}^{-1}$  was used for the river course.

In our study, we use the flood event of July 2012 as a test case because it has been well observed in a time series Cosmo-SkyMed images. These images with HH polarization and a spatial resolution of 5m are further detailed in [78]. They are used to derive out PFMs on the following dates: 27 November; 28 November; 29 November; 30 November; 01 December; 02 December (see Figure 3.3). The images were mainly acquired just after the flood peak and during the falling limb of the hydrograph. As the SAR has some limitations for detecting water under vegetation and around buildings an exclusion layer is used to mask areas of vegetation, permanent waters and buildings in the map. It was derived using the method proposed in [132] from Sentinel 1 images acquired between 2016 and 2018.

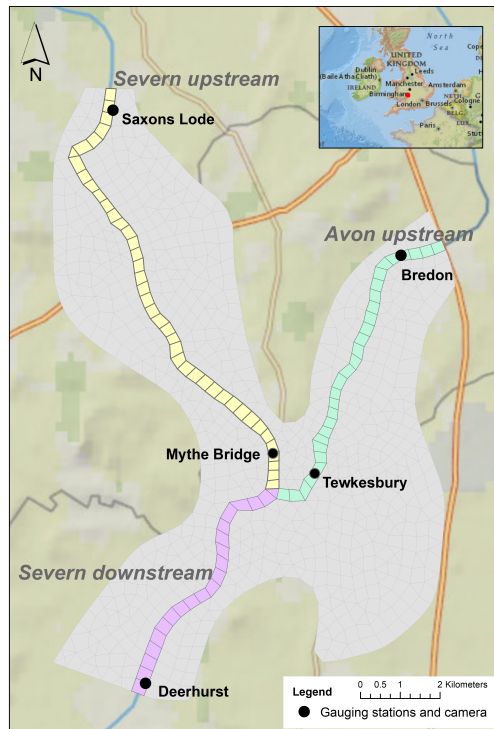


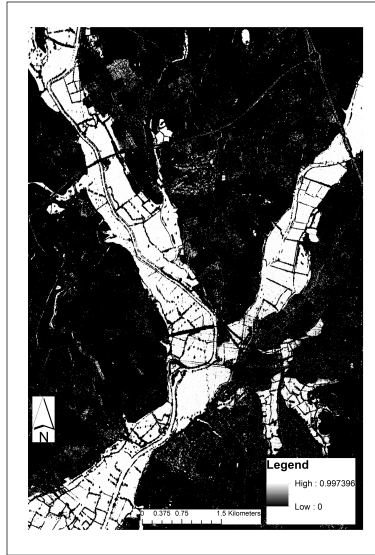
**Figure 3.2:** Study site showing the three river reaches and the available gauging stations and river camera.

### 3.3..2 Experimental design

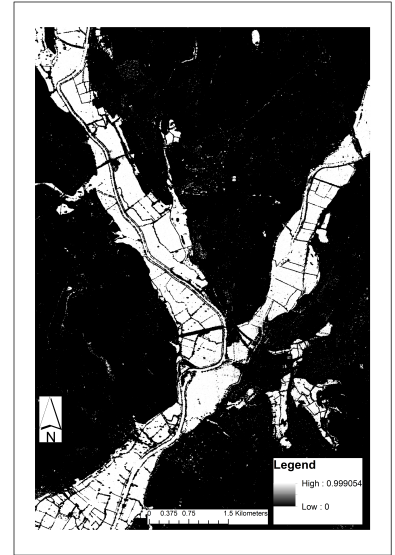
Streamflow time series at Saxons Lode and Bredon are used as upstream boundary conditions of the SW2D-DDP model. The initial condition is defined as a fixed uniform water depth in the riverbed. The downstream boundary condition is set as a Froude number (see Eq. 3.8) to have a more “free” condition in comparison to a prescribed water elevation. The Froude number is



(a) Image 1: 27 November



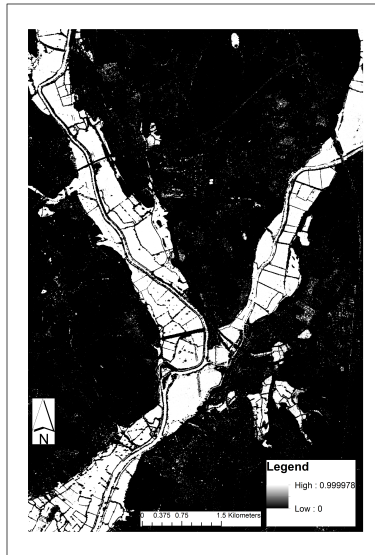
(b) Image 2: 28 November



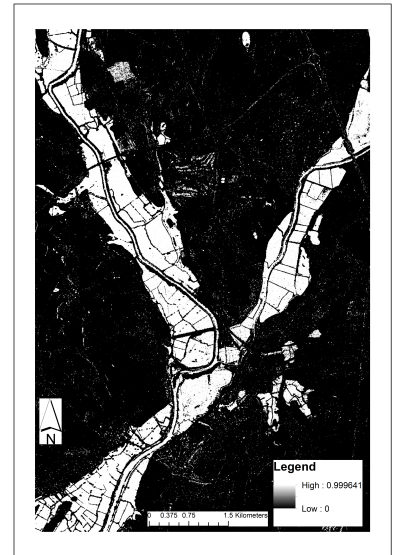
(c) Image 3: 29 November



(d) Image 4: 30 November



(e) Image 5: 01 November



(f) Image 6: 02 November

*Figure 3.3:* CosmoSky-Med probabilistic flood maps for the 2012 event.

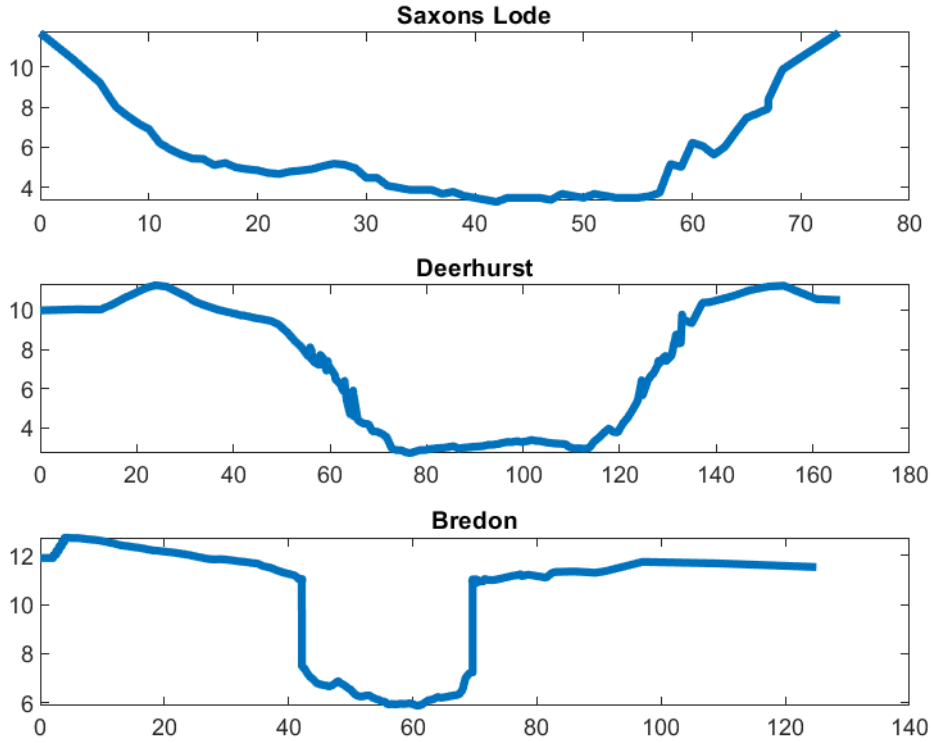


**Figure 3.4:** Cross sections at Saxons Lode, Bredon and Deerhurst.

computed as:

$$\text{Fr} = \frac{u}{\sqrt{gh}} \quad (3.8)$$

where  $u$  is the water velocity,  $h$  water height and  $g=9.81$  the gravitational constant. In SW2D-DDP, one WSE is computed by cell. However, bathymetry information is available on a sub-grid level, at the spatial resolution of the DEM used. Therefore, there is a spatial distribution of water heights computed as  $h = z - z_b$ , in a unique cell. In equation 3.8 the maximum water height in the cell is used, yielding artificially small values of the Froude number. In this application, the downstream Froude value was set to increase linearly from 0 to reach a “steady value” (SV) of 0.04 after four days. This estimation comes from a control simulation that used a water level hydrograph as a downstream boundary condition. Since this information is not always available due to the lack of streamflow data, we choose to further investigate the calibration of “steady value” of the Froude number along with the bathymetry.

The objective of the proposed data assimilation framework is to calibrate the river bottom elevation  $z_1$ , i.e. bathymetry. Since the mesh is composed of 93 riverbed cells, the calibration of  $z_1$  independently for each cell could potentially lead to contrasted and spatially inconsistent  $z_1$  values along the river channel. We therefore choose to use uniform longitudinal river slope values between the three boundaries of the hydraulic model: Saxons Lode, Bredon and Deerhurst (see Figure 3.2). Two slopes are obtained: one for the Severn River and another for the Avon River. Our calibration is thus limited to three parameters, corresponding to the bottom elevations of the riverbed cells located at at the three above mentionned gauging stations. We further

simplify and test the calibration of a unique parameter: the bottom elevation downstream, while imposing uniform slopes. The bottom elevations upstream are then deducted by adding an estimated “delta elevation” of 1.5 m for Saxons Lode and 2 m for Bredon. This estimation comes from the DEM and holds the assumption of the river channel slope being equal to the floodplain slope.

Therefore in total, we have four tests in which we calibrate one or more parameters:

- 1param ( $z_{1_{ds}}$ ): in this scenario, we calibrate  $z_1$  downstream, impose slopes, and deduct the two others  $z_1$  values in the upstream boundaries. The SV Froude number at downstream boundary is fixed to 0.04;
- 2param ( $z_{1_{ds}}, Fr$ ): in this scenario, we calibrate  $z_1$  downstream and the SV Froude number at downstream boundary;
- 3param ( $z_{1_{ds}}, z_{1_{up1}}, z_{1_{up2}}$ ): in this scenario, we calibrate the two  $z_1$  values upstream along with the downstream value. The SV Froude number downstream is fixed to 0.04;
- 4param ( $z_{1_{ds}}, z_{1_{up1}}, z_{1_{up2}}, Fr$ ): in this scenario, we calibrate the three  $z_1$  values and the SV Froude number at downstream boundary.

In our application, the ensemble is composed of 16 particles. The six available CosmoSky-Med images are assimilated using the TPF all at once.

### 3.4. Results

To investigate the TPF assimilation performance, we evaluate the assimilation results in terms of WSE predictions, against WSE observations at two gauging stations that are located inside the hydraulic domain: Mythe Bridge and Tewkesbury (see Figure 3.2). We first visually evaluate discrepancies between the simulated and the observed WSEs, by plotting the time series of WSEs for all particles for the OL (before the assimilation), and the posterior (after the assimilation), see Figure 3.5 to 3.12.

WSE time series show the OL ensemble (black) encompasses the observation (red) most of the time, in all scenario tests. The posterior particles are very similar and close to the observation, while slightly underestimating WSE at Mythe Bridge and Tewkesbury. This might be related to an overestimation of the river width, or underestimation of the calibrated bottom elevation  $z_1$ .

We also compute root mean square errors as:

$$RMSE = \sqrt{\frac{1}{K} \sum_{k=1}^K (z_{OL} - z_o)^2} \quad (3.9)$$

In Table 3.1, performances in terms of RMSEs are presented for the OL- and the posterior-derived WSEs, at Mythe Bridge and Tewkesbury. Moreover, in Table 3.2, we present the

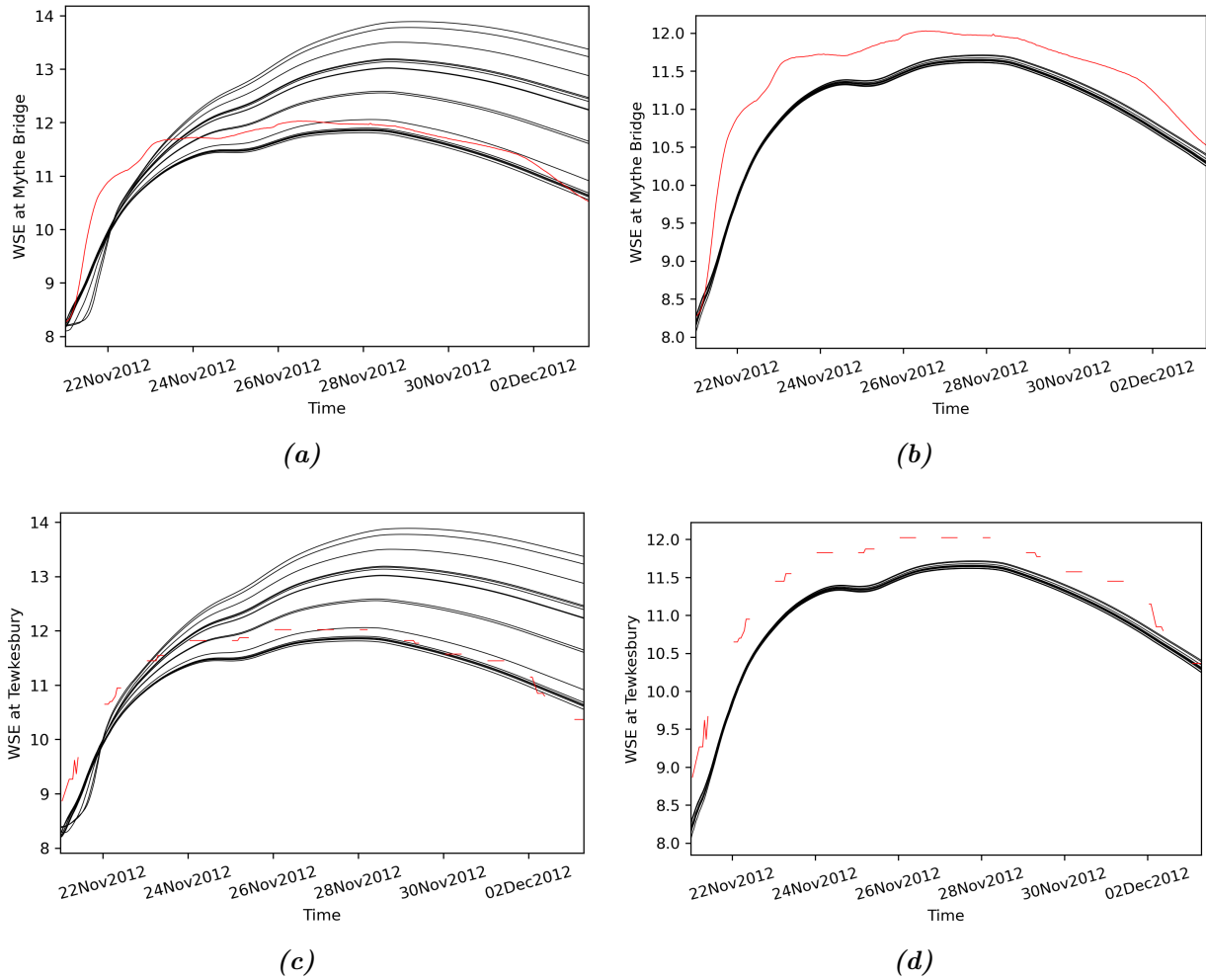


**Figure 3.5:** Test 1param daily time series of the water surface elevations, for a) the OL and b) the last iteration. Black lines correspond to the particle ensemble and the red line to the observation, at Mythe Bridge.

mean and standard deviation of the particles'  $z_1$ , for the OL and the posterior, at Saxons Lode, Bredon and Deerhurst where observed cross sections are available (see Figure 3.2 for the stations' location). Table 3.1 shows that in all tests performed, the low values of standard deviations of the posterior RMSEs indicate that the convergence of the TPF is reached. Results at Mythe Bridge show that the posterior RMSE does not reach the precision obtained with the ADWR simulation. However, for Tewkesbury, tests that calibrated 3 or 4 parameters showed an improvement of the posterior, not only with respect to the OL, but also with respect to ADWR values. This means that the calibration of the three  $z_1$  parameters on the boundaries of the hydraulic domain leads to the most accurate results. The calibration of the Froude number along with bathymetry does not seem to significantly affect the assimilation results. However, it is interesting to calibrate both Froude and bathymetry, since they are often unknown *a priori*. On another note, in all tests, the use of the exclusion layer does not seem to have a marked effect on the improvement of the assimilation results. Table 3.2 shows the calibrated  $z_1$  values, i.e. posterior, have lower standard deviations than those of the OL. However, they do not correspond to the observed values, for the three locations. This might be linked to

**Table 3.1:** RMSE performances ( $\pm$  standard deviation) for the OL and the posterior derived WSEs, for the different scenario tests. Performances obtained with the ADWR control simulation: RMSE(Mythe Bridge)=0.24; RMSE(Tewkesbury)=0.43.

	Mythe Bridge		Tewkesbury	
	OL	Posterior	OL	Posterior
1param	0.82 $\pm$ 0.46	0.51 $\pm$ 0.02	0.82 $\pm$ 0.47	0.46 $\pm$ 0.02
1param + ExLay	0.97 $\pm$ 0.45	0.52 $\pm$ 0.006	0.98 $\pm$ 0.45	0.48 $\pm$ 0.01
2param	0.8 $\pm$ 0.43	0.49 $\pm$ 0.04	0.8 $\pm$ 0.44	0.45 $\pm$ 0.04
2param + ExLay	0.79 $\pm$ 0.45	0.51 $\pm$ 0.02	0.8 $\pm$ 0.45	0.47 $\pm$ 0.02
3param	0.91 $\pm$ 1.06	0.41 $\pm$ 0.02	0.92 $\pm$ 1.17	0.33 $\pm$ 0.02
3param + ExLay	1.10 $\pm$ 0.77	0.42 $\pm$ 0.005	1.14 $\pm$ 0.90	0.33 $\pm$ 0.005
4param	0.88 $\pm$ 0.72	0.41 $\pm$ 0.01	0.90 $\pm$ 0.86	0.33 $\pm$ 0.01
4param + ExLay	1.22 $\pm$ 0.77	0.42 $\pm$ 0.01	1.28 $\pm$ 0.87	0.34 $\pm$ 0.01

**Table 3.2:**  $z_1$  Parameter means and standard deviations obtained for the OL and the posterior, for the different scenarios. Observed river bottom values on observed cross sections: Saxons Lode:  $z_1=4.39\pm 0.9$ ; Bredon:  $z_1=6.43\pm 0.44$ ; Deerhurst:  $z_1=3.8\pm 0.17$ .

	Saxons Lode		Bredon		Deerhurst	
	OL	Posterior	OL	Posterior	OL	Posterior
1param	5.47 $\pm$ 2.04	2.43 $\pm$ 0.22	6.47 $\pm$ 2.00	3.43 $\pm$ 0.22	3.97 $\pm$ 2.04	1.06 $\pm$ 0.08
1param + ExLay	6.25 $\pm$ 1.78	2.32 $\pm$ 0.15	7.27 $\pm$ 1.84	3.31 $\pm$ 0.17	4.75 $\pm$ 1.78	1 $\pm$ 0.00
2param	5.32 $\pm$ 2.03	2.49 $\pm$ 0.30	6.32 $\pm$ 2	3.47 $\pm$ 0.35	3.82 $\pm$ 2.02	1.13 $\pm$ 0.16
2param + ExLay	5.60 $\pm$ 1.76	2.37 $\pm$ 0.21	6.59 $\pm$ 1.75	3.35 $\pm$ 0.25	4.09 $\pm$ 1.75	1.03 $\pm$ 0.06
3param	7.54 $\pm$ 1.43	6.33 $\pm$ 0.57	8.14 $\pm$ 0.98	7.22 $\pm$ 0.46	6.19 $\pm$ 2.17	1.04 $\pm$ 0.07
3param + ExLay	6.53 $\pm$ 2.23	6.69 $\pm$ 0.26	7.93 $\pm$ 1.36	7.31 $\pm$ 0.24	4.69 $\pm$ 2.49	1.00 $\pm$ 0.01
4param	6.33 $\pm$ 1.86	6.74 $\pm$ 0.40	7.47 $\pm$ 1.54	7.28 $\pm$ 0.34	3.86 $\pm$ 2.78	1.03 $\pm$ 0.05
4param + ExLay	7.13 $\pm$ 1.61	6.33 $\pm$ 0.4	8.15 $\pm$ 0.84	6.93 $\pm$ 0.51	5.27 $\pm$ 2.18	1.03 $\pm$ 0.06

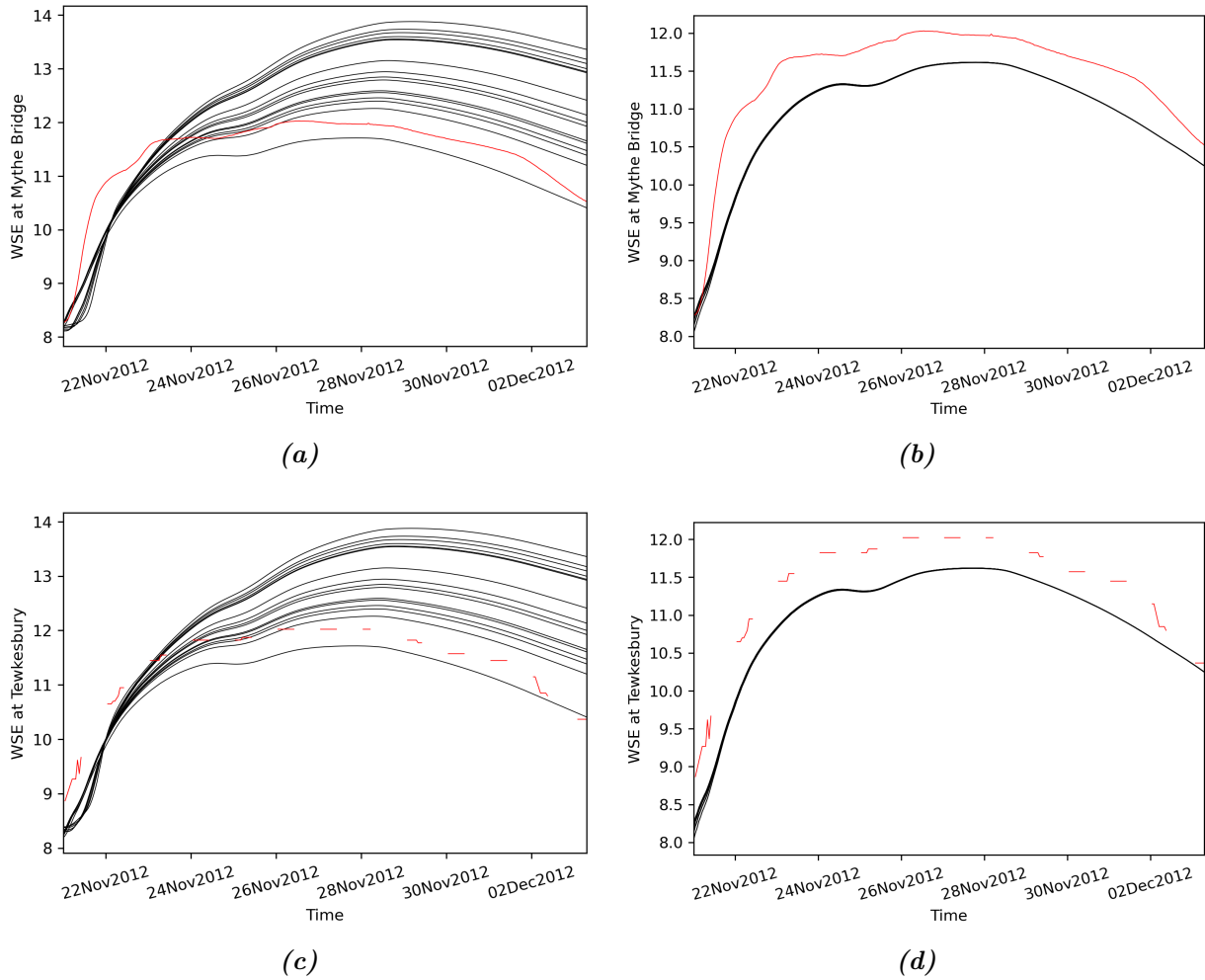


**Figure 3.6:** Test 1param + ExLay daily time series of the water surface elevations, for a) the OL and b) the last iteration. Black lines correspond to the particle ensemble and the red line to the observation, at Mythe Bridge and Tewkesbury.

the fact that the calibration of a simplified effective bathymetry also relies on many other hydraulic parameters such as: the river bank slopes, the river width, the shape of the river we have assumed. The simplified bathymetry estimated in SW2D-DDP, is trapezoidal, and was characterized with a river width wider, than that observed. This might explain that calibrated parameters obtained for Bredon, are slightly higher, than the observed  $z_1$ . On another note, the calibration of  $z_1$  downstream at Deerhurst, seems to lead to the same results no matter which calibration scenario is considered. We notice a strong variability of model calibration results between the first two tests where we calibrate the  $z_1$  downstream and the other two tests where we calibrate the  $z_1$  for the three locations: calibrated  $z_1$  values vary between approximately 2 to 6 m in Saxons Lode, and 3 to 7 m in Bredon. This is related to the estimated “delta elevation” used in the first two calibration tests.

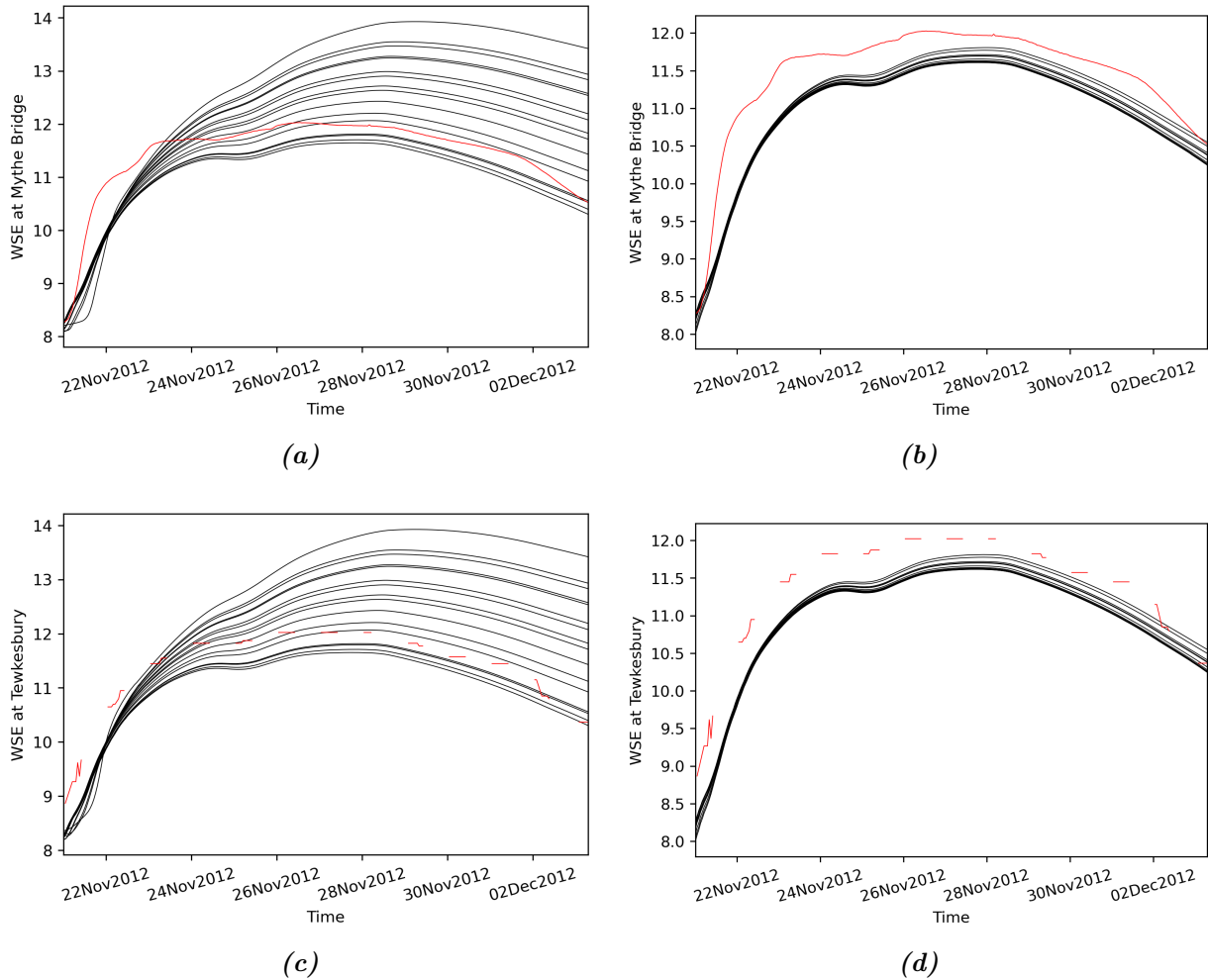


**Figure 3.7:** Test 2param daily time series of the water surface elevations, for a) the OL and b) the last iteration. Black lines correspond to the particle ensemble and the red line to the observation, at Mythe Bridge and Tewkesbury.

### 3.5. Discussion and conclusion

In this study, we have proposed a framework to assimilate Earth Observation (EO)-derived flood extents (FE) into a shallow water model, namely SW2D-DDP, using a tempered particle filter (TPF). The objective of this framework is to estimate an unknown parameter that is often required as input information in flood forecasting models: bathymetry. The assimilation has shown that the estimation of the bathymetry is efficient, with rather satisfying root mean squared errors (RMSE) of less than 0.5 m, using the calibration of bottom elevations distributed across the hydraulic domain, assuming the Froude number is known. The calibration of the effective bathymetry along with the Froude number delivered very similar results. The accuracy of a controlled simulation with known bathymetry is not reached for the Severn reach. The calibration of distributed bottom elevations was therefore more accurate than the simple calibration of a single parameter, in one location. The exclusion layer use did not seem to impact the assimilation results. The calibrated parameters obtained were not equal to the observed punctual values. This is likely because bathymetry in SW2D-DDP was estimated with

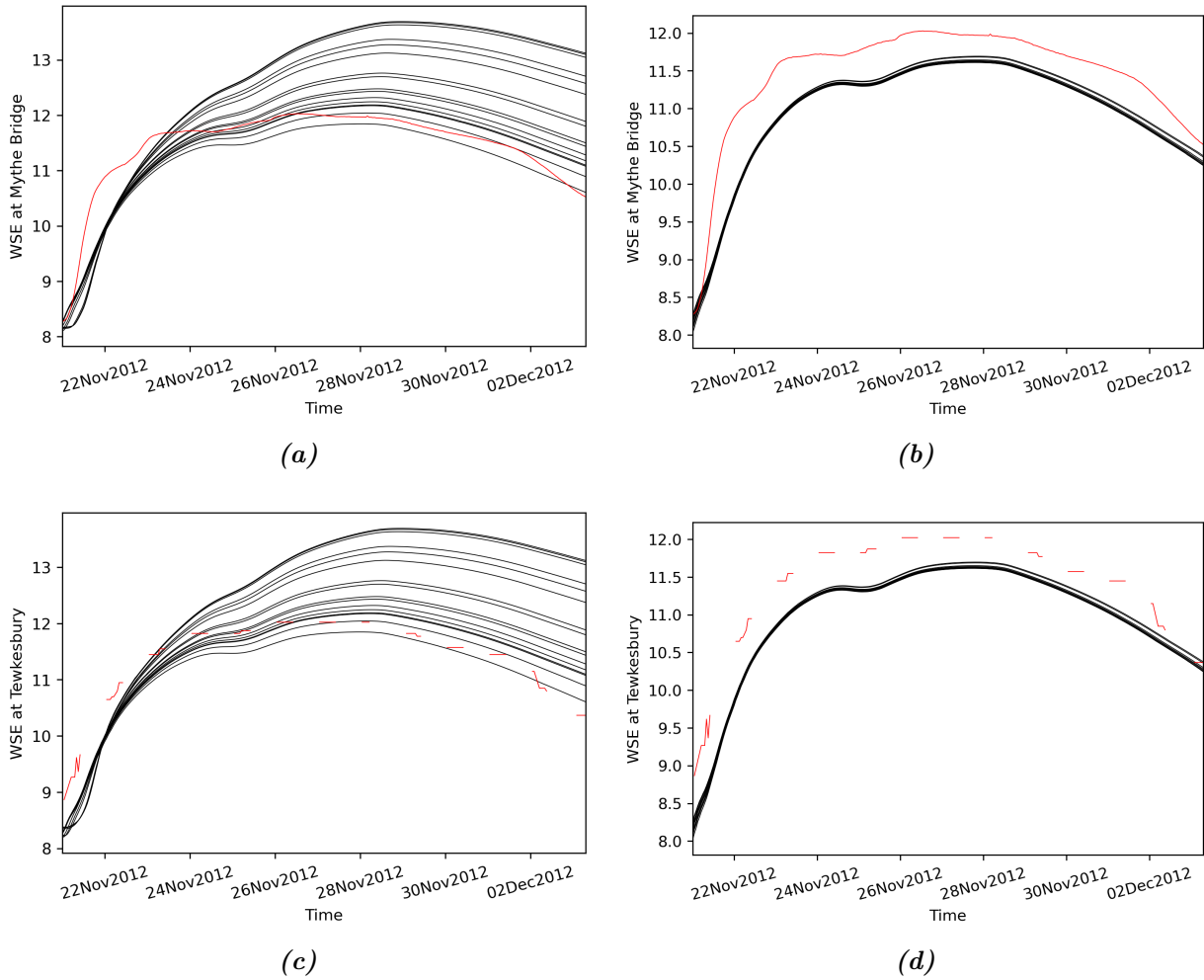


**Figure 3.8:** Test 2param + ExLay daily time series of the water surface elevations, for a) the OL and b) the last iteration. Black lines correspond to the particle ensemble and the red line to the observation, at Mythe Bridge and Tewkesbury.

punctual cross-sections, and based on many assumptions that could have made the river width over-estimated for instance. In fact, calibrating the effective bathymetry with only a few information, makes a compromise between the different hydraulic parameters that are missing as an input.

Another factor that might be influential in this DA framework, is the timing of available observations to assimilate. In our case, all images were available after the flood peak, which tells us about flow dynamics mainly happening in the floodplain. This might hamper the calibration of bathymetry, since the sensitivity of the bathymetry to the flood extent is more limited in this phase of the flood event. In future tests, the availability of images providing a higher variability of flood extents across the time series, may be beneficial for the bathymetry retrieval.

In conclusion, the preliminary results of this study are quite interesting but deserve to be further analysed, and tested with different types of data and on different site areas. A main outcome of the study shows that we are able to calibrate the Froude number with bathymetry, if both these data are not available, which opens up new perspectives of model calibration via the proposed DA algorithm, namely in data scarce areas but where SAR images are available.

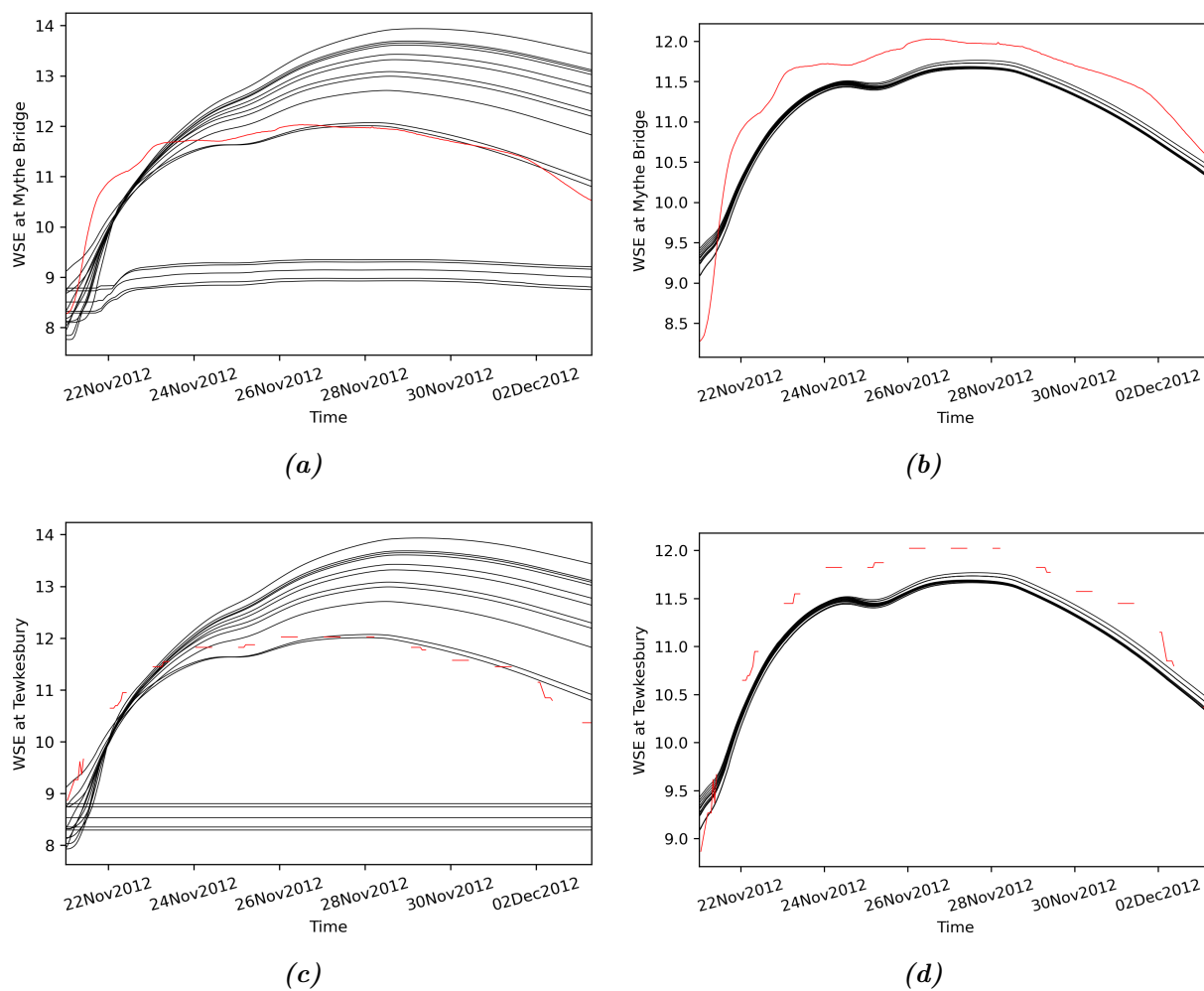


**Figure 3.9:** Test 3param daily time series of the water surface elevations, for a) the OL and b) the last iteration. Black lines correspond to the particle ensemble and the red line to the observation, at Mythe Bridge and Tewkesbury.

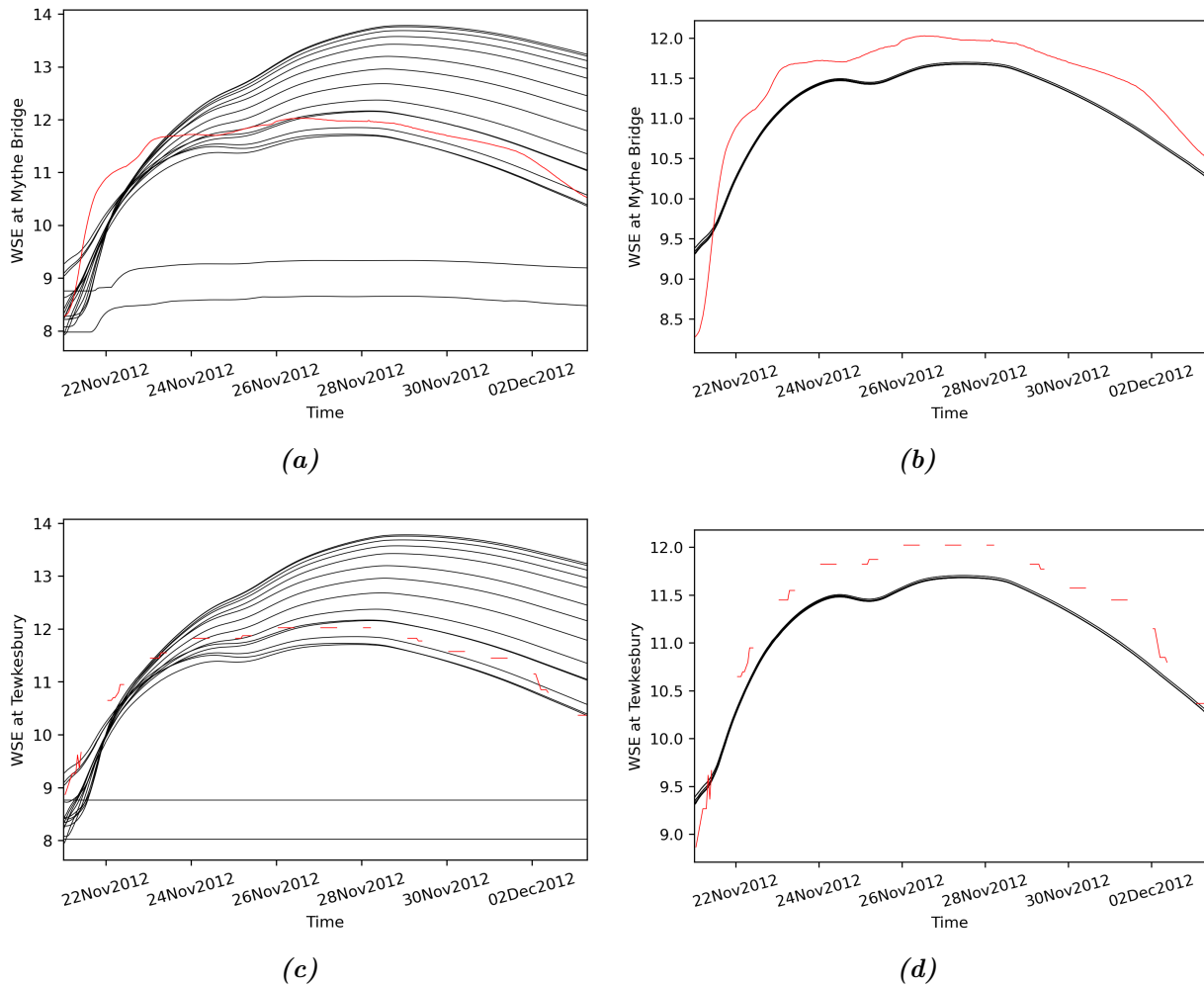


**Figure 3.10:** Test 3param + ExLay daily time series of the water surface elevations, for a) the OL and b) the last iteration. Black lines correspond to the particle ensemble and the red line to the observation, at Mythe Bridge and Tewkesbury.

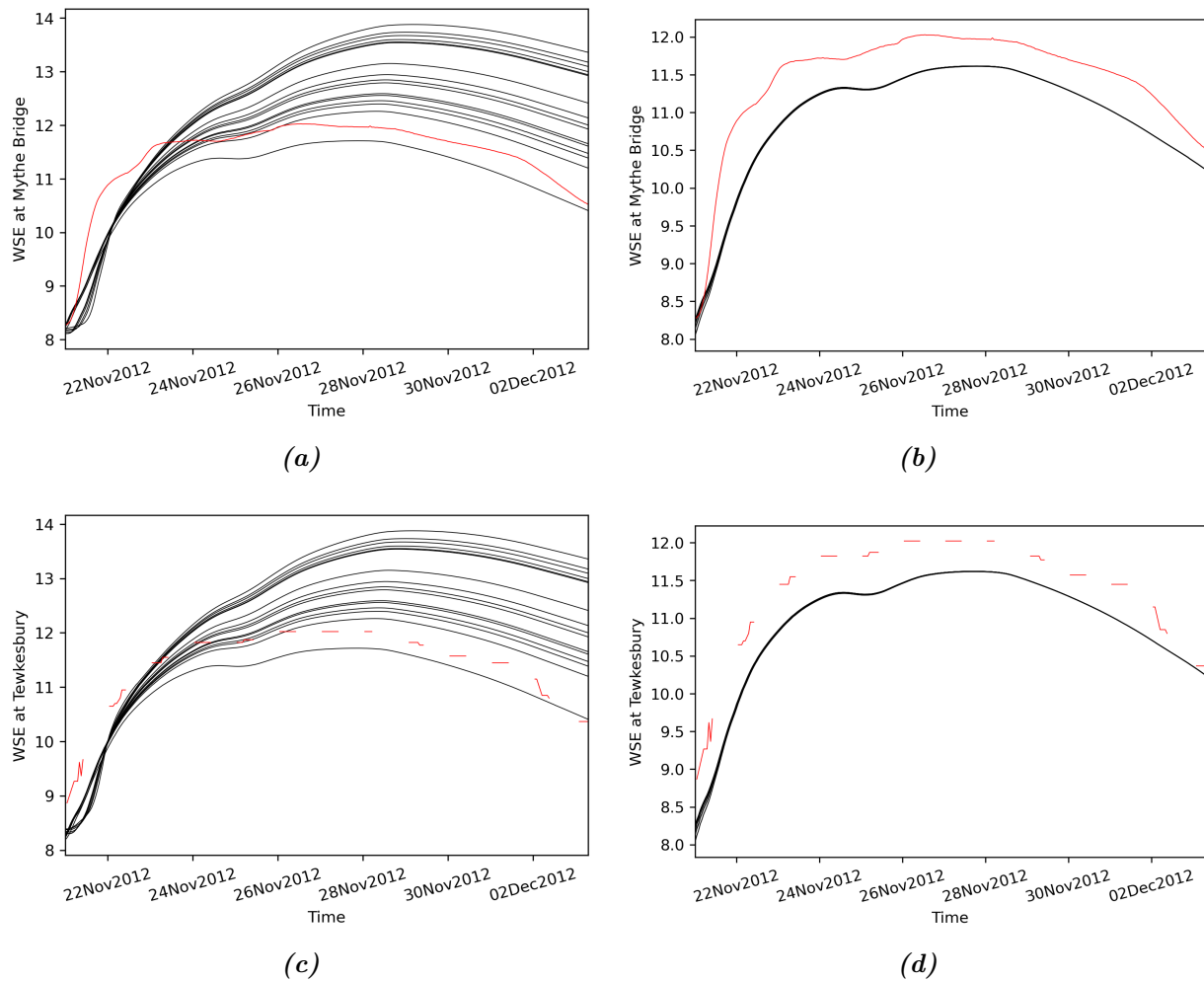


**Figure 3.11:** Test 4param daily time series of the water surface elevations, for a) the OL and b) the last iteration. Black lines correspond to the particle ensemble and the red line to the observation, at Mythe Bridge and Tewkesbury.

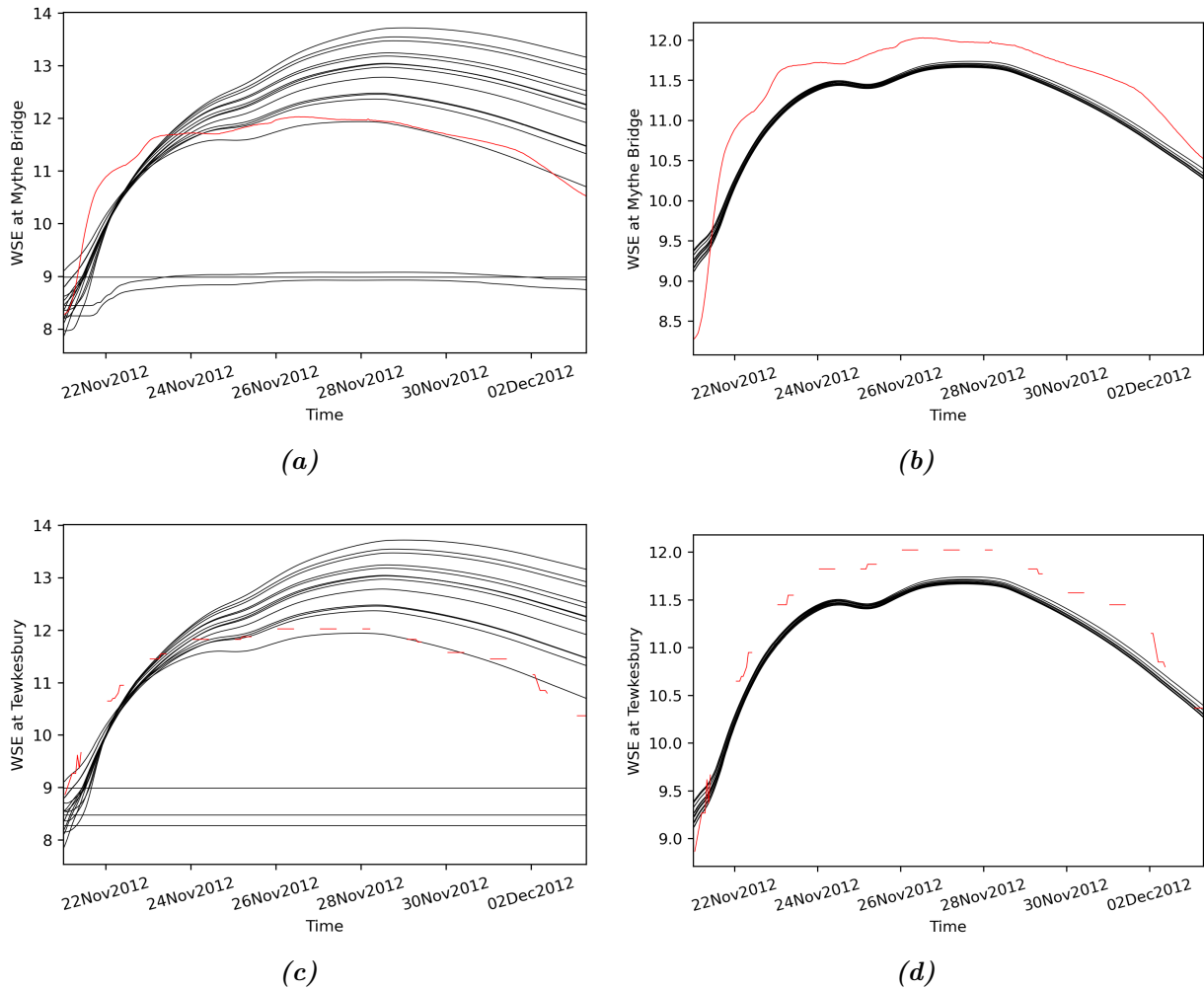


**Figure 3.12:** Test 4param + ExLay daily time series of the water surface elevations, for a) the OL and b) the last iteration. Black lines correspond to the particle ensemble and the red line to the observation, at Mythe Bridge and Tewkesbury.

# General Conclusions and Perspectives

*Do not say a little in many words but a great deal in a few!*

Pythagoras of Samos

This research study has examined several novel methodologies that have the potential to improve flood forecasting systems. The contributions of this PhD thesis to advance research can be summarised as follows:

1. we proposed a hydrodynamic modelling framework enabling fast flood simulations at high accuracy and applicable at large scales,
2. we developed an unsupervised automatic algorithm for water level estimation using only a satellite-derived flood extent map and a digital elevation model,
3. We proposed and evaluated a data assimilation framework that aims to retrieve unknown parameters such as bathymetry of a shallow water model.

In the first part of this thesis, we proposed a flood modelling framework based on a 2 dimensional shallow water model with depth dependant porosity (SW2D-DDP [50]) and evaluated it with respect to the standard version of the model (SW2D), considered as a benchmark. As porosity models were mostly developed for urban flood mapping, a special feature is that they enable to represent buildings within comparatively larger cells via porosity laws. The novelty of our work lies in the representation of small scale topography within large cells not only in the floodplain but also the riverbed. For the first time, the DDP model is applied over areas larger than urban settlements, with an automatic estimation of the porosity parameters from the DTM and river shape information only. The evaluation of water surface elevations at gauging stations has shown the porosity-based model (SW2D-DDP) performs as good as a standard shallow water model (SW2D), with average RMSDs lower than 15 cm. In terms of flood mapping, the proposed model had a similar performance to the benchmark model with approximately 90 % agreement during the flood peak. Discrepancies between the two model-derived flood maps were observed during the rising and the falling limbs. This was probably related to a faster flooding and receding dynamic in the porosity model due to its ability to represent small scale topography and drains via porosity. SW2D-DDP was found to run with a computational time reduced by a factor of 350, and was much easier to set up than SW2D (particularly when it comes to the discretization of the study area). The proposed modelling

approach therefore enabled us to treat bathymetry as a model calibration parameter in the third part of the thesis.

In the second part, we proposed the WaSER (WATER Surface Elevation Retrieval) algorithm enabling the automatic generation of refined water extent and depth maps using the fusion of satellite and topography data only. Datasets of various spatial resolutions were available to test: DEMs (LiDAR at 2 m, CopDEM at 10 m and SRTM at 30 m) and SAR images (TerraSAR-X at 3 m and Envisat at 150 m). Three variants of this algorithm based on the same rationale but using different intermediate steps were tested and inter-compared. The algorithm steps are based on: i) thresholding topographic data (HAND or DEM) at global or local scale to produce synthetic flood extent (FE) maps, ii) optimising the threshold by selecting the synthetic map that presents the best agreement with the satellite EO-FE map, and iii) generating water depth (WD) and water surface elevation (WSE) maps. One of the goals was to evaluate, using an aerial photograph and the results of SW2D-DDP, which variant was the best performing, depending on the resolution of the data used. It has been found that in terms of flood mapping, the two local variants of WaSER presented similar extents to those observed in the SW2D-DDP maps. Moreover, these variants outperformed the exclusive use of SAR flood mapping, reaching an accuracy of 86-91%. In terms of water surface elevation mapping, the local variants were the most performing with the combination of high resolution images (*e.g.* TerraSAR-X at 3 m) and topographic datasets (*e.g.* LiDAR at 2 m). With these approaches and data, the the difference with SW2D-DDP results reached 0.69 and 0.52 m respectively. The accuracy of the results is highly related to the precision of the DEM used. The HAND global variant was found to be the best performing, reaching errors of approximately 0.90 m compared to SW2D-DDP results, while combining low to medium resolution images (*e.g.* Envisat at 150 m) and DEMs (*e.g.* SRTM at 3 m). In that scenario, the level of precision of the DEM used was not able to predict well the directions of water flow; in order to obtain accurate results, the compatibility of the level of information detail brought by the topography and satellite data is essential. The proposed method enables an accurate estimation of spatially distributed water surface levels, and while it is not meant to replace hydraulic models, it constitutes a relevant tools for a rapid flood mapping without implementing any hydraulic calculations.

In the third part, we proposed a data assimilation algorithm based on a tempered particle filter to calibrate the SW2D-DDP model using probabilistic flood maps. One of the goals was to calibrate the bathymetry using the porosity parameters. To do so, we proposed a calibration using three parameters in the “riverbed cells” located on the boundaries of the hydraulic model. A simpler configuration suggested the calibration of a single parameter located in the downstream, and deducting the two remaining parameters by approximating a “delta elevation” estimated from topography data. We also chose to test the calibration of the downstream elevation-discharge boundary condition *via* the Froude number along with bathymetry. Results have shown that the calibration of the bathymetry using three parameters yielded good results in terms of water surface elevations with RMSEs less than 0.5 m after assimilation, compared to the observed water levels at gauging stations inside the hydraulic model domain. However, the

calibrated parameters obtained were not equal to the observed punctual values. This is probably due to the fact that the SW2D-DDP bathymetry was estimated based on many assumptions that might have overestimated river width, for example. In fact, the assimilation enabled the retrieval of an effective bathymetry that compensated the errors in river bank slopes, widths, *etc.* Moreover, it has been found that the calibration of the Froude number does not greatly impact the assimilation results, but can be of great benefit to retrieve unknown data for site applications where *in situ* data and hydraulic parameter information are missing.

Potential future research that may follow up this thesis are given next:

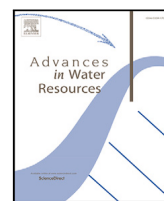
1. Apply of the porosity-based shallow water model on large and ungauged rivers such as the Mozambique and the Amazon rivers, to enable the automatic estimation of sub-grid topography/bathymetry and use it as input in flood forecasting models;
2. Conduct a sensitivity study on the effect of the local window size (parameter in WaSER) used in the local variants.
3. Further test the WaSER algorithm with different types of data of various resolutions, and on different areas characterized with complex topographies.
4. Flood mapping using the HAND global variant of WaSER is applicable anywhere in the world with the availability of free topography and satellite datasets.
5. Flood extent and depth maps coming from the WaSER algorithm can also be used as time series observations for the calibration of a hydraulic model, via the proposed data assimilation algorithm;
6. The data assimilation framework should be further tested with multi-event data and on different study areas, where more evaluation data is available.

## Acknowledgements

This thesis was supported by the National Research Fund of Luxembourg through the CASCADE project (Grant no. C17/SR/11682050).

# Author Publications

- Vita Ayoub, Carole Delenne, Marco Chini, Pascal Finaud-Guyot, David Mason, Patrick Matgen, Ramona Maria-Pelich, and Renaud Hostache. A porosity-based flood inundation modelling approach for enabling faster large scale simulations. *Published in Advances in Water Resources*, 162:104141, 2022.
- Vita Ayoub, Renaud Hostache, Patrick Matgen, Marco Chini, Ramona Maria-Pelich, and Carole Delenne. Estimating flood depth from space: an automatic method based on satellite flood imagery and topography data. *Submitted in Remote Sensing of Environment, in June 2022.*
- Vita Ayoub, Renaud Hostache, Patrick Matgen, Marco Chini, Ramona Maria-Pelich, and Carole Delenne. Estimating flood depth from space: an automatic method based on satellite flood imagery and topography data. *IAHS Montpellier, The XIth Scientific Assembly of the International Association of Hydrological Sciences, May to June 2022.*
- Vita Ayoub, Carole Delenne, David Mason, Marco Chini, Ramona-Maria Pelich, and Renaud Hostache. Rapid simulations of large scale flood inundations using porosity functions. *Simhydro 2021 - 6th International Conference Models for complex and global water issues - Practices and expectations*, 2021.
- Vita Ayoub, Carole Delenne, Patrick Matgen, Pascal Finaud-Guyot, and Renaud Hostache. A 2d shallow water model with depth-dependant porosity applied to the severn river. In *River Flow 2020-10th Conference on Fluvial Hydraulics*, 2020
- Vita Ayoub, Carole Delenne, Patrick Matgen, Pascal Finaud-Guyot, and Renaud Hostache. Towards fast large-scale flood simulations using 2D Shallow water modelling with depth-dependant porosity. In *EGU General Assembly*, 2020.
- Vita Ayoub, Renaud Hostache, Patrick Matgen, and Carole Delenne. Estimation de niveaux d'eau à partir d'images satellitaires radar et de données topographiques. In *Journées de Modélisation des Surfaces Continentales*, 2019.



# A porosity-based flood inundation modelling approach for enabling faster large scale simulations

Vita Ayoub<sup>a,b,c,\*</sup>, Carole Delenne<sup>b,c</sup>, Marco Chini<sup>a</sup>, Pascal Finaud-Guyot<sup>b,c</sup>, David Mason<sup>d</sup>, Patrick Matgen<sup>a</sup>, Ramona Maria-Pelich<sup>a</sup>, Renaud Hostache<sup>a,e</sup>

<sup>a</sup> Luxembourg Institute of Science and Technology, Environmental Research and Innovation Department, Esch-sur-Alzette, Luxembourg

<sup>b</sup> HSM, Univ. Montpellier, CNRS, IRD, Montpellier, France

<sup>c</sup> Inria, Team Lemon, Montpellier, France

<sup>d</sup> University of Reading, Department of Geography and Environmental Science, Reading, United Kingdom

<sup>e</sup> UMR Espace-Dev, IRD, Univ. Réunion, Univ. Guyane, Univ. Antilles, Univ. Nouvelle Calédonie, UPVD, Univ. Montpellier, Montpellier, France

## ARTICLE INFO

### Keywords:

Shallow water model  
Porosity-based model  
Flood inundation  
Large scale  
High-resolution data  
Fast simulations

## ABSTRACT

Floods are among the most devastating natural hazards in the world. With climate change and growing urbanisation, floods are expected to become more frequent and severe in the future. Hydrodynamic models are powerful tools for flood hazard assessment but face numerous challenges, especially when operating at a large scale. The downside of discretising an area using a fine mesh yielding more accurate results, is the expensive computational cost of simulations. Moreover, critical input information such as bathymetry (i.e. riverbed geometry) are required but cannot be easily collected by field measurements or remote sensing observations. During the past few years, the development of sub grid models has gained a growing interest as these enable faster simulations by using coarser cells and, at the same time, preserve small-scale topography variations within the cell. In this study, we propose and evaluate a modelling framework based on the shallow water 2D model with depth-dependent porosity enabling to represent floodplain and riverbed topography through porosity functions. To enable a careful and meaningful evaluation of the model, we set up a 2D classical model and use it as a benchmark. We also exploit ground truth data and remote sensing derived flood inundation maps to evaluate the proposed modelling framework and use as test cases the 2007 and 2012 flood events of the river Severn. Our empirical results demonstrate a high performance and low computational cost of the proposed model for fast flood simulations at a large scale.

## 1. Introduction

With the increasing risk of more frequent and severe floods (Arnell and Gosling, 2016) due to climate change and growing urbanisation, there is a crucial need to make more investments in flood management. Impacts of floods include human, socio-economical and environmental losses. Poorly conducted hazard assessments can lead to inefficient risk management, from insufficient protective mitigation measures to expensive rebuilding of devastated areas (Baan and Klijn, 2004; Meyer et al., 2009). Instead, well-conducted flood risk assessments provide a valuable support for decision making related to urban planning and emergency response preparedness. Therefore, it is essential to improve flood management systems to better anticipate and further reduce potential flood risk (Pradhan et al., 2014; Tehrany et al., 2014). In this context, hydrological and hydraulic models play a central role in flood forecasting as they provide predictions of water streamflows and levels

across various temporal and spatial scales (Revilla-Romero et al., 2016; Hostache et al., 2018).

The most common flood inundation (hydraulic) models are based on the depth-averaged Navier Stokes equations, also called de Saint-Venant or Shallow Water Equations (SWE). The resolution of these equations can be carried out in one (1D) or two dimensions (2D). 1D models solve the 1D formulation of the SWE (Bates and De Roo, 2000) where the flow is assumed to be unidirectional and water levels are assumed to be constant across sections. Although they are relatively easy to setup and fast to run (Cunge, 1980), these models fail to provide accurate predictions of overbanking flow and in presence of complex topographies, especially because the momentum transfers between the channel and the floodplain are neglected. 1D-storage area models (also often referred to as 1D+ or quasi-2D) are sometimes preferred as they

\* Corresponding author at: Luxembourg Institute of Science and Technology, Environmental Research and Innovation Department, Esch-sur-Alzette, Luxembourg.

E-mail address: [vitaayoub@outlook.com](mailto:vitaayoub@outlook.com) (V. Ayoub).

<https://doi.org/10.1016/j.advwatres.2022.104141>

Received 20 July 2021; Received in revised form 19 January 2022; Accepted 24 January 2022

Available online 9 February 2022

0309-1708/© 2022 Luxembourg Institute of Science and Technology. Published by Elsevier Ltd. This is an open access article under the CC BY license (<http://creativecommons.org/licenses/by/4.0/>).

# Bibliography

- [1] Peyman Abbaszadeh, Hamid Moradkhani, and Hongxiang Yan. Enhancing hydrologic data assimilation by evolutionary particle filter and markov chain monte carlo. *Advances in Water Resources*, 111:192–204, 2018.
- [2] Shahab Afshari, Ahmad A Tavakoly, Mohammad Adnan Rajib, Xing Zheng, Michael L Follum, Ehsan Omranian, and Balázs M Fekete. Comparison of new generation low-complexity flood inundation mapping tools with a hydrodynamic model. *Journal of Hydrology*, 556:539–556, 2018.
- [3] Taslima Akter and Slobodan P Simonovic. Aggregation of fuzzy views of a large number of stakeholders for multi-objective flood management decision-making. *Journal of environmental management*, 77(2):133–143, 2005.
- [4] Douglas E Alsdorf, Ernesto Rodríguez, and Dennis P Lettenmaier. Measuring surface water from space. *Reviews of Geophysics*, 45(2), 2007.
- [5] KM Andreadis, CB Brinkerhoff, and CJ Gleason. Constraining the assimilation of swot observations with hydraulic geometry relations. *Water Resources Research*, 56(5):e2019WR026611, 2020.
- [6] Konstantinos M Andreadis, Elizabeth A Clark, Dennis P Lettenmaier, and Douglas E Alsdorf. Prospects for river discharge and depth estimation through assimilation of swath-altimetry into a raster-based hydrodynamics model. *Geophysical Research Letters*, 34(10), 2007.
- [7] Nigel W Arnell and Simon N Gosling. The impacts of climate change on river flood risk at the global scale. *Climatic Change*, 134(3):387–401, 2016.
- [8] Vita Ayoub, Carole Delenne, Marco Chini, Pascal Finaud-Guyot, David Mason, Patrick Matgen, Ramona Maria-Pelich, and Renaud Hostache. A porosity-based flood inundation modelling approach for enabling faster large scale simulations. *Advances in Water Resources*, 162:104141, 2022.
- [9] Vita Ayoub, Carole Delenne, Patrick Matgen, Pascal Finaud-Guyot, and Renaud Hostache. A 2d shallow water model with depth-dependant porosity applied to the severn river. In *River Flow 2020-10th Conference on Fluvial Hydraulics*, 2020.

- 
- [10] Paul JA Baan and Frans Klijn. Flood risk perception and implications for flood risk management in the netherlands. *International journal of river basin management*, 2(2):113–122, 2004.
- [11] Rui Bai, Tiejian Li, Yuefei Huang, Jiaye Li, and Guangqian Wang. An efficient and comprehensive method for drainage network extraction from dem with billions of pixels using a size-balanced binary search tree. *Geomorphology*, 238:56–67, 2015.
- [12] Paul D Bates and APJ De Roo. A simple raster-based model for flood inundation simulation. *Journal of hydrology*, 236(1-2):54–77, 2000.
- [13] Sylvain Biancamaria, Michael Durand, KM Andreadis, PD Bates, Aaron Boone, NM Mognard, Ernesto Rodriguez, DE Alsdorf, DP Lettenmaier, and EA Clark. Assimilation of virtual wide swath altimetry to improve arctic river modeling. *Remote Sensing of Environment*, 115(2):373–381, 2011.
- [14] Stéphane Calmant, Frédérique Seyler, and Jean François Cretaux. Monitoring continental surface waters by satellite altimetry. *Surveys in geophysics*, 29(4):247–269, 2008.
- [15] Wenxi Cao, André Twele, Simon Plank, and Sandro Martinis. A three-class change detection methodology for sar-data based on hypothesis testing and markov random field modelling. *International journal of remote sensing*, 39(2):488–504, 2018.
- [16] Alberto Carrassi, Marc Bocquet, Laurent Bertino, and Geir Evensen. Data assimilation in the geosciences: An overview of methods, issues, and perspectives. *Wiley Interdisciplinary Reviews: Climate Change*, 9(5):e535, 2018.
- [17] Vincenzo Casulli. A conservative semi-implicit method for coupled surface–subsurface flows in regional scale. *International Journal for Numerical Methods in Fluids*, 79(4):199–214, 2015.
- [18] Bo Chen, Witold F Krajewski, Radek Goska, and Nathan Young. Using lidar surveys to document floods: A case study of the 2008 iowa flood. *Journal of Hydrology*, 553:338–349, 2017.
- [19] Marco Chini, Renaud Hostache, Laura Giustarini, and Patrick Matgen. A hierarchical split-based approach for parametric thresholding of sar images: Flood inundation as a test case. *IEEE Transactions on Geoscience and Remote Sensing*, 55(12):6975–6988, 2017.
- [20] Marco Chini, Ramona Pelich, Luca Pulvirenti, Nazzareno Pierdicca, Renaud Hostache, and Patrick Matgen. Sentinel-1 insar coherence to detect floodwater in urban areas: Houston and hurricane harvey as a test case. *Remote Sensing*, 11(2):107, 2019.
- [21] Sagy Cohen, G Robert Brakenridge, Albert Kettner, Bradford Bates, Jonathan Nelson, Richard McDonald, Yu-Fen Huang, Dinuke Munasinghe, and Jiaqi Zhang. Estimating

- floodwater depths from flood inundation maps and topography. *JAWRA Journal of the American Water Resources Association*, 54(4):847–858, 2018.
- [22] Elizabeth S Cooper, Sarah L Dance, Javier Garcia-Pintado, Nancy K Nichols, and Polly J Smith. Observation impact, domain length and parameter estimation in data assimilation for flood forecasting. *Environmental Modelling & Software*, 104:199–214, 2018.
- [23] Elizabeth S Cooper, Sarah L Dance, Javier García-Pintado, Nancy K Nichols, and Polly J Smith. Observation operators for assimilation of satellite observations in fluvial inundation forecasting. *Hydrology and Earth System Sciences*, 23(6):2541–2559, 2019.
- [24] Dim Coumou and Stefan Rahmstorf. A decade of weather extremes. *Nature climate change*, 2(7):491–496, 2012.
- [25] Mathieu Coustau, Sophie Ricci, Valérie Borrell-Estupina, Christophe Bouvier, and Olivier Thual. Benefits and limitations of data assimilation for discharge forecasting using an event-based rainfall–runoff model. *Natural Hazards and Earth System Sciences*, 13(3):583–596, 2013.
- [26] Jean Cunge. Practical aspects of computational river hydraulics. *Pitman Publishing Ltd. London,(17 CUN), 1980, 420*, 1980.
- [27] A. Dasgupta, R. Hostache, R. Ramsankaran, Guy J.-P. Schumann, Stefania Grimaldi, Valentijn R. N. Pauwels, and Jeffrey P. Walker. On the impacts of observation location, timing, and frequency on flood extent assimilation performance. *Water Resour. Res.*, 57(2):e2020WR028238, 2021.
- [28] Antara Dasgupta, Renaud Hostache, RAAJ Ramsankaran, Guy J-P Schumann, Stefania Grimaldi, Valentijn RN Pauwels, and Jeffrey P Walker. A mutual information-based likelihood function for particle filter flood extent assimilation. *Water Resources Research*, 57(2):e2020WR027859, 2021.
- [29] A Defina, L D’alpaos, and B Matticchio. A new set of equations for very shallow water and partially dry areas suitable to 2d numerical models. In *Modelling of flood propagation over initially dry areas*, pages 72–81. ASCE, 1994.
- [30] Andrea Defina. Two-dimensional shallow flow equations for partially dry areas. *Water Resources Research*, 36(11):3251–3264, 2000.
- [31] Carole Delenne, Jean-Stéphane Bailly, Antoine Rousseau, Renaud Hostache, and Olivier Boutron. Endorheic waterbodies delineation from remote sensing as a tool for immersed surface topography. *IEEE Geoscience and Remote Sensing Letters*, 2021.
- [32] Giuliano Di Baldassarre, Guy Schumann, Luigia Brandimarte, and Paul Bates. Timely low resolution sar imagery to support floodplain modelling: a case study review. *Surveys in geophysics*, 32(3):255–269, 2011.

- 
- [33] C. Di Mauro, R. Hostache, P. Matgen, Ramona Pelich, Marco Chini, Peter Jan van Leeuwen, Nancy Nichols, and Gunter Blöschl. Assimilation of probabilistic flood maps from sar data into a coupled hydrologic-hydraulic forecasting model: a proof of concept. *Hydrol. Earth Syst. Sci.*, 25:4081–4097, 2021.
- [34] Concetta Di Mauro, Nancy K Nichols, Renaud Hostache, Patrick Matgen, Ramona-Maria Pelich, Marco Chini, Peter Jan van Leeuwen, and Guenter Bloeschl. A tempered particle filter to enhance the assimilation of sar derived flood extent maps into flood forecasting models. 2022.
- [35] Gift Dumedah and Paulin Coulibaly. Evaluating forecasting performance for data assimilation methods: The ensemble kalman filter, the particle filter, and the evolutionary-based assimilation. *Advances in water resources*, 60:47–63, 2013.
- [36] Michael Durand, CJ Gleason, Pierre-André Garambois, David Bjerklie, LC Smith, Hélène Roux, Elizandro Rodriguez, Paul D Bates, Tamlin M Pavelsky, Jerome Monnier, et al. An intercomparison of remote sensing river discharge estimation algorithms from measurements of river height, width, and slope. *Water Resources Research*, 52(6):4527–4549, 2016.
- [37] Michael Durand, Jeffrey Neal, Ernesto Rodríguez, Konstantinos M Andreadis, Laurence C Smith, and Yeosang Yoon. Estimating reach-averaged discharge for the river severn from measurements of river water surface elevation and slope. *Journal of Hydrology*, 511:92–104, 2014.
- [38] Pascal Finaud-Guyot, Carole Delenne, Vincent Guinot, and Cécile Llovel. 1d–2d coupling for river flow modeling. *Comptes Rendus Mécanique*, 339(4):226–234, 2011.
- [39] Frédéric Frappart, K Do Minh, Julien l’Hermitte, Anny Cazenave, Guillaume Ramillien, Thuy Le Toan, and Nelly Mognard-Campbell. Water volume change in the lower mekong from satellite altimetry and imagery data. *Geophysical Journal International*, 167(2):570–584, 2006.
- [40] Pierre-André Garambois, Stéphane Calmant, Hélène Roux, Adrien Paris, Jérôme Monnier, Pascal Finaud-Guyot, Amanda Samine Montazem, and Joecila Santos da Silva. Hydraulic visibility: Using satellite altimetry to parameterize a hydraulic model of an ungauged reach of a braided river. *Hydrological Processes*, 31(4):756–767, 2017.
- [41] Pierre-André Garambois and Jérôme Monnier. Inference of effective river properties from remotely sensed observations of water surface. *Advances in Water Resources*, 79:103–120, 2015.
- [42] Javier García-Pintado, David C Mason, Sarah L Dance, Hannah L Cloke, Jeff C Neal, Jim Freer, and Paul D Bates. Satellite-supported flood forecasting in river networks: A real case study. *Journal of Hydrology*, 523:706–724, 2015.

- [43] Laura Giustarini, Renaud Hostache, Dmitri Kavetski, Marco Chini, Giovanni Corato, Stefan Schlaffer, and Patrick Matgen. Probabilistic flood mapping using synthetic aperture radar data. *IEEE Transactions on Geoscience and Remote Sensing*, 54(12):6958–6969, 2016.
- [44] Laura Giustarini, Renaud Hostache, Patrick Matgen, Guy J-P Schumann, Paul D Bates, and David C Mason. A change detection approach to flood mapping in urban areas using terrasar-x. *IEEE transactions on Geoscience and Remote Sensing*, 51(4):2417–2430, 2012.
- [45] Laura Giustarini, Patrick Matgen, Renaud Hostache, Mara Montanari, D Plaza, VRN Pauwels, GJM De Lannoy, Robain De Keyser, L Pfister, L Hoffmann, et al. Assimilating sar-derived water level data into a hydraulic model: a case study. *Hydrology and Earth System Sciences*, 15(7):2349–2365, 2011.
- [46] Neil J Gordon, David J Salmond, and Adrian FM Smith. Novel approach to nonlinear/non-gaussian bayesian state estimation. In *IEE proceedings F (radar and signal processing)*, volume 140, pages 107–113. IET, 1993.
- [47] S. Grimaldi, J. Xu, Y. Li, V.RN Pauwels, and J.P Walker. Flood mapping under vegetation using single sar acquisitions. *Remote sensing of Environment*, 237:111582, 2020.
- [48] Stefania Grimaldi, Yuan Li, Valentijn Pauwels, and Jeffrey P Walker. Remote sensing-derived water extent and level to constrain hydraulic flood forecasting models: Opportunities and challenges. *Surveys in Geophysics*, 37(5):977–1034, 2016.
- [49] Vincent Guinot. Multiple porosity shallow water models for macroscopic modelling of urban floods. *Advances in Water Resources*, 37:40–72, 2012.
- [50] Vincent Guinot, C Delenne, Antoine Rousseau, and O Boutron. Flux closures and source term models for shallow water models with depth-dependent integral porosity. *Advances in Water Resources*, 122:1–26, 2018.
- [51] Vincent Guinot, Brett F Sanders, and Jochen E Schubert. Dual integral porosity shallow water model for urban flood modelling. *Advances in Water Resources*, 103:16–31, 2017.
- [52] Vincent Guinot and Sandra Soares-Frazão. Flux and source term discretization in two-dimensional shallow water models with porosity on unstructured grids. *International Journal for Numerical Methods in Fluids*, 50(3):309–345, 2006.
- [53] Vincent Häfliger, Eric Martin, Aaron Boone, Sophie Ricci, and Sylvain Biancamaria. Assimilation of synthetic swot river depths in a regional hydrometeorological model. *Water*, 11(1):78, 2019.
- [54] Edward Herbst and Frank Schorfheide. Tempered particle filtering. *Journal of Econometrics*, 210(1):26–44, 2019.

- 
- [55] R Heremans, A Willekens, D Borghys, B Verbeeck, J Valckenborgh, Mea Acheroy, and C Perneel. Automatic detection of flooded areas on envisat/asar images using an object-oriented classification technique and an active contour algorithm. In *International Conference on Recent Advances in Space Technologies, 2003. RAST'03. Proceedings of*, pages 311–316. IEEE, 2003.
- [56] Jean-Michel Hervouet, Rene Samie, and Benoît Moreau. Modelling urban areas in dam-break flood-wave numerical simulations. *DEVELOPMENTS IN WATER SCIENCE*, 47:1613–1620, 2002.
- [57] Matthew S Horritt and Paul D Bates. Effects of spatial resolution on a raster based model of flood flow. *Journal of Hydrology*, 253(1-4):239–249, 2001.
- [58] R Hostache, P Matgen, L Giustarini, Felix Norman Teferle, C Tailliez, J-F Iffly, and G Corato. A drifting gps buoy for retrieving effective riverbed bathymetry. *Journal of Hydrology*, 520:397–406, 2015.
- [59] Renaud Hostache, Marco Chini, Laura Giustarini, Jeffrey Neal, Dmitri Kavetski, Melissa Wood, Giovanni Corato, Ramona-Maria Pelich, and Patrick Matgen. Near-real-time assimilation of sar-derived flood maps for improving flood forecasts. *Water Resources Research*, 54(8):5516–5535, 2018.
- [60] Renaud Hostache, Xijun Lai, Jerome Monnier, and Christian Puech. Assimilation of spatially distributed water levels into a shallow-water flood model. part ii: Use of a remote sensing image of mosel river. *Journal of hydrology*, 390(3-4):257–268, 2010.
- [61] Renaud Hostache, Patrick Matgen, Guy Schumann, Christian Puech, Lucien Hoffmann, and Laurent Pfister. Water level estimation and reduction of hydraulic model calibration uncertainties using satellite sar images of floods. *IEEE Transactions on Geoscience and Remote Sensing*, 47(2):431–441, 2009.
- [62] Inria Lemon Team. SW2D Software: <http://sw2d.inria.fr/>.
- [63] Wendy Kenyon. Evaluating flood risk management options in scotland: A participant-led multi-criteria approach. *Ecological economics*, 64(1):70–81, 2007.
- [64] Byunghyun Kim, Brett F Sanders, James S Famiglietti, and Vincent Guinot. Urban flood modeling with porous shallow-water equations: A case study of model errors in the presence of anisotropic porosity. *Journal of Hydrology*, 523:680–692, 2015.
- [65] Donghwan Kim, Hanwen Yu, Hyongki Lee, Edward Beighley, Michael Durand, Douglas E Alsdorf, and Euiho Hwang. Ensemble learning regression for estimating river discharges using satellite altimetry data: Central congo river as a test-bed. *Remote sensing of environment*, 221:741–755, 2019.

- [66] Wolfgang Kron. Flood risk= hazard • values • vulnerability. *Water international*, 30(1):58–68, 2005.
- [67] X Lai, Q Liang, H Yesou, and S Daillet. Variational assimilation of remotely sensed flood extents using a 2-d flood model. *Hydrology and Earth System Sciences*, 18(11):4325–4339, 2014.
- [68] K Larnier, J Monnier, P-A Garambois, and J Verley. River discharge and bathymetry estimation from swot altimetry measurements. *Inverse Problems in Science and Engineering*, 29(6):759–789, 2021.
- [69] François-Xavier Le Dimet and Olivier Talagrand. Variational algorithms for analysis and assimilation of meteorological observations: theoretical aspects. *Tellus A: Dynamic Meteorology and Oceanography*, 38(2):97–110, 1986.
- [70] J Lhomme. One-dimensional, two-dimensional and macroscopic approaches to urban flood modelling. *PhD diss., Montpellier*, 2, 2006.
- [71] Kuan Li, Andrew Jackson, and Philip W Livermore. Variational data assimilation for the initial-value dynamo problem. *Physical Review E*, 84(5):056321, 2011.
- [72] Thibault Malou, P-A Garambois, Adrien Paris, Jerome Monnier, and Kevin Larnier. Generation and analysis of stage-fall-discharge laws from coupled hydrological-hydraulic river network model integrating sparse multi-satellite data. *Journal of Hydrology*, 603:126993, 2021.
- [73] Sandro Martinis and Christoph Rieke. Backscatter analysis using multi-temporal and multi-frequency sar data in the context of flood mapping at river saale, germany. *Remote Sensing*, 7(6):7732–7752, 2015.
- [74] Sandro Martinis, André Twele, and Stefan Voigt. Unsupervised extraction of flood-induced backscatter changes in sar data using markov image modeling on irregular graphs. *IEEE Transactions on Geoscience and Remote Sensing*, 49(1):251–263, 2010.
- [75] David C Mason, David M Cobby, Matthew S Horritt, and Paul D Bates. Floodplain friction parameterization in two-dimensional river flood models using vegetation heights derived from airborne scanning laser altimetry. *Hydrological processes*, 17(9):1711–1732, 2003.
- [76] David C Mason, Matthew S Horritt, Neil M Hunter, and Paul D Bates. Use of fused airborne scanning laser altimetry and digital map data for urban flood modelling. *Hydrological Processes: An International Journal*, 21(11):1436–1447, 2007.
- [77] David C Mason, Mark Trigg, Javier Garcia-Pintado, Hannah L Cloke, Jeffrey C Neal, and Paul D Bates. Improving the tandem-x digital elevation model for flood modelling using

- flood extents from synthetic aperture radar images. *Remote Sensing of Environment*, 173:15–28, 2016.
- [78] DC Mason, GJ-P Schumann, JC Neal, J Garcia-Pintado, and PD Bates. Automatic near real-time selection of flood water levels from high resolution synthetic aperture radar images for assimilation into hydraulic models: A case study. *Remote Sensing of Environment*, 124:705–716, 2012.
- [79] Patrick Matgen, Mara Montanari, Renaud Hostache, Laurent Pfister, L Hoffmann, D Plaza, VRN Pauwels, GJM De Lannoy, Robain De Keyser, and HHG Savenije. Towards the sequential assimilation of sar-derived water stages into hydraulic models using the particle filter: proof of concept. *Hydrology and Earth System Sciences*, 14(9):1773–1785, 2010.
- [80] Patrick Matgen, G Schumann, J-B Henry, Lucien Hoffmann, and Laurent Pfister. Integration of sar-derived river inundation areas, high-precision topographic data and a river flow model toward near real-time flood management. *International Journal of Applied Earth Observation and Geoinformation*, 9(3):247–263, 2007.
- [81] Di Mauro, Renaud Hostache, Patrick Matgen, Ramona Pelich, Marco Chini, Peter Jan Van Leeuwen, Nancy K Nichols, Günter Blöschl, et al. Assimilation of probabilistic flood maps from sar data into a coupled hydrologic–hydraulic forecasting model: a proof of concept. *Hydrology and Earth System Sciences*, 25(7):4081–4097, 2021.
- [82] Volker Meyer, Sebastian Scheuer, and Dagmar Haase. A multicriteria approach for flood risk mapping exemplified at the mulde river, germany. *Natural hazards*, 48(1):17–39, 2009.
- [83] P Christopher D Milly, Richard T Wetherald, KA Dunne, and Thomas L Delworth. Increasing risk of great floods in a changing climate. *Nature*, 415(6871):514–517, 2002.
- [84] Chrissy Mitchell. Flood resilience—a time for cathedral-based thinking and action!, 2022.
- [85] Jerome Monnier, Frédéric Couderc, Denis Dartus, Kévin Larnier, Ronan Madec, and J-P Vila. Inverse algorithms for 2d shallow water equations in presence of wet dry fronts: Application to flood plain dynamics. *Advances in Water Resources*, 97:11–24, 2016.
- [86] Alberto Montanari. What do we mean by ‘uncertainty’? the need for a consistent wording about uncertainty assessment in hydrology. *Hydrological Processes: An International Journal*, 21(6):841–845, 2007.
- [87] Norman Mueller, Adam Lewis, Dale Roberts, Steven Ring, R Melrose, J Sixsmith, Leo Lymburner, A McIntyre, P Tan, S Curnow, et al. Water observations from space: Mapping surface water from 25 years of landsat imagery across australia. *Remote Sensing of Environment*, 174:341–352, 2016.

- [88] Jeffrey Neal, GJP Schumann, and Paul D Bates. A simple model for simulating river hydraulics and floodplain inundation over large and data sparse areas. *Water Resour Res*, 48, 2012.
- [89] Jeffrey Neal, Guy Schumann, and Paul Bates. A subgrid channel model for simulating river hydraulics and floodplain inundation over large and data sparse areas. *Water Resources Research*, 48(11), 2012.
- [90] Thanh Huy Nguyen, Sophie Ricci, Christophe Fatras, Andrea Piacentini, Anth ea Delmotte, Emeric Lavergne, and Peter Kettig. Improvement of flood extent representation with remote sensing data and data assimilation. *IEEE Transactions on Geoscience and Remote Sensing*, 60:1–22, 2022.
- [91] Antonio Donato Nobre, Luz Adriana Cuartas, M Hodnett, Camilo Daleles Renno, G Rodrigues, A Silveira, and S Saleska. Height above the nearest drainage—a hydrologically relevant new terrain model. *Journal of Hydrology*, 404(1-2):13–29, 2011.
- [92] Ian Olthof and Simon Tolszczuk-Leclerc. Comparing landsat and radarsat for current and historical dynamic flood mapping. *Remote Sensing*, 10(5):780, 2018.
- [93] Hind Oubanas, Igor Gejadze, P-O Malaterre, M Durand, Rui Wei, Renato PM Frason, and Alessio Domeneghetti. Discharge estimation in ungauged basins through variational data assimilation: The potential of the swot mission. *Water Resources Research*, 54(3):2405–2423, 2018.
- [94] Binh Pham-Duc, Catherine Prigent, and Filipe Aires. Surface water monitoring within cambodia and the vietnamese mekong delta over a year, with sentinel-1 sar observations. *Water*, 9(6):366, 2017.
- [95] Biswajeet Pradhan, Ulrike Hagemann, Mahyat Shafapour Tehrany, and Nikolas Prechtel. An easy to use arcmap based texture analysis program for extraction of flooded areas from terrasar-x satellite image. *Computers & geosciences*, 63:34–43, 2014.
- [96] L eo Pujol, Pierre-Andr e Garambois, Pascal Finaud-Guyot, Jerome Monnier, K evin Larnier, Robert Mose, Sylvain Biancamaria, Herv e Yesou, D Moreira, Adrien Paris, et al. Estimation of multiple inflows and effective channel by assimilation of multi-satellite hydraulic signatures: The ungauged anabranching negro river. *Journal of Hydrology*, 591:125331, 2020.
- [97] L Pulvirenti, N Pierdicca, M Chini, and L Guerriero. An algorithm for operational flood mapping from synthetic aperture radar (sar) data using fuzzy logic. *Natural Hazards and Earth System Sciences*, 11(2):529–540, 2011.
- [98] Damien Raclot. Remote sensing of water levels on floodplains: a spatial approach guided by hydraulic functioning. *International Journal of Remote Sensing*, 27(12):2553–2574, 2006.

- [99] Rolf H Reichle. Data assimilation methods in the earth sciences. *Advances in water resources*, 31(11):1411–1418, 2008.
- [100] Camilo Daleles Rennó, Antonio Donato Nobre, Luz Adriana Cuartas, João Vianei Soares, Martin G Hodnett, and Javier Tomasella. Hand, a new terrain descriptor using srtm-dem: Mapping terra-firme rainforest environments in amazonia. *Remote Sensing of Environment*, 112(9):3469–3481, 2008.
- [101] Beatriz Revilla-Romero, Niko Wanders, Peter Burek, Peter Salamon, and Ad de Roo. Integrating remotely sensed surface water extent into continental scale hydrology. *Journal of hydrology*, 543:659–670, 2016.
- [102] Sophie Ricci, Andrea Piacentini, Olivier Thual, Etienne Le Pape, and Gabriel Jonville. Correction of upstream flow and hydraulic state with data assimilation in the context of flood forecasting. *Hydrology and Earth System Sciences*, 15(11):3555–3575, 2011.
- [103] Brett F Sanders. Evaluation of on-line dems for flood inundation modeling. *Advances in water resources*, 30(8):1831–1843, 2007.
- [104] Brett F Sanders, Jochen E Schubert, and Humberto A Gallegos. Integral formulation of shallow-water equations with anisotropic porosity for urban flood modeling. *Journal of Hydrology*, 362(1-2):19–38, 2008.
- [105] Joseph T Schaefer. The critical success index as an indicator of warning skill. *Weather and forecasting*, 5(4):570–575, 1990.
- [106] Jochen Schanze. Flood risk management—a basic framework. In *Flood risk management: hazards, vulnerability and mitigation measures*, pages 1–20. Springer, 2006.
- [107] Stefan Schlaffer, Marco Chini, Denise Dettmering, and Wolfgang Wagner. Mapping wetlands in zambia using seasonal backscatter signatures derived from envisat asar time series. *Remote Sensing*, 8(5):402, 2016.
- [108] G Schumann, P Matgen, L Hoffmann, R Hostache, F Pappenberger, and L Pfister. Deriving distributed roughness values from satellite radar data for flood inundation modelling. *Journal of Hydrology*, 344(1-2):96–111, 2007.
- [109] Laurence C Smith. Satellite remote sensing of river inundation area, stage, and discharge: A review. *Hydrological processes*, 11(10):1427–1439, 1997.
- [110] Sandra Soares-Frazão, Julien Lhomme, Vincent Guinot, and Yves Zech. Two-dimensional shallow-water model with porosity for urban flood modelling. *Journal of Hydraulic Research*, 46(1):45–64, 2008.
- [111] Tajdarul H Syed, James S Famiglietti, and Don P Chambers. Grace-based estimates of terrestrial freshwater discharge from basin to continental scales. *Journal of Hydrometeorology*, 10(1):22–40, 2009.

- [112] Hossein Tabari. Climate change impact on flood and extreme precipitation increases with water availability. *Scientific reports*, 10(1):1–10, 2020.
- [113] Kenji Tanaka, Yoichi Fujihara, Keisuke Hoshikawa, and Hideto Fujii. Development of a flood water level estimation method using satellite images and a digital elevation model for the mekong floodplain. *Hydrological sciences journal*, 64(2):241–253, 2019.
- [114] Mahyat Shafapour Tehrany, Biswajeet Pradhan, and Mustafa Neamah Jebur. Flood susceptibility mapping using a novel ensemble weights-of-evidence and support vector machine models in gis. *Journal of hydrology*, 512:332–343, 2014.
- [115] B Tellman, JA Sullivan, C Kuhn, AJ Kettner, CS Doyle, GR Brakenridge, TA Erickson, and DA Slayback. Satellite imaging reveals increased proportion of population exposed to floods. *Nature*, 596(7870):80–86, 2021.
- [116] Jacqueline Torti. Floods in southeast asia: A health priority. *Journal of global health*, 2(2), 2012.
- [117] André Twele, Wenxi Cao, Simon Plank, and Sandro Martinis. Sentinel-1-based flood mapping: a fully automated processing chain. *International Journal of Remote Sensing*, 37(13):2990–3004, 2016.
- [118] USACE. United States Army Corps of Engineers: Theoretical basis for one-dimensional flow calculations. In *Hydraulic reference manual*, chapter 2. USACE, Davis (CA, USA), 2002. Version 3.1.
- [119] Peter Jan Van Leeuwen. Nonlinear data assimilation in geosciences: an extremely efficient particle filter. *Quarterly Journal of the Royal Meteorological Society*, 136(653):1991–1999, 2010.
- [120] Peter Jan Van Leeuwen. Particle filters for nonlinear data assimilation in high-dimensional systems. In *Annales de la Faculté des sciences de Toulouse: Mathématiques*, volume 26, pages 1051–1085, 2017.
- [121] Peter Jan Van Leeuwen. Non-local observations and information transfer in data assimilation. *Frontiers in Applied Mathematics and Statistics*, 5:48, 2019.
- [122] Sanita Vetra-Carvalho, Sarah L Dance, David C Mason, Joanne A Waller, Elizabeth S Cooper, Polly J Smith, and Jemima M Tabcart. Collection and extraction of water level information from a digital river camera image dataset. *Data in Brief*, 33:106338, 2020.
- [123] L Wan, M Liu, F Wang, T Zhang, and HJ You. Automatic extraction of flood inundation areas from sar images: a case study of jilin, china during the 2017 flood disaster. *International Journal of Remote Sensing*, 40(13):5050–5077, 2019.

- [124] Albrecht H Weerts, Ghada Y El Serafy, Stef Hummel, Juzer Dhondia, and Herman Gerritsen. Application of generic data assimilation tools (datools) for flood forecasting purposes. *Computers & Geosciences*, 36(4):453–463, 2010.
- [125] Patrick Willems, Guido Vaes, D Popa, L Timbe, and Jean Berlamont. Quasi 2d river flood modelling. In *River Flow*, volume 2, pages 1253–1259. Swets & Zeitlinger Lisse, 2002.
- [126] Melissa Wood, Renaud Hostache, Jeffrey Neal, Thorsten Wagener, Laura Giustarini, Marco Chini, Giovanni Corato, Patrick Matgen, and Paul Bates. Calibration of channel depth and friction parameters in the lisflood-fp hydraulic model using medium-resolution sar data and identifiability techniques. *Hydrology and Earth System Sciences*, 20(12):4983–4997, 2016.
- [127] Xianhong Xie and Dongxiao Zhang. Data assimilation for distributed hydrological catchment modeling via ensemble kalman filter. *Advances in Water Resources*, 33(6):678–690, 2010.
- [128] Kun Yan, Giuliano Di Baldassarre, Dimitri P Solomatine, and Guy J-P Schumann. A review of low-cost space-borne data for flood modelling: topography, flood extent and water level. *Hydrological processes*, 29(15):3368–3387, 2015.
- [129] Yeosang Yoon, Michael Durand, Carolyn J Merry, Elizabeth A Clark, Konstantinos M Andreadis, and Douglas E Alsdorf. Estimating river bathymetry from data assimilation of synthetic swot measurements. *Journal of Hydrology*, 464:363–375, 2012.
- [130] Keqi Zhang, Daniel Gann, Michael Ross, Quin Robertson, Juan Sarmiento, Sheyla Santana, Jamie Rhome, and Cody Fritz. Accuracy assessment of aster, srtm, alos, and tdx dems for hispaniola and implications for mapping vulnerability to coastal flooding. *Remote Sensing of Environment*, 225:290–306, 2019.
- [131] Wenting Zhang, Xingnan Zhang, Yongzhi Liu, Wenwen Tang, Jan Xu, and Zhimin Fu. Assessment of flood inundation by coupled 1d/2d hydrodynamic modeling: A case study in mountainous watersheds along the coast of southeast china. *Water*, 12(3):822, 2020.
- [132] Jie Zhao, Ramona Pelich, Renaud Hostache, Patrick Matgen, Senmao Cao, Wolfgang Wagner, and Marco Chini. Deriving exclusion maps from c-band sar time-series in support of floodwater mapping. *Remote Sensing of Environment*, 265:112668, 2021.
- [133] Zhu Zhongming, Lu Linong, Yao Xiaona, Zhang Wangqiang, Liu Wei, et al. Release: New data shows millions of people, trillions in property at risk from flooding—but infrastructure investments now can significantly lower flood risk. 2020.
- [134] R Zielinski and Jerzy Chmiel. Vertical accuracy assessment of srtm c-band dem data for different terrain characteristics. *New developments and challenges in remote sensing (ed. BOCHENEK Z.)(Millpress, Rotterdam 2007)*, pages 685–693, 2007.

- [135] Hendrik Zwenzner and Stefan Voigt. Improved estimation of flood parameters by combining space based sar data with very high resolution digital elevation data. *Hydrology and Earth System Sciences*, 13(5):567–576, 2009.